E98/398

DIFFRACTIVE PRODUCTION OF RHO MESONS BY 147 GeV MUONS INCIDENT ON A DEUTERIUM TARGET

by

Leon Cimonos Myrianthopoulos

December, 1978

AAB1880

THE UNIVERSITY OF CHICAGO

DIFFRACTIVE PRODUCTION OF RHO MESONS BY 147 GeV MUONS INCIDENT ON A DEUTERIUM TARGET

A DISSERTATION SUBMITTED TO
THE FACULTY OF THE DIVISION OF THE PHYSICAL SCIENCES
IN CANDIDACY FOR THE DEGREE OF
DOCTOR OF PHILOSOPHY

DEPARTMENT OF PHYSICS

BY

LEON CIMONOS MYRIANTHOPOULOS

CHICAGO, ILLINOIS

DECEMBER, 1978

FERMILAB
LIBRARY

ACKNOWLEDGEMENTS

First and foremost I thank Professor H. L. Anderson, my thesis advisor, for his guidance and support in carrying out this research. He worked long and hard helping me bring it to its conclusion. I am also grateful to him for the opportunity to participate at the forefront of the experimental investigations during this exciting time for high energy physics, and for allowing me to benefit from his experience while, at the same time, fostering my independence.

I thank the numerous technical support personnel at the four collaborating institutions and at Fermilab, as well as all fellow experimenters for their contributions. In particular, it is a pleasure to acknowledge the many fruitful discussions and informative consultations with W. R. Francis, who pioneered the analysis of rho production from our hydrogen data. The programs, experience, and insight that he provided eased this work considerably. I also thank H. Matis for many useful suggestions and for his improvements to the plotting package routines. I appreciate, now more than then, the encouragement by S.C. Wright to present some of my results at an early stage of the analysis. I am indebted to T. Quirk, S. Pordes, and W. A. Loomis for providing the tertiary tapes, to A. Skuja

LIBRARY

for developing many of the Monte Carlo routines, to B. Gordon for details of inclusive ρ production, to L. Verhey for sharing his expertise on the muon beam line, and to R. Wilson for his active interest in my topic.

At Chicago, the important contributions of the staff of the Electronics Shop, headed by T. Nunamaker, and of the Engineering Services Group, headed by R. Armstrong, were vital to the correct and timely functioning of this experiment and were very much appreciated. I am particularly thankful to two members of the latter group, Richard Northrop and Glenn Okazaki, for their skillful drawing of most of the figures in this thesis. Special thanks go to Rudy Gabriel for his multiple contributions to the design, construction, and operation of the beam MWPC.

The careful and competent, in spite of the time limitations, typing of Rosemary Garrison is sincerely appreciated.

The Chicago contributions to this experiment and all the work involved in bringing this thesis to this stage were supported by grants from the National Science Foundation. I am deeply grateful for a University of Chicago research assistantship, funded by these grants, during my apprenticeship in high energy physics.

Last, but by no means least, I thank my parents and my wife for their part in this accomplishment. Their contributions are too numerous to mention here.

TABLE OF CONTENTS

	Page
ACKNOWLEDGEMENTS	ii
LIST OF TABLES	vi
LIST OF ILLUSTRATIONS.	viii
ABSTRACT	xi
Chapter	
I. THEORETICAL AND EXPERIMENTAL BACKGROUND . . .	1
General Introduction Notation and Definitions of Variables Theoretical Considerations Experimental Background Target Choice	
II. THE EXPERIMENT.	16
Muon Beam The Apparatus Electronic and Physical Trigger Components Data Acquisition	
III. DATA REDUCTION	33
Secondary Data Tapes Event Reconstruction Tertiary Tapes	
IV. EVENT SELECTION	55
Halo Rejection Selection Criteria	

TABLE OF CONTENTS--Continued

Chapter		Page
V.	DATA ANALYSIS	78
	Raw Cross Sections Evaluation Effective Luminosity Monte Carlo Acceptance Calculation Distributions Studied	
VI.	RESULTS	101
	Mass Cross Sections t Cross Sections Conclusions	
REFERENCES.		111

LIST OF TABLES

Table		Page
1.	Experiments on rho production by virtual photons	115
2.	Hadron assignment to halo by test	116
3.	Bin kinematics	117
4.	Event distribution into the m bins	118
5.	Distribution of the events with $0.6 < m < 1.0$ GeV into the t bins	119
6.	Acceptance-related quantities depending only on Q^2	120
7.	Values of the acceptance-related quantity S and of its estimated error for the m bins	121
8.	Values of the acceptance-related quantity S and of its estimated error for the t bins	122
9.	Raw m differential cross sections, per nucleon, in μbarns/GeV	123
10.	Raw t differential cross sections, per deuteron, in μbarns /GeV^2	124
11.	Integrals of the smeared functions parameterizing the mass differential cross sections	125
12.	Integrals of the unsmeared functions parameterizing the mass differential cross sections	126
13.	Coefficients determining the t resolution correction factor	127
14.	Results of the fits to the mass differential cross sections	128

LIST OF TABLES--Continued

Table		Page
15.	Mass resolution correction factors	129
16.	Q^2 variation of the total cross section. . . .	130
17.	Results of the fits to the t differential cross sections	131

LIST OF ILLUSTRATIONS

Figure		Page
1.	Feynman diagram for diffractive rho muo-production via single photon exchange. . . .	132
2.	Variation of the virtual photon flux factor with Q^2, for three values of ν. . . .	133
3.	Feynman diagram for rho production by timelike virtual photons from $e^+ - e^-$ annihilation	134
4.	Slope of the diffractive peak as a function of the $\gamma \rightarrow \rho$ transition time. . . .	135
5.	Schematic and optics of the muon beam line . .	136
6.	Diagram of the apparatus..	137
7.	Variation of several counting rates as a function of the position of the N-veto counter across the beam.	138
8.	Geometry of a bending plane trajectory for a sharp-edged model of the CCM field	139
9.	Downstream trackfinding efficiency variation along the horizontal direction.	140
10.	Tertiary tape information about an event . . .	142
11.	Projection to the vertex of downstream Y-Z "hadron" tracks.	143
12.	Projection to the vertex of upstream X-Z "hadron" tracks.	144
13.	Pion pair opening angle vs. pion energy for 100 GeV ρ decay.	145
14.	Pion pair mass vs. opening angle	146
15.	Z position of the interaction vertex	147

LIST OF ILLUSTRATIONS--Continued

Figure		Page
16.	Energy balance distribution	148
17.	Event t distribution	149
18.	Scattered muon acceptance variation with Q^2 and ν	151
19.	Q^2 - ν distribution of the events passing all cuts	153
20.	Dipion invariant mass histograms for the four Q^2 ranges	154
21.	Definition of the angles of the rho-decay angular distribution	155
22.	Raw mass differential cross sections, per nucleon, for the four Q^2 ranges.	157
23.	Mass resolution.	159
24.	Simulation of ρ production by the diffractive scattering of nonresonant pions.	160
25.	Resonant, nonresonant background, and interference components of the mass spectra . . .	162
26.	Mass differential cross sections and fit for $0.0 < Q^2 < 0.1$ GeV^2/c^2	164
27.	Mass differential cross sections and fit for $0.1 < Q^2 < 0.3$ GeV^2/c^2	166
28.	Mass differential cross sections and fit for $0.3 < Q^2 < 1.0$ GeV^2/c^2	168
29.	Mass differential cross sections and fit for $1.0 < Q^2 < 5.0$ GeV^2/c^2	170
30.	Q^2 variation of the total ρ production cross section.	171

LIST OF ILLUSTRATIONS--Continued

Figure		Page
31.	Comparison of $\sigma_\rho(Q^2)$ measured by experiments performed at different energies	172
32.	Energy variation of $\sigma(\gamma p \rightarrow \rho p)$.	173
33.	t differential cross sections and fit for $0.0 < Q^2 < 0.1$ GeV^2/c^2	175
34.	t differential cross sections and fit for $0.1 < Q^2 < 0.3$ GeV^2/c^2	177
35.	t differential cross sections and fit for $0.3 < Q^2 < 1.0$ GeV^2/c^2	179
36.	t differential cross sections and fit for $1.0 < Q^2 < 5.0$ GeV^2/c^2	181
37.	Contours of equal probability for the $0.3 < Q^2 < 1.0$ fit to the t differential cross sections	183
38.	Q^2 variation of B, the $\frac{d\sigma}{dt}$ slope.	185

ABSTRACT

The diffractive production of ρ mesons has been observed in the scattering of 147 GeV muons by deuterium. The pion pair from ρ decay and the scattered (triggering) muon were observed and momentum analyzed by a wide aperture spectrometer featuring a 74 KGm magnet. Out of over 100,000 analyzed triggers 459 events ascribed to this exclusive channel were used for the extraction of differential cross sections for the process in four different bins in Q^2, the square of the four-momentum transfer to the virtual photon which mediates the muon interaction. The Q^2 variation of the cross section is best described by the square of the rho propagator but is also consistent with Vector Dominance predictions. By extrapolating to $Q^2 = 0$ we predict that $\sigma(\gamma p \rightarrow \rho p) = 8.7 \pm 0.4$ μbarns (not including a 7 percent systematic error) for $E_\gamma = 112$ GeV. Coherent rho production by virtual photons is seen for the first time, manifested as an enhancement in the very forward ($|t| < 0.1$ GeV^2, where t is the square of the four-momentum transfer from the virtual photon to the rho) cross section. It is, most likely, characterized by the same Q^2 variation. The t-distributions can be described by a diffraction peak slope parameter which is independent of Q^2. This is evidence against the concept of photon shrinkage.

DEDICATION

I dedicate this work to my wife, Maro, grateful for her infinite patience and understanding.

CHAPTER I

THEORETICAL AND EXPERIMENTAL BACKGROUND

General Introduction

It is a remarkable feature of the particles of nature that none are truly elementary. Each comes with an admixture of every other particle with which it can interact. For example the electron, which by virtue of its electric charge can interact with the electromagnetic field, has associated with it a cloud of photons, the quanta of that field. Similarly, photons may transform into any of the several vector mesons, strongly interacting particles with the same quantum numbers. Such vector mesons have a virtual existence. Once formed they quickly revert into photons again so that energy conservation is kept within the bounds admissible by the uncertainty principle. However, at sufficiently high energies and in the presence of a nucleus that takes up the momentum recoil, these vector mesons may materialize[1] and be observed.

This dissertation is a study of such a process. In particular, we have observed the diffractive production of ρ^0 mesons in the scattering of 147 GeV muons by deuterium. Out of all the events recorded when an incident muon lost energy by scattering off deuterium, we selected those which

gave a π^+-π^- pair with invariant mass close to that of the ρ meson. We limited our study to rhos that were elastically produced. That is events in which all the energy lost by the muon appeared in the two pions of ρ decay, due allowance for recoil being made.

In this dissertation we describe how the ρ mesons were identified. We show how their production depends on the momentum transferred to the virtual photon, through which the scattering takes place, and on the momentum transferred to them from this photon. Finally, it is shown how the muoproduced rhos are related to those observed in photoproduction.

Notation and Definitions of Variables

The scattering of muons from nucleons proceeds primarily thru the electromagnetic force. It is an important feature of our experiment that the interaction is dominated by single photon exchange and that the simple Feynman diagram of Figure 1 provides an adequate description of diffractive rho production. An incoming muon of four-momentum k emits a virtual photon γ^* and emerges with outgoing four-momentum k'. The four-momentum of the virtual photon is $q = k - k'$. The photon materializes into a ρ^o meson with the nucleons taking up the recoil four-momentum whose square is given by

$$t = (q - p_\rho)^2 = (p - p')^2$$

where p_ρ is the four-momentum of the ρ^o and where p and p' are the four-momenta of the nucleon system before and after the scattering, respectively.

The invariant q^2 is given in terms of measurable quantities by

$$q^2 \equiv -Q^2 = 2m_\mu^2 - 2EE' + 2\ |\vec{k}|\ |\vec{k}|\cos\theta < 0$$

where E and $\vec{k}$ (E' and $\vec{k}'$) denote the laboratory energy and momentum of the incident (scattered) muon and θ is the angle between $\vec{k}$ and $\vec{k}'$. Only scatterings with

$$Q^2 > Q^2_{min} = -2m_\mu^2 + 2\ (EE' - |\vec{k}|\ |\vec{k}'|)$$

are allowed by kinematics. It is a good approximation to take

$$Q^2_{min} = m_\mu^2\ \nu^2/(EE')$$

where $\nu = E - E'$ denotes the energy loss of the scattered muon (or the laboratory energy of the virtual photon).

The recoil N of Figure 1 could be the deuteron in its ground state or in the continuum. In a truly diffractive reaction N just absorbs momentum and allows the virtual photon to transform into a rho meson. In terms of observable quantities the square of the four-momentum transfer to N is given by

$$t = m_\rho^2 - Q^2 + 2\ |\vec{P}_\gamma|\ |\vec{P}_\rho|\cos\theta_{\gamma\rho} - 2\nu E_\rho$$

$$\simeq -\ \nu^2\ \theta^2_{\gamma\rho}$$

where $\theta_{\gamma\rho}$ is the laboratory angle between the directions of incidence of the virtual photon and of emergence of the rho, and

$$|\vec{P}_\gamma|^2 = \nu^2 + Q^2$$

The approximation neglects a correction term equal to $Q^2/(2M_N\ \nu)$, which never exceeds a few percent in the kinematic region under investigation. In the case of deuterium this expression for t has the additional advantage of making no assumption about the nature of the recoil, which was not observed in this experiment.

The cross section for the leptoproduction of a final state is related to that for the virtual photoproduction of the same state. In the Hand notation[2] the relation for the reaction of interest is

$$\frac{d^2\sigma}{dq^2 d\nu}(\mu + N \rightarrow \mu + \rho^o + N) = \Gamma_T(q^2, \nu)\ \sigma(\gamma^* + N \rightarrow \rho^o + N) \tag{I.1}$$

where Γ_T represents the flux of transverse virtual photons in a small $\{q^2, \nu\}$ area and is given by

$$\Gamma_T = \frac{\pi}{EE'}\ \frac{\alpha}{4\pi^2}\ \frac{E'}{E}\ \frac{2M\nu - Q^2}{2\ M\ Q^2}\ \frac{2}{1-\epsilon} \tag{I.2}$$

with ϵ being the virtual photon polarization parameter, determined by kinematics as

$$\varepsilon = \left[1 + 2 \frac{Q^2 + \nu^2}{Q^2 \left(1 - \frac{Q^2_{min}}{Q^2} \right)^2} \tan^2 \left(\frac{\theta}{2}\right) \right]^{-1}$$

and M being the mass of the proton.

Figure 2 shows the variation of Γ_T with Q^2 for three values of ν within the range of our acceptance, assuming an incident muon beam of 147.6 GeV. Since the virtual photon flux factor decreases as $1/Q^2$ most of the events are expected and found to populate the low Q^2 region. In the Q^2 region of practical interest for this study the virtual photon flux is approximately 500 times smaller than the incident muon flux.

The cross section for the production of any final state f by virtual photons incident on nucleons ($\gamma^* + N \rightarrow f$) depends on the values of Q^2 and ν characterizing the virtual photon and is defined as

$$\sigma(Q^2, \nu, f) \equiv \sigma_T (Q^2, \nu, f) + \varepsilon \sigma_L (Q^2, \nu, f)$$

Here σ_T and σ_L denote the cross sections for the production of the same final state f by transverse and longitudinal virtual photons, respectively. In the limit $Q^2 \rightarrow 0$, σ_T approaches the real photoproduction cross section while $\sigma_L \rightarrow 0$. This shows that the variation of the cross section with Q^2 will be different for each polarization and makes necessary the decomposition shown above. The polarization

parameter ϵ enters because at each (Q^2, ν) point the flux of longitudinally polarized photons is given by

$$\Gamma_L(Q^2, \nu) = \epsilon\ (Q^2, \nu, E)\ \Gamma_T(Q^2, \nu)$$

The cross section appearing in (I.1) (corresponding to $f = \rho^o + N$) stands for this combination of σ_L and σ_T and so do the results reported in later chapters. The ratio of the longitudinal to the transverse ρ production cross section is denoted by

$$R_\rho = \frac{\sigma_L\ (Q^2, \nu, \rho^o + N)}{\sigma_T\ (Q^2, \nu, \rho^o + N)}$$

following the symbolism for the inclusive case.

Theoretical Considerations

The transformation of a virtual photon into vector mesons also occurs in $e^+ - e^-$ annihilation. The Feynman diagram for rho production in this case is shown in Figure 3. The virtual photon is timelike with $q^2 = s$ the total c.m. energy of the colliding leptons. The production of a vector meson V of mass m_V occurs at positive values of q^2 $(= m_V^2)$. The transformation into a rho is governed by a coupling constant which has been evaluated by observing $e^+ + e^- \to \rho \to \pi^+ + \pi^-$ with the result[3]

$$\gamma_\rho^2/4\pi = 0.64 \pm 0.06.$$

The matrix element of the process is given by[4]

$$< \pi^+\pi^- | J_\mu | 0 > = < \pi^+\pi^- | \rho > \frac{1}{q^2 - m_\rho^2 + i\Gamma_\rho m_\rho} < \rho | J_\mu | 0 >$$

where J_μ is the hadronic part of the electromagnetic current operator and proximity of q^2 to the ρ pole is assumed. Using the notation of Figure 3 to replace the amplitude and the matrix element on the right hand side of the above equation by the coupling constants to which they are proportional, we arrive at

$$< \pi^+\pi^- | J_\mu | 0 > \sim \frac{f_{\rho\pi\pi}}{2\gamma_\rho} \frac{m_\rho^2}{q^2 - m_\rho^2 + i\Gamma_\rho m_\rho} \qquad (I.3)$$

Since our measurements involve spacelike virtual photons we need to know the behavior of the coupling strengths for $q^2 < 0$.

Vector Meson Dominance (VDM)

According to the ideas of Vector Meson Dominance the interactions of photons with hadrons are explained in terms of the ability of the photon to turn into vector mesons, V. Another common assumption, borne out by the available observations, is that the γ-V coupling constants ($g_V = 2\gamma_V$) are independent of Q^2 and have the value determined by the annihilation experiments. In the case of the ρ this means that the ratio ($f_{\rho\pi\pi}/2\gamma_\rho$) is a constant independent of Q^2.

The consequences of these simple ideas were verified by experiments, although the agreement was often unimpressive. For example, the prediction relating the total photoabsorption cross section to the sum of those for vector meson photoproduction[5] is off by approximately 20 percent, with the discrepancy presumably due to vector mesons heavier than the ϕ and to cross terms. This sort of agreement showed that one could use Vector Dominance to describe approximately the behavior of the cross sections of reactions involving photons in regions not yet covered by experiment. The domain of such predictions is augmented when the basic premises of Vector dominance are combined with the idea of quark structure for hadrons.[6]

Of particular interest to our experiment is the resulting prediction on the variation of the cross section of the reaction $\gamma + N \rightarrow \rho^o + N$ with energy. Vector dominance supplies the relation

$$f(\gamma N \rightarrow \rho^o N) \geq \sum_{V = \rho, \omega, \phi} \frac{\sqrt{4\pi\alpha}}{2\gamma_V} \; f(VN \rightarrow \rho^o N)$$

where f denotes the amplitude for its argument. However, because of the isospin change involved when $V = \omega$ and $V = \phi$, the ρ term is expected to become dominant with increasing energy. Therefore

$$\sigma(\gamma N \rightarrow \rho^o N) = \frac{\pi\alpha}{\gamma_\rho^2} \sigma(\rho^o N \rightarrow \rho^o N)$$

Simple quark models predict that $\sigma(\rho^o N) = \sigma(\pi^o N)$, thus providing a link to observable hadronic reactions. Since isospin considerations imply that

$$\sigma(\pi^o N \to \pi^o N) = \frac{1}{2} [\sigma(\pi^+ N \to \pi^+ N) + \sigma(\pi^- N \to \pi^- N)] ,$$

rho photoproduction is related to elastic pion-nucleon scattering by

$$\sigma(\gamma N \to \rho^o N) = \frac{\pi\alpha}{\gamma_\rho^2} \frac{1}{2} [\sigma_{e\ell}(\pi^+ N) + \sigma_{e\ell}(\pi^- N)] \qquad (I.4)$$

The validity of this relation can be tested by extrapolating our results to $Q^2 = 0$.

This experiment also tests the Vector Dominance prediction for the Q^2 variation of the cross section for the process $\gamma^* + N \to \rho^o + N$. For transverse rho production the cross section is expected[7] to reflect the rho propagator variation, namely

$$\sigma_\rho(Q^2) = \sigma_\rho(0) * m_\rho^4/(Q^2 + m_\rho^2)^2 \qquad (I.5)$$

omitting kinematic factors. This would seem to result from a naive generalization of the applicability of (I.3) into the region of spacelike q^2. The prediction is however based on firmer theoretical foundations, involving the basic VDM assumption of slow variation of (s-channel helicity frame) amplitudes with Q^2, with eventual independence at sufficiently high energies.[7, 8, 9, 10] This assumption

also predicts that the production of longitudinally polarized rhos will be characterized by the Q^2 variation of (I.5) multiplied by the factor R_ρ. The total cross section is then predicted to be proportional to (I.5) multiplied by the factor $(1 + \epsilon R_\rho) \equiv (1 + \epsilon \xi^2(\nu) Q^2/m_\rho^2)$. Here the quantity ξ stands for the ratio of the total ρN cross sections (that for longitudinal rhos divided by the one for transverse rhos) and it therefore varies (but slowly) with energy.

Since this Q^2 variation is predicted without any reference to the nature of the recoil N the same variation is expected to characterize the reaction $\gamma^* + d \to \rho^o + d$ as well.

Q^2 Dependence of the
$d\sigma/dt$ Slope

The ability of the photon to turn into a strongly interacting particle can be thought of as a form of hadronic vacuum polarization effect. Such a virtual transition is allowed by the uncertainty principle to last for an amount of time $\Delta\tau$ equal to the inverse of the energy violation involved. The latter is given by

$$\Delta E \simeq (m_V^2 + Q^2)/\, 2\nu$$

as long as $Q^2 \ll \nu^2$. The hadronlike behavior of the photon is expected to be more evident when the length traveled by the transition product is large compared to the "size" of

the nucleon. In our case this means that

$$\Delta\tau = \frac{2\nu}{m_\rho^2 + Q^2} > \frac{1}{m_\pi} \sim 7 \text{ GeV}^{-1}$$

When both sides of the above inequality are multiplied by the mass of the proton, the approximate condition $\omega_\rho' > 6.7$ (where $\omega_V' = 2\, m_p\, \nu/[Q^2 + m_V{}^2]$) results. This shows that virtual photons with high ω $(= \frac{2m_p\nu}{Q^2})$ are the ones most likely to exhibit this behavior. At the same time it illustrates the importance of having large ν available if one is interested in studying the process over as large a Q^2 range as possible.

These virtual transitions give a spatial extension to the parent photon, characterized by a radius R_γ. This radius constitutes a measure of the effective size of the virtual hadronic cloud associated with the photon. Such a measure is provided by the study of the Q^2 variation of the $d\sigma(\gamma^* p \to \rho p)/dt$ cross section. In common with other diffractive reactions this is given by

$$\frac{d\sigma}{dt} = A \exp\,(B_{\rho p}\, t)$$

where $(B_{\rho p})^{1/2}$ is the effective interaction radius between a photon and a proton.

The possibility of variation of this photon "size" with Q^2 has been the subject of several theoretical

investigations[11] and has been pursued vigorously by experimenters. The theories disagree about the physical mechanism responsible for such a size and consequently about the mode and amount of any variation as well. They all agree however that the most promising route for an experimental determination of the issue is provided by the study of the Q^2 variation of $B_{\rho p}$.

In an optical model $B_{\rho p} \simeq \frac{1}{4}(R_\gamma^2 + R_p^2)$ where R_p is the effective radius of the proton. Therefore, if as most models predict, there is a decrease of R_γ with Q^2 ("photon shrinkage") it will manifest itself as a slower decrease of the slope B ($\equiv B_{\rho p}$). Maximal shrinkage ($R_\gamma \to 0$) would result in a slope B of value half that of the proton-proton scattering slope at the same energy.

While a shrinking photon radius implies a decrease of $B_{\rho p}$ with increasing Q^2, the converse is not necessarily true. An observed change in B may be due to processes other than those involving a photon size. For example, when the contributions of transitions of the type $\rho' p \to \rho p$ are taken into account, they are shown[12] to predict a slow decrease of B with Q^2, if steeper t-slopes for these off-diagonal processes than for the elastic (diagonal) one are assumed. (Here ρ' stands for a higher mass vector meson of the ρ family, within the context of a generalized vector dominance model).

By measuring $d\sigma/dt$ cross sections for several Q^2 bins we are able to determine the corresponding slopes $B(Q^2)$ and thus provide experimental information on this issue from a kinematic region previously inaccessible and safely satisfying the condition $\omega_\rho' > 6.7$ throughout the Q^2 range under study.

The variable mass of the virtual photon (Q^2) clearly provides a unique and additional dimension to the study of the phenomena associated with the photoproduction of vector mesons.

Experimental Background

The most recent comprehensive review of the experimental results for the process $\gamma^* p \rightarrow \rho^o p$ is that by Wolf.[13] A comparison of several aspects of the experiments considered in that review[14, 15, 16, 17, 18] as well as of our own experiment is presented in Table 1. The Q^2 range covered in all of the experiments is roughly the same but because of the higher incident energy available in our experiment measurements with ν up to 10 times larger than in previous work could be obtained. This in turn meant that the condition $\omega_\rho' > 6.7$, which was seldom met in previous work, could be guaranteed throughout the range of our measurements.

Wolf's review showed that once all appropriate corrections had been applied the Q^2 variation of the cross section was in agreement with the VDM prediction for

$W > 2$ GeV, where $W^2 = 2\, m_p \nu + m_p^2 - Q^2$ is the total hadronic center-of-mass energy squared. However, when our experiment was being proposed there were conflicting claims regarding the steepness of the Q^2 variation. In particular, one experiment[19] had found that $\sigma(\gamma^* \to \rho)$ was consistent with being equal to $0.15 * \sigma(\gamma^* \to \text{all})$ for $Q^2 < 0.33\ (\text{GeV}/c)^2$.

The measurements reviewed by Wolf were also found compatible with the parameterization $R_\rho = \xi^2 \frac{Q^2}{m_\rho^2}$, up to $Q^2 \simeq 1.5\ (\text{GeV}/c)^2$. The value of ξ^2 was found to be slowly decreasing (with increasing W) and of the order of 0.5 above $W = 2$ GeV. For our experiment $W \simeq 14$ GeV and, given the observed decrease of R_ρ with increasing W, the value of ξ^2 is expected to be even lower than 0.5.

The question of the variation of the slope B of the t distributions with Q^2 (or with $\Delta\tau$) remained unsettled. Each separate experiment shows trends of decrease in B but they are statistically insignificant as can be seen from Figure 4. Moreover several of the measurements are either close to or even below the $\omega_\rho' \simeq 6.7$ threshold. At least one of the relevant theories (Nieh's) predicts that the slope will indeed be increasing with ω_ρ', until it reaches values of the order of 8 GeV^{-2} at $\omega_\rho' \simeq 6.7$. Decreasing slopes would therefore be expected below the threshold. In contrast the lowest ω_ρ' of our measurements is greater than 30.

Target Choice

In our experiment we wanted to study rho production in both deuterium and hydrogen targets. Since protons and neutrons are expected to contribute equally to the process a deuterium target will double the event rate.

Measurements in deuterium are of value for checking the isospin independence of the process. Moreover, with deuterium the coherent ($\gamma^* d \rightarrow \rho^o d$) production and its variation with Q^2 can be measured. The use of the same equipment and analysis methods for both targets eliminates many of the systematic uncertainties in comparing the results from hydrogen and deuterium.

CHAPTER II

THE EXPERIMENT

The experimental apparatus was set up inside Fermilab's Muon Laboratory by a collaboration of physicists from the University of Chicago, Harvard University and the Universities of Illinois and Oxford (CHIO). The general objective was to extend the study of inelastic lepton-nucleon scattering in the region of Fermilab energies. The apparatus formed a large-aperture, high resolution magnetic spectrometer designed to detect both the scattered muon and the forward-going reaction products. Thus studies of the final state hadrons as well as of the inclusive reaction could be performed.

Most of the previous studies of diffractive rho leptoproduction employed a beam of electrons. Our experiment used muons because these are more readily available at Fermilab and because muons at high energy have the advantage of smaller radiative corrections and easier identification. Given μ - e universality, the experiment was designed to provide results either directly comparable or complementary to those already available from lower energy electron beams, while exploring kinematic regions previously inaccessible.

Muon Beam

In Figure 5 we show how the Fermilab muon beam was produced. Following their acceleration to 300 GeV the circulating protons were extracted slowly from the main ring. A portion (usually more than half) of the extracted proton beam ended up heading towards the production target of the neutrino area. This target was a 30 cm (one interaction length) rod of aluminum. For pions the highest yield occurs at an energy roughly half that of the primary proton beam. Therefore, immediately after the production target a triplet of quadrupole magnets (Q1) selected all forward-going (within ± 2 mrad) charged secondaries within a wide momentum band centered on 150 GeV/c, focusing them into a 500 m long evacuated decay pipe. At this point a much more restrictive (± 2 percent) momentum selection was made by the first bending station (D1) magnets. All selected particles were then focused by a pair of quadrupole doublets (Q2, Q3) so as to converge into approximately 19 m of CH_2 hadron absorber, filling the aperture of the magnets of the third bending station (D3). The muons, which had been produced by the π decays up to this point, emerge from the absorber accompanied by a negligible ($\sim 10^{-6}$) fraction of hadrons. The last set of quadrupoles (Q4) focuses the muons onto the experimental target. The three 20' dipoles of the last bending station (D4) were used to measure the momentum of the beam muons.

They will be denoted as 1E4 elsewhere.

The resulting muon beam had a typical intensity of 750 K per accelerator pulse corresponding to a ratio of (muons/incident proton) of approximately 10^{-7}. In addition to what was electronically defined as the beam proper, a comparable and usually larger number of 'halo' muons entered the laboratory on every pulse. The halo is due to the high penetrating power of the muons. The presence of the halo gave rise to stale tracks in the spark chambers and complicated the analysis of the data.

The Apparatus

A schematic drawing of the main elements of the apparatus is shown in Figure 6. A short description of each of the components is given in the rest of this section.

Beam System

The horizontal direction of an incident muon before and after the last bending station (1E4) was measured by four multiwire proportional chambers (SO) of 8" x 8" active area with vertical readout wires, spaced twelve to the inch. The most upstream such beam MWPC is located immediately after the last beam line quadrupole magnet, which also has an 8" x 8" aperture, while the 1E4 dipoles have an aperture four inches in diameter. The wire spacing and long lever arms involved allow the measurement of a momentum in the 150 GeV/c region

with a 0.1 percent accuracy, close to the multiple scattering limit. Each one of the two beam stations (SO) downstream of 1E4 houses an additional beam MWPC with horizontal readout wires. These chambers determined the projection of the trajectory of the incident muon in the vertical plane. Thus both the momentum and the direction of the incident muon were measured. Each of the ordinates (X, Y) of the point of intersection of an incident muon track with a plane transverse to the z-axis (the nominal incident beam direction) anywhere inside the Muon Laboratory could be determined with an accuracy of approximately 0.5 mm, thanks to the long lever arm (some 31 m) between the last two beam stations.

Each of the six beam MWPC wire planes is complemented by a corresponding beam hodoscope mounted on the same stand. Each such hodoscope consists of eight scintillator strips 0.75 inch wide, 6 inch long and 0.125 inch thick (except for the most upstream one for which the width is 1 inch and the length 8 inches). The space resolution of the beam hodoscopes is worse than that of the beam chambers but their time resolution is much better (15 nsec compared to 100 nsec). Whenever there was more than one wire set in a beam chamber the corresponding beam hodoscope was used to help single out the one set by the triggering muon.

Except for the requirement that no more than a single strip of each of the pair of beam hodoscopes nearest

to the target be set, the information of the beam hodoscope and the beam chambers was not used in deciding whether to trigger the apparatus. The time coincidence of four trigger counters, one per beam station (SO), combined with the absence of a signal from any of a number of veto counters (scintillators with a circular hole in the middle) strategically located along the beam line, did however constitute one of the components of the trigger. Since this component refers to the presence of a beam signal it is denoted by B (see Figure 6). The most prominent of the veto counters was located inside the muon laboratory and is indicated by V in Figure 6. It consisted of a bank of large scintillators covering an area 3 meters high and 4 meters wide and prevented halo muons from triggering the apparatus. Directly behind this halo veto hodoscope a 1 meter thick concrete wall made sure that interactions with products traveling backwards in the laboratory would not be self-vetoed.

The Target

The liquid deuterium was contained inside a cylindrical mylar flask, 1.2 m long and 7" in diameter. The flask material presented 0.4 gm/cm^2 to the beam, roughly 2 percent of the target proper. The flask was surrounded by a thin-walled, evacuated, aluminum, cylindrical can. The upstream face of the can was far enough from the end of the flask to allow unambiguous separation of the events originating there.

The same target flask, but filled with hydrogen, was used for the proton-target studies of the collaboration.

The 1 m x 1 m MWPC

Eight multi-wire proportional chambers of large (1m x 1m) active area and with shift register readout were installed directly downstream of the target. They were grouped into four pairs (S1) each consisting of one chamber with vertical readout wires (referred to as an X-chamber in this experiment) and one with horizontal ones (or a Y-chamber). They were used to determine the trajectories of the scattered muon and of all other forward-going charged products of an interaction, upstream of the spectrometer magnet. Their good (~ 100 nsec) time resolution insured that most of the tracks detected by them were indeed associated with the interaction. Their wire spacing (16 per inch) coupled with the way they were positioned resulted in an angular resolution of 0.6 mrad. More details about the construction and mode of operation of these chambers are given in References 20 and 21.

Spectrometer Magnet

As the initials CCM indicate, the momentum analyzing magnet of this experiment was the magnet of the Chicago (Synchro-) Cyclotron.[22] The radius of the pole faces was kept at 2.2 m but the gap between them was increased to 1.5 m to increase the acceptance. The nominal field was 15 Kg and

gave a transverse momentum kick of 2.22 GeV/c to singly charged particles traversing a diameter. Only particles of momentum greater than approximately 6 GeV/c were transmitted through the magnet into the downstream experimental aperture. The cylindrical symmetry and uniformity of the field reduced the task of associating upstream to downstream tracks to a simple comparison of their impact parameters. This will be discussed later.

Downstream Spark Chambers, Hodoscopes, and Absorbers

Two sets of physically distinct spark chambers, each employing its own readout method, were used to measure the trajectories downstream of the CCM. They were arranged to maximize the solid angle acceptance with the longest possible lever arm.

The first set consisted of 12 wire planes separated into three groups (S2) each containing two spark gaps 2 m x 4 m in area. The two wire planes across each gap had a spacing of 1 mm and were arranged to form alternating pairs of U-X and X-V planes (A U wire makes an angle of $\tan^{-1}$ (1/8) with the vertical and a V wire the same angle but with a negative sign). They employed capacitive signal storage and shift register readout.[23] They could therefore operate inside the CCM fringe field and required low spark currents. Their long sensitive time (more than 2 μsec) combined with the fact that they were active in the region traversed by the

beam and with their proximity to the remnant radioactivity of the CCM resulted in many spurious sparks. They did however complement the information that could be provided by the rest of the momentum measuring planes and resulted in an improved resolution. Additional details on the construction and performance of these chambers are given in References 24 and 21.

The second set consisted of a series of 8 wire planes forming the sequence UXUXVUXV across four gaps (S3). The wire spacing was also 1 mm and the area covered was 2 m x 6 m. They employed magnetostrictive delay line readout. Unrelated sparks were reduced by deadening a 10 cm radius area centered on the deflected beam. The large currents they required for sparking set an upper limit of 15 for the maximum number of triggers that could be allowed per second. More information about all magnetostrictive readout spark chambers can be found in Reference 25.

Immediately following the second set of momentum measuring spark chambers there is a pair of hodoscopes (H, G) with crossed counter elements. They form a grid, covering most of the active region of the 2 m x 6 m chambers, that was used to separate stale from intime downstream tracks. The G counter consists of horizontal strips of scintillator and features an adjustable hole in the region traversed by the deflected beam. A signal from at least one of the G counters was required in order to trigger the apparatus.

Behind these two hodoscopes there was a 3 radiation length (2") steel plate not shown in the figure. Electrons, positrons and photons shower in passing through this plate. Four gaps (eight wire planes) of 2 m x 6 m magnetostrictive chambers, referred to as the photon chambers and also not shown in the figure, detected these showers by the presence of a cluster of sparks around the projection of the trajectory of the incident light lepton. The photon chambers were used to separate electrons from pions in some cases.

A 16 inch thick (~ 70 radiation length) lead brick wall followed by three more 2 m x 4 m spark chamber gaps was positioned directly behind the photon chambers for the purpose of inducing and detecting showers by neutrons. These so called neutron chambers, again not shown in the figure, were not used in the data analysis.

All particles other than muons were stopped in the final absorber (A) which consisted of staggered steel blocks, 8 feet thick. Here the penetrating power of muons was used for their identification.

The main veto counter of the experiment, the N hodoscope, was situated behind the hadron absorber. It consisted of 13 horizontal counters, each 66 cm long and 7.7 cm wide arranged to overlap halfway, thus covering an area 54 cm wide and 66 cm long. Its purpose was to veto the muons of the beam that had either not interacted or had undergone

little energy loss. Its position sideways (in the x-direction) was adjustable. The requirement that none of the N counters be set was one of the components of the trigger of the experiment.

Accurate temporal and rough spatial information about muons penetrating the hadron absorber was provided by the set of M and M-prime hodoscopes. As shown in the figure the M counters were horizontal and the M-prime vertical. Their combination therefore forms a grid similar to that of the G and H hodoscopes. Details about all hodoscopes of this experiment are given in Reference 26. The relevant triggering requirement was that at least one of the M or the M-prime counters be set, indicating the presence of a scattered muon.

The trajectories of muons downstream of the hadron absorber were determined by the last set of magnetostrictive chambers (S4). Four chambers, each containing two wire planes of 2 m by 4 m active area, formed this set which was referred to as the muon chambers.

Electronic and Physical Trigger Components

The apparatus was triggered whenever the electronic coincidence $B \cdot \overline{N} \cdot (M \text{ or } M') \cdot G$ was satisfied. The objective was to preferentially detect the muon-nucleon interactions occurring in the target while minimizing the fraction of the triggers due to extraneous processes.

The signal B (see Figure 6) guarantees both the presence of an incident muon of approximately the correct beam energy and the simultaneous absence of a halo muon. Muons interacting upstream of 1E4 move out of the beam spot and are vetoed by the several small veto counters along the beam line, which are an integral part of B. To insure that the incident muon has not interacted between 1E4 and the muon laboratory, the requirement that no more than one of the elements of each of the two beam hodoscopes nearest to the target be set was made part of B. Since muons arrived in "buckets" 18 ns apart (reflecting the frequency of the RF acceleration in the main ring) this requirement also insures that the bucket contains only one beam muon. This avoids an event veto by a companion beam muon not interacting in the target. Similarly, a companion halo muon outside the beam aperture will be detected by the halo veto hodoscope, which prohibits the formation of the signal B.

The signal $\overline{N}$ vetoes any event in which the muon was not scattered enough to miss the N counter. The size of the N counter was chosen large enough to veto, in addition to the unscattered beam, a large fraction of the more numerous low Q^2 events and so prevent them from saturating the trigger. The probability that two beam muons arrive in the same RF bucket was measured to be 0.06 ± 0.02, varying with the beam tuning of each run. Since the beam and halo fluxes are

approximately equal, accidental halo-beam coincidences occur at a similar rate. It was therefore necessary to install a highly efficient N veto counter. Otherwise, there would have been accidentals with the beam muon providing the B and the accompanying halo muon, undetected by the halo veto, providing the M·G.

A set M or M' hodoscope counter, in the absence of an N signal, indicates the presence of an interacting muon inside the aperture of the detectors.

Since the G hodoscope has a hole through which the deflected non-interacting beam passes, the G counters can only be set by the scattered muon or by the products of the interaction. A G signal therefore indicates that the interaction took place upstream of the plane of the G hodoscope, given that we already have a $B \cdot \overline{N} \cdot (M \text{ or } M')$ coincidence. Without the G requirement triggers from muons interacting in the absorbers downstream of G would have overwhelmed those due to interactions within the target because of the disparity between the amounts of material involved.

The only trigger component which could be adjusted was the position of the N counter across the beam. Vertically the counter was centered on the nominal beam height. The horizontal position adopted for data taking was chosen following a study of the behavior of the triggering and other rates, with the N counter traveling across the beam and

always containing most of it. The results of this study are presented in Figure 7. The chosen operating point was a compromise between the conflicting objectives of minimizing the triggering rate and of being insensitive to small changes in the beam spot, position, and shape. The triggering rate $[B \cdot \overline{N} \cdot (M \text{ or } M') \cdot G/B]$ indeed remained inside the $(9.5 \pm 0.6) \times 10^{-6}$ range throughout the data taking. The target empty rate was approximately half of the target full value.

The anticipated triggering rate due to muon-target nucleon interactions[27] was of the order of 2×10^{-6}, for any reasonable position of the N counter. A muon could however also lose energy in the target by scattering elastically off an electron or by bremsstrahlung. Our acceptance calculations showed that in addition to the beam the N counter would also veto all scatterings with $Q^2 < 2\ (\text{GeV}/c)^2$ as long as ν is less than roughly 90 GeV. The μ-e elastic and muon bremsstrahlung interactions are characterized by low Q^2 (small angles) and their cross section decreases with increasing ν. Therefore the N counter prevented most of such interactions from triggering. Even so, since for $\nu > 90$ GeV interactions of any Q^2 would trigger the apparatus, the triggering rate from μ-e elastic scatters was also approximately 2×10^{-6} while that from muon bremsstrahlung was about half as large. A small fraction

of the recorded triggers was due to various combinations of accidental coincidences which satisfied the triggering criterion. Examples are positrons from beam μ decay setting B and G in random coincidence with M or M' and beam muons interacting downstream of G (setting $B \cdot \bar{N} \cdot$[M or M']) in random coincidence with G.

Different triggers, such as 'B' alone or 'Halo', were occasionally employed to record information necessary for surveying, normalization, and monitoring purposes. The $B \cdot \bar{N} \cdot$(M or M')$\cdot$G trigger was the only one used for data taking. The primary objective of this trigger is to facilitate the study of the inclusive reaction. A large fraction of diffractive rho events was not observed because, in pursuit of this objective, the N counter was set to veto low Q^2 events with $\nu < 90$ GeV. For this reason and since we want to study just one exclusive channel, the number of events in which a rho is diffractively produced is expected to constitute a small fraction of the triggers. The numerical value of this fraction depends strongly on the nature of the Q^2 dependence of the cross section for the diffractive process. The value predicted by Vector Dominance, using Eq. (I.5), is of the order of 0.005 and is lower than any of the other expectations.

Data Acquisition

Information from physically dissimilar detectors such as counters and wire chambers, as well as from auxiliary pieces of equipment, such as scalers, had to be recorded. A CAMAC system was therefore used in order to standardize the end products of the electronic readout systems and to facilitate the interfacing to the online computer. The information was stored in CAMAC modules (scanners for the chambers, latches for the counters and quad scalers for the scalers) prior to being transferred to the computer. Although each such module consisted of distinct hardware, designed to encode the information according to a predetermined convention, they all shared two common features: Their sequence of operations was initiated by a "prompt out" i.e., a signal generated by the fast electronics of the experiment no later than 6 μsec from the moment the triggering criterion was satisfied; and when their operations had been completed they issued a "look-at-me" (LAM) indicating to the computer that data transfer was allowed and desirable.

The following sequence of events took place every time the triggering criterion was satisfied: The scalers were stopped and the circuit that produced the trigger was disabled to insure that the recording of the event would proceed uninterrupted. The scaler and counter information

was read out and stored into their respective CAMAC modules. A strobe signal was sent to all proportional chambers, freezing the information from each wire into its respective shift register. Some 300 nsec later the spark chambers were fired. After the noise from the sparks had died down, some 5 μsec later, the "prompt outs" initiating the transfer and encoding of the chamber information into their respective scanners were sent. In less than 5 msec all modules had issued their LAM. The computer was then interrupted and began the process of transferring the event data through the CAMAC interface into its fast memory, in 600 (16 bit) word blocks, filling up to four (but typically two) such blocks per event. This process lasted for some 50 msec on the average. The scalers and the triggering circuit were then enabled and the sequence was repeated following the occurrence of the next trigger.

There were twenty 600-word blocks available in the computer memory. Since the average triggering rate was four per pulse and since most of the events would need no more than two such blocks in which to store their information (the number of sparks being the only variable quantity) the twenty blocks proved adequate for most of the spills. On the few occasions that seventeen or more of these blocks had been filled, the computer gated the experiment off for the rest of the spill so as not to allow a bias in favor of events with fewer sparks.

The first task of the computer during the five second interval between spills was to copy the contents of this memory buffer onto tape, again in 600 word records. At tape density of 800 bpi, up to 5000 triggers could be recorded on a single tape forming a unit which was called a run. Shorter runs were however often necessitated by malfunctions of the equipment, loss of the beam, or computer problems. Additional information about the structure and the contents of these so-called raw data tapes can be found in Reference 28.

The online computer, a Xerox Σ-3 featured a hardware priority-interrupt system. Event acquisition had the highest priority, followed by the logging of the data on tape. In addition to these two tasks the computer also performed a host of useful checks both at the individual event level and on a statistical basis. It therefore served as a monitor of the proper functioning of the equipment, pointing out to the experimenter problems that might have otherwise gone undetected until the data was analyzed off-line. Details about these and other functions of the on-line control system and software can be found in References 21 and 29.

There were 64 usable runs corresponding to a flux of 2.628×10^{10} muons incident on the full liquid deuterium target during the time that the apparatus was in a position to be triggered. Approximately two hundred and fifty thousand recorded triggers formed the dataset on which this study was based.

CHAPTER III

DATA REDUCTION

The rudimentary information about each trigger, such as the location of the sparks within each chamber and the set elements of the various hodoscopes, recorded online on the raw data tapes had to be transformed to make them useful for the extraction of physics results. A two-step process, with the output of the first serving as input to the second, was employed to reduce the contents of these tapes to a more suitable form. In the first step the alignment of the active elements of the apparatus was determined for each run and then the real space coordinates of the sparks were calculated and recorded on secondary ("scaled data") tapes. The core of the second step consisted of trackfinding programs which used the scaled data to determine the tracks of charged particles. The parameters from which these tracks could be reconstructed were then written onto tertiary (data summary) tapes.

The secondary and tertiary tapes were produced by other members of the collaboration at the Rutherford Laboratory's IBM 360/195. The physics analysis reported in this thesis was performed at Fermilab's CDC 6600 and at the University of Chicago's IBM 370/168, using the tertiary tapes

as the starting point. The rest of this chapter describes the raw → scaled → tertiary reduction process in detail.

Secondary Data Tapes

The coordinate system with respect to which the positions of the chambers and their sparks were measured was a right-handed one with the positive z-axis along the nominal incident beam direction and with the positive y-axis pointing upwards along the vertical. The center of the CCM was chosen as the origin.

To determine the real space location of each spark we needed to know the alighment of the various chambers. The starting point for alignment was provided by the two pairs of beam MWPC downstream of 1E4. These chambers had been positioned by surveyors so that the line joining the centers of their active areas coincided with the z-axis and so that their readout wires stretched along the vertical or the horizontal directions. Therefore the absolute (with respect to this coordinate system) value of the ordinate of their set wires could be easily deduced. Whenever one and only one wire was set in each of these four chambers, the incident muon track was unambiguously and absolutely determined. Due to the relative distances involved the projection of such a track onto any chamber plane downstream of the target was predictable to within .7 mm, a length comparable to the intrinsic space resolution of the chambers. With the CCM

turned off the position of each chamber transverse to the z-axis could then be determined as the one minimizing the square of the difference between observed and predicted intercepts of the muon track.

The alignment of the 1 m x 1 m MWPC was determined once and for all by this method. However, variations in the temperature of the muon lab resulted in changes in the speed of sound and thus in the calibration of the magnetostrictive lines, making necessary a separate alignment procedure for each run for the rest of the apparatus. First the relative positions of the twenty momentum-measuring planes downstream of the CCM were determined by considering iteratively the tracks through these planes which had been found in the first few hundred events of each run. The absolute position was determined by linking tracks through the CCM. Tracks in the x-z plane were matched by minimizing the difference of their impact parameters; at the same time the consistency between the beam height and the projection of the downstream tracks back to the target was optimized. (The vertical focussing was negligible.) This procedure required knowledge of the absolute positions of the MWPC's upstream of the CCM. The only other group of chambers for which alignment was indispensable were the muon chambers. Here the non-linear response of two wands had to be corrected for and then the relative alignment of the chambers determined using tracks through the chambers. Finally, the set was aligned as a

unit with respect to the downstream momentum-measuring planes, by matching muon tracks.

The alignment procedure was complicated even further by an intermittent malfunctioning of the BMWPC readout hardware: It turned out that for some of the runs the 5 μsec (following a trigger) during which the clock line was blocked was not always long enough for the spark chamber noise to die down. As a result the BMWPC data would be shifted by the same number of counts in each of the chambers but this number would vary from trigger to trigger. Fortunately the beam runs, which were interspersed among the data runs, served to fix the alignment between the beam chambers and the corresponding beam hodoscope elements. (The spark chambers were not energized during beam runs.) The known position of the hodoscope elements and the nature of the defect (a uniform shift) were in turn utilized to establish a reverse shift that provided the best match between beam chamber and beam hodoscope information for all the triggers of a data run. Deviations of ± 2 wires, compared to 9 wires per hodoscope element, were then allowed for individual triggers for which this reverse shift had not removed the discrepancy. It was estimated[25] that less than 10 percent of the triggers may have been processed with a shift off by 1 wire. At any rate the effect on the resolution of the kinematic quantities is negligible. Also, since

only a translation is involved, no change in the momentum determination by 1E4 had to be made. In the data taking that followed this experiment the problem was solved by increasing the blocking time and by incorporating fiducials (i.e., wires set all the time).

A less elaborate alignment process would have sufficed if there were fewer stale and noise sparks mixed in with the real ones. Their presence made the use of the full resolving power of the detectors necessary for efficient and reliable trackfinding. In any case, once the locations of the chambers had been determined for each run, the spark information was converted to real space coordinates, which were then recorded onto the secondary (scaled data) tapes along with the counter counts for each event.

Event Reconstruction

The event reconstruction process had the following objectives:

(a) To identify all the tracks of charged particles traversing any segment of the apparatus,

(b) To determine the temporal relationship of every such track to the moment that the triggering interaction took place,

(c) To pick out the track of the triggering muon,

(d) To determine the coordinates of the interaction vertex, and

(e) To calculate the momentum of every particle emerging from the vertex and detected downstream of the CCM and to determine the kinematic quantities, such as Q^2 and ν, associated with the event.

Only a fraction of the recorded sparks was associated with the interacting muon or with the products of the interaction. The rest were caused by stale muons, by the residual radioactivity of the CCM and by "noise." Each spark was either assigned to a track of a particle traversing the apparatus or discarded as extraneous in the first step in the event reconstruction process.

Four different and independent programs performed the trackfinding, one for each of four regions into which the chambers were allocated according to function. These were: (a) The beam region (encompassing the beam chambers), (b) The upstream region (containing the 1 m x 1 m MWPCs), (c) The downstream region (containing the momentum-measuring spark chambers), and (d) The muon chamber region. By linking the track segments at the boundaries of adjacent regions the path of a particle could be traced through the apparatus. Also, cross-checks could be made and the efficiency of individual pieces of the apparatus as well as of the trackfinding routines themselves could be determined. If a sequential procedure had been used, i.e., one in which the results of the trackfinding in one region were used as seeds

for the search of an adjacent region, such measurements, necessary for the extraction of cross sections, would have been much more difficult.

Trackfinding by Region

In the beam region the fine spatial resolution of the beam chambers, was combined with the superior time resolution of their associated beam hodoscopes to identify the path of the incident muon prior to the interaction point. Set wires having a set hodoscope element right behind them were selected as the true indicators of the point of traversal over any other set wires in the same chamber. If no wires were set the center of a set hodoscope element was used except for the case of the x-y pair in front of the target. Here the existence of set wires was required because it was essential for limiting the road within which the interaction vertex could lie.

The beam-region trackfinding was designed to assure a sensible, clean,and unambiguous incident muon track at the expense of efficiency. As a result the efficiency was typically 68 percent for the trigger (data) runs and 80 percent for the beam runs, with the difference coming from the sensitivity of the trigger to muons losing energy upstream of the target and to the contribution by random coincidences to the "beam" signal. Since failure to identify a clean incident muon track meant that the processing of the event was abandoned, a correction for the possible loss of events

had to be applied. This is discussed in Chapter V.

As in the case of the beam region the trackfinding in the 1m MWPCs was done separately for the X and the Y views. All 3 or 4-spark tracks (there were three Y and four X chambers) pointing to the incident muon track inside or upstream of the target were found. Tracks more than 2 percent probable were kept unless they shared more than two sparks with another track of better chisquared.

In the 2 m x 4 m and 2 m x 6 m spark chambers there were no planes wired to give the y coordinate directly. Instead the y coordinate of a spark was deduced by incorporating the information provided from the tilted ($\frac{dy}{dx} = \pm 8$) plane of type U or V, across the gap from a type X wire plane. Since each plane usually records more than one spark several possible (x, y) pairs are formed for each gap. Such a pair is acceptable if its y falls within the physical y-boundaries of the chamber. The spark chamber trackfinder operated on groups of four adjacent gaps, considered to contain such (x, y) pairs of scaled data, in the following manner.

The most negative x spark of the group was first chosen and a strip, centered on the spark and of variable width proportional to the absolute value of the spark, was laid down across all four gaps. A search was made within the strip to see if it contained at least two more x-sparks in the remaining gaps. In either case the procedure was

repeated for the next most negative x-spark in the group. Whenever the search was successful a straight line fit and chisquared calculation were performed, assuming an error of 1.25 mm for the position of each spark. This is generous compared to the resolution of 0.5 mm but still an effective guard against confusion given a typical double spark separation of some 17.5 mm. Fits surviving the chisquared cut were identified with a track's projection onto the x-z plane. The associated y sparks were then treated in a similar manner to determine the y-z projection. Because the resolution in y is a factor of 10 worse than in X the assumed y-spark position error was 15 mm. Sparks assigned to a track were removed from any further consideration by the trackfinder.

The procedure outlined above was applied first to the four muon spark chamber gaps and then independently to the four 6 m momentum measuring gaps. In the case of the latter set the tracks found constituted a starting point for a search through the 12 capacitive readout spark chambers immediately upstream. The extrapolation of the 6 m track in the X-view served as the center of a 25 mm-wide road within which the associated sparks were required to lie. A line connecting the height of the incident muon at the center of the target to the height of the y-track at the 6 m chambers served the same purpose in the Y-view. If six or more sparks were found inside the road a new fit in X, U

and V was done allowing for as much as 1.75 mm error per spark. If the chisquared exceeded this cut the sparks contributing the most were suppressed and the fit was redone. If this too failed then the center of the road was allowed to swing by as much as 15 mm on either side of its original position at the most upstream shift register plane (with correspondingly less allowance for planes further downstream) and a new search and testing were initiated. The extrapolation aimed to lengthen the lever arm along which the downstream track was measured thereby improving the accuracy with which the track parameters could be determined.

The two types of spark chambers were not treated on the same footing for the downstream trackfinding due to the observed difference in the density of sparks recorded by them. The magnetostrictive readout (6 m) chambers had a deadened region at the location of the deflected beam. They were also further away from the CCM than the capacitive readout (4 m) chambers and had therefore fewer extraneous sparks. Thus they gave a more manageable number of (X, Y) pairs which served as seeds for the downstream trackfinding. (Even so, we needed of the order of 100 msec per trigger to carry out the downstream trackfinding.)

Linking of Upstream and Downstream Tracks

The cylindrical symmetry of the CCM simplified the process of linking of the upstream and downstream tracks found so far. In the bending plane, the field is adequately described as having a constant strength with a sharp edge of effective radius R. With reference to Figure 8 the path of a particle is then the segment of a circle such that the entry and exit trajectories are tangents at points A and B. The symmetry about the line joining the center of the magnet (O) to the center of this circle (C) requires that the impact parameters (b) to the entry and exit trajectories be equal. The observed distribution of the difference (b[upstream]-b[downstream]) had $\sigma \simeq 2$ mm and tracks for which this difference was less than 8.75 mm were considered to be linked in X.

Since the X and Y tracks found upstream were not associated, separate linking was necessary in the y-z plane. Compared to the resolution with which track slopes and the intercepts at z = 0 were measured the effect of the magnetic field was negligible and each Y track could therefore be parametrized by a straight line. Two Y tracks on opposite sides of the CCM were linked if they satisfied the relation:

$$\left(\frac{\delta\,\text{slope}}{6\ \text{mrad}}\right)^2 + \left(\frac{\delta\,\text{intercept}}{2\ \text{cm}}\right)^2 < 1$$

where δ denotes the difference of the values of its subscript for the downstream and upstream tracks under examination. As was also the case for the x-z view each track was allowed to link to as many as four different tracks from the other side of the CCM, leaving to a later stage the decision which linkage should be ascribed to the event.

Completion of Trackfinding

To recover from inefficiencies of the detecting equipment and/or of the region-by-region trackfinding programs the tracks found in one region were used as seeds for further trackfinding in adjacent regions.

The impact parameter of upstream X-tracks and a single (x, y) 6-meter chamber spark, masked by set elements of the G and H hodoscopes, defined the center of a 1 cm wide road within which searches for more sparks in the downstream planes were performed. In the beam region about 10 percent additional tracks were identified this way. Next, the intercept at z = 0 of downstream tracks was used as the starting point for searches for two-spark upstream tracks. Since there were only 3 1 m x 1 m Y-planes this procedure helped reduce the dependence of the trackfinding efficiency (in the upstream region) on the efficiency of the individual MWPC planes. Because such so-called two-point tracks were almost always found, additional criteria, to be described later, were used to establish their legitimacy.

Timing of Tracks

The fine time resolution and high efficiency of the counters of the G, H, M, M' and N hodoscopes were relied upon to determine the temporal relationship of all downstream and muon tracks to the moment of triggering. The dimensions of the hodoscope elements were first enlarged (by 1 cm in X and by 3.81 cm in Y) to allow for survey and track projection uncertainties; the number and the identity of set hodoscope elements along each track's projection were then determined. Depending on the details of the geometry various grades of timing agreement could be assigned but basically tracks were categorized as either "intime" or as "out of time" or stale--the latter occurring when not a single counter along the track's projection was set. The relevant hodoscopes were M and M' in the case of muon chamber tracks and G and H for the downstream tracks.

Linking of Downstream and Muon Tracks

The next objective of the event reconstruction process was the identification of the path of the muon which caused the triggering. To this effect the linking of the downstream and muon chamber tracks was first examined. The momentum-dependent multiple scattering effects of the lead wall and the hadron absorber (located between the two regions) complicated the linking process here.

In the x-z view the effects of multiple scattering and of the track resolution from either side of the hadron absorber were comparable. Therefore, to establish linking in X the difference of the projection of the tracks to the middle of the hadron absorber was used. This difference was scaled by a factor compensating for the proportionality of the mean multiple scattering angle to the inverse of the muon momentum and then a cut of ± 5 cm was imposed, independent of momentum. The difference of the X-slopes of the two tracks under consideration, again appropriately scaled for momentum, was simultaneously required not to exceed 15 mrads.

Multiple scattering in Y is the same as in X but the resolution of the Y tracks is much worse than that of the X tracks. Given the lever arms involved the resolution errors from the upstream and the muon Y tracks were comparable close to the most upstream muon chamber. There the additional requirement that the difference between the Y-intercepts should not exceed 15 cm was imposed. Since in this case both the x-z and the y-z views of each track under consideration were known, and since multiple linking was not acceptable here, this loose cut in Y served only to reduce confusion. If multiple links were not eliminated after the Y cut was imposed then the tracks with the best matching X-intercepts were declared as the only linked ones. No restrictions were

imposed on the total number of possible downstream-muon track links per event (i.e., all possibilities were given an equal chance).

Identifying the Scattered Muon

The downstream track due to the scattered muon should normally (a) be intime and it should (b) link to an upstream and (c) to a muon chamber track. Features (a) and (b) were required of all scattered muon candidates but (c) was not. In such cases, downstream tracks whose projection pointed to at least one set M or M' counter and to a cluster of muon chamber sparks became scattered muon candidates. For both types of candidates the quality of intimeness was graded depending on the ratio of the number of counters pointed at and set to the number pointed at. In addition at least three of the maximum possible four counters had to be set before either a projected downstream track or a downstream track linked to a muon chamber track would be declared to be the scattered muon. Since all these criteria were found to be satisfied by more than one combination of downstream-muon chamber tracks in approximately 1 percent of the reconstructed events, the combination with the best quality was chosen as the scattered muon. There were, however, provisions for recording the relevant information for up to 3 such eligible combinations per event. The validity of the choice could be questioned later using additional criteria, like the energy balance.

For approximately 30 percent of the reconstructed events (or 15 percent of the triggers) no combination or projection satisfying the above mentioned criteria was found. All the information about such events was however recorded on the tertiary data tape. Only triggers for which either no clean incident muon or no downstream tracks were found were considered as reconstruction failures and were therefore omitted from the summary tapes.

Determination of the Interaction Vertex

The upstream track that linked to the downstream portion of the scattered muon track was used in conjunction with the incident beam muon track to tentatively identify the vertex of the interaction. All upstream tracks which linked to intime downstream ones and passed close to this vertex were then incorporated in a subsequent recalculation of the vertex. Thus the interaction vertex for multiparticle (here meaning more than two) final states was accurately known even if Q^2 was close to the kinematic limit, provided that at least one of the angles with the incident muon track was large compared to the 0.6 mrad angular resolution of the upstream tracks. Most of the events of interest in this study possess these features, making their association to the target easy to ascertain.

To allow for the possibility of secondary interactions within the target and for having selected the wrong

candidate for the scattered muon up to 5 vertices could be recorded. These were the 3 vertices located furthest upstream from which emerged tracks linking to downstream ones and the 2 most upstream vertices which had no such tracks associated with them.

Calculation of Kinematic Quantities

The accuracy with which the impact parameter was measured from downstream was much better than that from the proportional chambers upstream, due to the longer lever arm and to the larger number of sparks associated with the track. The scattering angle in x for each upstream track was therefore determined by drawing the tangent from the x position of the vertex to the circle having the center of the CCM as its origin and with radius equal to the impact parameter as measured by the downstream linked track. The momentum p in GeV/c of a particle which travels along a circle of radius ρ meters inside a cylindrically symmetric field of radius R meters and constant strength B kilogauss is given by:

$$p = 0.03\ B\rho$$

The hard edge model of the CCM field used is described by R = 2.4709 m and B = 15 kilogauss.

From Figure 8 it can be seen that:

$$\rho = CD + DB = (R^2 - b^2)^{1/2} \cot\left(\frac{\theta}{2}\right) \pm b$$

where the angle ABC = $\theta = \left| |\theta_{out}| \pm |\theta_{in}| \right|$ and the + (-) sign applies to trajectories of opposite (same) sign slopes. Thus the vertex and the downstream track provide all the quantities necessary for the determination of the momentum of the particle in the x-z plane. This is also true for the y-z plane where the height of the downstream track at its mean z was used in conjunction with the y of the vertex to determine the scattering angle in y, following the application of simple vertical focussing and helix effect corrections. A momentum could thus only be assigned to those downstream tracks which linked in at least one view with an upstream track.

Given the vector momenta, kinematic quantities such as Q^2 and ν were determined according to their definitions.

Trackfinding Efficiency

It was one of the features of the design of our experiment to provide the maximum amount of redundancy allowed by the space limitations. The availability of many more than the minimum number of planes necessary for momentum determination eased enormously the task of identifying the tracks in the crucial downstream and upstream regions of the apparatus. At the same time the trackfinding efficiency was rendered largely independent of the efficiency of individual chambers. The importance of this built-in feature cannot be overemphasized.

Due to another design feature, however, it was anticipated that the efficiency to detect a downstream track should depend on the X intercept of the track at the 6 m chambers, which provide the origin of the trackfinding in this region. The reason for this complication was that these chambers had a dead area (10 cm in radius) in the beam region, where the density of tracks was peaking due to the intense halo around the beam. Special studies were undertaken to measure this effect.

The efficiency of the trackfinding process was defined as the probability of detecting the presence of a random track, externally added to real events at the secondary tape level. Fake tracks were generated so as to be beam and target-associated and to cover the aperture of the detecting apparatus. At the point where such tracks traversed a chamber, sparks were generated so as to correspond, on the average, to the measured individual detection characteristics of the piece of apparatus involved. In addition to efficiency and resolution, particular attention was paid to simulating the spread of the sparks. The trackfinding programs were then allowed to operate on the modified event and the results were checked to see if the inserted fake track had been detected. As it was pointed out in the first of a series of reports on such tests,[30] this method has the advantage of using the background sparks present on the data tapes rather than trying to simulate them.

These studies gave us the overall downstream trackfinding efficiency and determined its variation as a function of X at the 6 m chambers. As expected, the inefficiency was found to be strongly and positively correlated with the density of tracks. The results of the most exhaustive of these studies[31] are shown in Figure 9. The peaking of the inefficiency occurs in the region of the chambers around the deadener and is attributed to the increase of the confusion near the beam. (The inefficiency is 100 percent inside the deadener). Figure 9 is the parameterization of the downstream trackfinding efficiency used by the Monte Carlo program which calculated the acceptance for the reaction under study (see Chapter V).

Tertiary Tapes

Once the analysis of an event had been completed the reconstruction program wrote all its findings on a tertiary tape and then proceeded with the analysis of the next trigger. The information recorded included the track parameters for the incident muon and for the tracks found in the upstream, downstream, and muon chamber regions as well as their linking. The vertex and its error matrix, kinematic quantities and the vector momentum assigned to downstream tracks were also written on the tertiary tapes. The counter latching information and two sets of scaler counts, one associated with the trigger and one accumulated since the last event that was

written on the tertiary tape, were taken or deduced from the secondary tapes and were also recorded.

A full description of the information available on the tertiary tapes and of the format with which it is written is given in reference 32. Basically there are two buffers, one for the track parameters and another for the momenta. A set of pointers indicates the beginning of the various types of tracks in the track buffer and another stores the assignment of a momentum vector to its downstream track. An illustration of the kind of information available for each event on a tertiary tape is presented in Figure 10. Slopes are given in units of tenths of radians and intercepts in 1/4 mm. By expressing distances along the z-axis in units of 1/4 cm, the product of a slope times a z-distance in these units is also expressed in 1/4 mm, and is thus directly comparable to other distances transverse to the z-axis such as the (x, y) coordinates of the vertex.

Except for indicating whether a scattered muon had been found no attempt was made at this stage to classify the type of trigger (inelastic nuclear scatter, muon-electron elastic scatter, muon-bremsstrahlung, spurious, etc.) to which each event on the tertiary tape belonged. This was left up to the users of the tapes, offering them the opportunity to experiment with and define their own selection criteria and correction factors.

In addition to their use as data summary tapes, the tertiary tapes served as input to programs which determined the efficiency and other properties of individual detectors or their components. Also, several of the correction factors, necessary for the extraction of absolute cross sections, were deduced from the output of special programs which operated on the contents of the tertiary tapes. The methods employed are presented in Chapter V.

CHAPTER IV

EVENT SELECTION

This chapter describes in detail how events were identified as candidates for the reaction under study and outlines the process of their selection from a dataset consisting of over 100,000 analyzed triggers. The methods employed for both the selection of events and for the evaluation of the cross sections (the latter are described in Chapter V) also apply, unless otherwise stated, to the results[33] from our hydrogen target data.

Halo Rejection

Some of the tracks found downstream of the CCM were not associated with the interaction of the triggering muon. Most of the events contained at least one such extraneous track, thought to be due to halo muons traversing the apparatus within the sensitive time of the spark chambers (over 2 μsec) prior to the moment of triggering. The recording of such tracks was expected since the halo intensity was of the order of the muon beam itself and halo muons were spread throughout the aperture of the detectors. By definition these tracks are out of time, that is normally the counter elements to which they are pointing are not set. From the

measured muon-nucleon interaction rate and the parameters of the muon beam it was calculated that the probability that an out of time track was due to a hadron from an earlier (non-triggering) interaction was negligible. The data verified this expectation, thus allowing us to assume safely that all extraneous tracks were produced by halo muons and nothing else.

In order to identify a specific final state (an exclusive channel) it is necessary to be able to count the number of hadrons produced at the interaction vertex, trigger by trigger. For counting to be possible, tracks must first be separated into genuine and extraneous. After long investigations the set of criteria described below was used to make this decision in a consistent manner.

First, the linking between the downstream tracks and the muon chamber tracks was investigated. The objective was to identify which of the tracks were produced by particles other than muons. Only downstream tracks that had been assigned a momentum were of interest and they were labeled as halo if they were found to be unambiguously linked to any muon chamber track. The sole exception was, of course, the track that had already been assigned to the triggering muon. In addition, any other track that linked to the muon chamber track segment of the triggering muon was retained, attributing the linking to geometrical coincidence. In the

same spirit, if an out of time muon chamber track linked to more than one downstream tracks of which only one had been assigned momentum, the latter was not flagged as halo, giving it the benefit of the doubt (but still subjecting it to the rest of the tests described below). Under all other circumstances a "hadron" (meaning non-muon) downstream track which had been assigned momentum and which linked to a muon chamber track was labeled as halo and the count of "hadrons" for the event was decreased by one.

Downstream tracks were assigned momentum if they were not clearly out of time and if they linked to an upstream track. Although the momentum was calculated assuming that the hadron originated at the vertex of the interaction no checks were made to insure that either the downstream track or the upstream track(s) to which it linked were indeed pointing towards the vertex. The next two tests were designed to impose this requirement.

Since the tracks are bentin x by the CCM, only the y projection from downstream can be checked. Figure 11 compares the distributions of the difference between the y of the downstream projection, evaluated at the z of the vertex, and the y of the vertex for negatively and positively charged "hadron" tracks. The distribution of the positives has wider wings indicating the existence of halo muons in that sample of tracks. (The histograms shown correspond to all downstream tracks that were assigned momentum, irrespective

of whether they had been labeled as halo.) This was confirmed by examining the same distribution for downstream tracks that linked to an out of time muon chamber track. After taking into consideration these as well as the histogram from the scattered muon it was decided to label a downstream track as halo if the absolute value of this difference exceeded 200 1/4 mm.

Downstream tracks could link to as many as four upstream ones. At least one of the latter should project within a reasonable distance back to the vertex. To decide on the amount of a cut we studied the distribution of this distance for tracks linked to downstream tracks already identified as halo. This distribution peaked at zero but had wide wings. For approximately half the links the absolute value of the distance was less than 30 1/4 mm. A much more strongly peaked distribution of this distance resulted when the linkage was to downstream tracks not yet identified as halo. For the x-z tracks this is shown by the continuous line of Figure 12. Assuming that all of the links to tracks missing the x of the vertex by more than 30 1/4 mm are accidental and that the rest of the accidental links are equal in number and distributed as those of the halo inside the ± 30 1/4 mm region, results in the estimate for the background shown by the dashed line in Figure 12. This represents the maximum possible background since all linked upstream tracks--not

just the one projecting closest to the vertex--were considered. It was decided to apply a generous and safe cut at ± 30 1/4 mm, within which up to 18 percent of the links could be accidental, and to rely on the event selection criteria for the final weeding. Similar results were obtained for the projections of the y-z upstream tracks, for which the same cut was also applied. For the purposes of this test two-point upstream tracks with poor chisquared (greater than 625 for x tracks or greater than 1250 for y tracks) were considered as not linking to the downstream track in question.

To illustrate the effectiveness of the various cuts the results from a representative sample of tertiary tape events which contained 20436 downstream "hadron" tracks that were assigned momentum are presented in Table 2. At the end 7404 of these tracks had been declared as halo. The percent shown is the number of events failing either only one of the three tests described above or a combination thereof, divided by 20436.

Once all tracks had been tested the momenta of the ones surviving all the tests were added and their sum was subtracted from the energy loss ν of the scattered muon. If this difference was greater than 5 GeV the momentum buffer was searched for the existence of a track that would provide the missing downstream energy. (Particles of momentum less than about 5 GeV could not have traversed the CCM.) If the

absolute value of the difference between ν and the new total downstream energy was less than 5 GeV the halo label was removed from the track. If more than one such tracks were found the one providing the closest energy balance was preferred. The objective of this reversal of opinion was to allow us to recover from possible misidentifications of genuine hadrons as halo particles. Both the hadron track in question and the event were branded, however, so that they could later be checked for systematic differences from the rest of the events in the sample. No obvious differences were found, vindicating the adoption of this precautionary measure.

At long last the number of "hadron" tracks for each event could now be ascertained; it was defined as the number of downstream tracks assigned momentum which were not labeled as halo or as part of the triggering muon path.

Selection Criteria

A distinguishing feature of the downstream topology of the reaction

$$\mu^+ + N \rightarrow \mu^+ + \rho^o + N, \ \rho^o \rightarrow \pi^+ + \pi^- \qquad \text{(IV.1)}$$

is the presence of just a pair of oppositely charged particles, in addition to the scattered muon. The few recoils with kinetic energy large enough to emerge from the target do not aim towards the CCM. So all events with this topological

signature downstream are candidates provided that they also balance energy within reasonable limits.

The process of selection of candidates for the reaction (IV.1) began by requiring this characteristic downstream signature: Events with none, one, more than two, or two but same-sign "hadron" (i.e., non-muon) tracks downstream were rejected outright and were excluded from any further considerations. The rest of the selection criteria either involved a characteristic or desirable property for a genuine candidate, or simply imposed a restriction in the range of a variable, or both. In the case of two of the properties, namely the energy balance and the pair opening angle, the cuts were applied in two stages. During the first stage loose cuts were applied in order to allow us to study the nature of, and correct for, any contaminating backgrounds. There were 1608 events which, in addition to presenting the correct downstream picture, also survived the two loose cuts. These events constituted the dataset from which the figures involving data and presented in association with the rest of this chapter were derived. The 459 members of this dataset which survived both the second stage stricter cuts in these two properties and the rest of the cuts formed yet another dataset. The latter determined the data-related input to the programs which calculated the cross sections. The cuts which were applied are discussed below.

Pair Opening Angle

The identity of the members of the pair of oppositely charged "hadrons," also referred to as a neutral pair, could not be unambiguously determined. Assumptions about the nature of the particles had to be made and the consequences of each assumption had to be compared with the observations.

One of the measurable properties of each pair is its laboratory opening angle. If the oppositely charged hadrons are pions originating from ρ decay, most of the opening angles should fall in the 10 to 20 mrad range. This is simply a consequence of the decay kinematics and is illustrated in Figure 13 for pairs of combined laboratory energy equal to 100 GeV and with invariant mass in the region of the ρ mass. Any reasonable assumption about the shape of the decay angular distribution, or equivalently the mode of the sharing of energy between the two pions, leads to opening angles in the 10-20 mrad range. This is even more the case when the CCM momentum cutoff is also taken into consideration.

The prominent feature of histograms of the opening angle was indeed a broad (FWHM $\simeq$ 8 mrad) peak centered on 13.5 mrad. Approximately 30 percent of the neutral pairs had, however, very small opening angles clustered into a secondary peak centered on 0.5 mrad (FWHM $\simeq$ 0.4 mrad). The oppositely charged "hadrons" with opening angle in this secondary peak were interpreted as electrons and positrons

pair-produced by photons from muon bremsstrahlung. Since the root-mean-square angle between either member of such an $e^+ - e^-$ pair and the direction of a parent photon of energy E, is[34]

$$\left\langle \theta^2 \right\rangle^{1/2} \simeq \frac{m_e c^2}{E} \ln \left(\frac{E}{m_e c^2} \right)$$

where m_e is the mass of the electron, small opening angles are indeed expected to characterize pairs of this nature. (Our 0.5 mrad angular resolution dominates and is reflected in the measurement of these small angles which are of the order of 0.1 mrad for a 100 GeV parent photon.) In addition, this interpretation is consistent with the relative numbers of pairs in the two (opening angle) peaks observed in our two targets.[35] Production of rhos is proportional to the target density while $e^+ - e^-$ pair production is inversely proportional to the target radiation length. Therefore, the fraction of $e^+ - e^-$ neutral pairs in hydrogen is expected and found to be twice as large as in deuterium. (Seventy percent of the hydrogen neutral pairs had opening angles $<$ 5 mrad.)

These considerations only argue in favor of the assumption that most of the pairs with small opening angles consist of electrons and positrons. The nature of the members of such pairs was established experimentally (confirming this assumption) by examining the distribution of the photon chambers spark counts associated with the track

of these particles and then comparing them to the distributions corresponding to other particles. The photon chambers, located directly downstream of a 3 radiation length steel plate, should detect showers in the case of electrons and positrons as opposed to registering just a few (of the order of the number of the planes involved) sparks when traversed by muons and hadrons. The number of photon chamber sparks associated with each electron track for samples of elastic μ-e scatters was indeed invariably larger than 20 (40 on the average). A similar distribution was observed for the spark counts of each of the members of pairs characterized by opening angle less than 1 mrad. In contrast, the distributions for muons and for members of pairs with larger opening angles peaked around a spark count of 8, with a FWHM of 10, but also had a sizable tail in the > 20 sparks region. Since the tails of the electron and hadron distributions overlapped and because some members of pairs were not headed towards the aperture of the photon chambers, particle identification on the basis of spark counts was not possible for individual events. We could, however, safely conclude that electron-positron pairs were responsible for the secondary peak in the opening angle histograms. The first stage cut was therefore applied at 1 mrad.

Diffractive production of ϕ mesons, followed by their decay into a K^+ - K^- pair, has the same topological

features as (IV.1). We could not distinguish pions from kaons but we could exclude this source of contamination by a tighter opening angle cut. This is so because the center of mass momentum of either kaon from a ϕ decay is 0.13 GeV/c while that of pions from a ρ decay is 0.36 GeV/c. Therefore, typical opening angles from ϕ decays are a factor of three smaller than those from typical ρ decays. Indeed, interpreting the members of pairs as kaons (by setting $M = m_k$ in equation [IV.2]) produced a peak in the invariant mass at $m = m_\phi$ and the opening angle of essentially all pairs in this peak was less than 5 mrad. The second stage opening angle cut was therefore imposed at 5 mrad, eliminating all ϕ-decay candidates. This cut also guaranteed that the z-position of the interaction vertex was accurately determined independent of Q^2, since it insured the presence of two tracks intersecting each other (and the muon tracks) at angles large compared to the 0.6 mrad experimental resolution. Knowing the vertex allowed us in turn to perform a fiducial volume target cut without the need for a corresponding subtraction from target empty runs.

We will be analyzing distributions of the invariant mass m of pairs. This mass is related to the laboratory opening angle of the pair α, by

$$m^2 = M^2 \left(2 + \frac{P_1}{P_2} + \frac{P_2}{P_1}\right) + 4 P_1 P_2 \sin^2 \frac{\alpha}{2} \qquad \text{(IV.2)}$$

where M is the mass of either member of the pair and P_1, P_2 are the momenta in the laboratory. Thus, for a given M, large opening angles imply large invariant masses and vice versa. A cut removing pairs with opening angle less than a certain value is therefore roughly equivalent to a cut of pairs with mass below a corresponding limit.

The effect of the 5 mrad opening angle cut on the dataset that survived the loose cuts is illustrated in Figure 14. The pair mass was calculated assuming that all decay products are pions. Although the cut removed just a small fraction of the events, it eliminated most of the pairs with mass less than 0.4 GeV, forcing us to adopt this value as the lower limit of the range over which the mass distributions were analyzed. What is more unfortunate but not evident from the figure is that this cut preferentially removes longitudinally polarized rhos, which favor small opening angles. The remaining data are therefore less sensitive to variations of angular distribution and polarization parameters. Since the cut was unavoidable, it was imposed and, at the same time, it was incorporated in the acceptance calculation. Therefore the effect of the cut was properly accounted for.

Interaction Vertex

The Z-distribution of the interaction vertex for the 1608 events which survived the loose cuts is shown in Figure 15. The target peak stands out clearly and it becomes

even sharper when the 5 mrad opening angle cut is imposed. The secondary peak around the - 9.5 m mark is due to the material of the most downstream set of beam hodoscopes and beam MWPC. Even though 60 percent of our events have $Q^2 < 0.2$ $(GeV/c)^2$ the distribution is very similar to that obtained when the vertex was determined by the muon alone and Q^2 was required to be larger than 0.5 $(GeV/c)^2$. This is due to the presence of the additional two upstream tracks, which help determine the vertex more accurately than it is possible from the muon tracks alone, for comparable values of Q^2. As it was mentioned a simple cut could therefore be imposed. The limits used were -7.250 m $< Z$ (vertex) $<$ -5.125 m and their position is indicated in the figure. A correction for events originating from the target mylar cup and from the downstream flange of the target container will have to be applied, since our vertex resolution could not exclude them.

Energy Balance

In a truly diffractive process the energy of the incident muon is accounted for by the sum of the energies of all particles in the final state of (IV.1). The energy of the unobserved recoil can be deduced from the value of t and it is a small correction in any case. In practice, resolution and radiative effects as well as backgrounds from inelastic processes complicate the situation. In order

to avoid any bias due to these and to systematic effects all events for which the absolute value of the energy balance was less than 15 GeV were retained at the beginning. The energy balance distribution for this sample is shown in Figure 16.

For the purposes of this plot unobserved energy carriers, such as neutrals and photons, present in the final state correspond to energy missing from the downstream view. The tail on the positive side of the peak should therefore be higher than the negative side one, as observed. The peak is not centered on zero indicating a 1 percent relative calibration disagreement between 1E4 and the CCM. One can use the energy balance plots for μ-e elastic events to center the distribution either on a run-by-run basis or as a function of ν for the dataset as a whole. However, these methods either make unverifiable assumptions about the relative stability of the two magnets or assign the full discrepancy to one of them. It was therefore decided not to adjust the position of the peak but to apply instead a less restrictive cut than the ± 3 GeV used for hydrogen. As shown in the figure, the second stage energy balance cut was applied at ± 5 GeV.

Radiative processes shift events towards the tails of the peak. A cut in the energy balance will thus result in the loss of a fraction of elastic events. Following

Urban,[36] W. R. Francis extended the calculation of the radiative corrections to our case and found that they were small and slowly varying.[37] Throughout most of the region of interest they only necessitated an increase of the cross sections by 3 ± 2 percent, for the hydrogen energy balance cut. For a looser cut the correction is even smaller and none was therefore applied. A correction for background remaining under the peak is, however, still necessary. The reduction of this background was one of the reasons for which the cut described next was applied.

Recoil Momentum Transfer (t)

The t-distribution of a diffractive process is characterized by an exponential falloff. This distribution for the 1608 events which survived the loose cuts in energy balance and opening angle, is shown in Figure 17. Clearly there is no point in including events with $|t| \geq 1.0$ GeV^2 since there the signal has dropped down to the level of the background, which is approximately flat. Even if all backgrounds were to be removed by the rest of the cuts, still the number of remaining events would be statistically insignificant. This so-called diffraction cut was therefore used to remove all events with $|t| > 0.8$ GeV^2, as indicated in the figure.

In addition to being practical, such a cut enhances the signal of interest by suppressing its contamination by

other processes. Events in which the ρ is produced inelastically but is accompanied by one or more undetected low-energy pions (so that the energy balance is satisfied), constitute the most obvious source of background. Inclusive ρ^o production by real and virtual photons has been studied at lower energies. In the case of inelastic ρ^o photoproduction[38] the slopes of the t-distribution fall in the 3-4 $(\mathrm{GeV/c})^{-2}$ range. Similar slopes are observed for inclusive ρ^o production by hadrons, while elastic ρ^o photoproduction is characterized by much steeper ($\simeq 7\ [\mathrm{GeV/c}]^{-2}$) slopes. In virtual photoproduction[39] the inelastic background in the region of the elastic peak has been measured to be less than 10 percent, and to be Q^2-independent. In our case the energy balance cut is roughly equivalent to requiring that the quantity $z = E_\rho/\nu$ be larger than 0.95. The background in this very forward region is therefore expected to be dominated by inelastic diffraction. Wolf[40] has predicted a t-slope of 5.5 for inelastic diffractive rho photoproduction at 10 GeV. Moreover, the inelastic diffractive scattering of pions has been measured at Fermilab energies[41] and found to be characterized by slopes of the order of 4.5 to 5.0. To the extent that these considerations are applicable to our case they predict a steeper t-slope for events passing the energy balance cut compared to the slope for those failing it and therefore that the t-cut would be more effective in removing events outside the energy balance cut.

These expectations were verified by our observations: The t-slopes from number of events distributions were of the order of 7 inside compared to 2.5 outside the energy balance cut. In addition, the t-cut removed some 20 percent of the events passing all but the energy balance cut, while removing only 6 percent of those passing all other cuts. We concluded that only a small fraction of the events passing all cuts involved rhos which were produced inelastically. This fraction was estimated to be of the order of 7 percent by considerations which are outlined below.

Since only a small fraction of unrelated upstream tracks accidentally passes within 7.5 mm of the corresponding vertex ordinate (at the z-position of the vertex) it is possible to identify events which are clearly inelastic, using only tertiary tape information, even though the downstream topology of all candidates is identical. For each event all upstream tracks that do not link downstream are examined for association with the vertex. If one or more such tracks point (within 7.5 mm) to the vertex the event is most likely inelastic and is so branded. We observed that the t-distribution of the thus defined inelastic events peaks at $t \neq 0$, with the peak shifting towards $t = 0$ as E_ρ/ν approaches unity. This verifies the inelastic nature of these events and justifies the method of their selection. (Note, however, that inelastic events involving neutrals cannot always be picked up in this way.)

The loose (± 15 GeV) energy balance cut allowed us to investigate the region of $z > 0.85$. Events passing all other cuts were grouped in several z-bins and the fraction of "inelastics" in each bin was determined. This fraction was found to decrease from 0.6 ± 0.1 for $z < 0.90$ to 0.06 ± 0.02 in the region inside the energy balance cut. Studies of our deuterium dataset for inclusive rho production[42] have shown that the ratio of the rho signal to the phase space background increases with increasing z, becoming approximately equal to one in the region $0.7 < z < 0.9$. This corresponds to a fraction of inelastics of 0.5 if we attribute the rho signal in the region of $z < 0.9$ solely to inelastic rhos. This comparison shows that a fraction of 0.6 is reasonable. As z increases less energy is available to the secondaries and so the fraction is expected to decrease. Since the fraction of inelastics observed inside the energy balance cut can be completely accounted for by accidentals, no reliable lower limit of the remaining background can be derived in this way.

The number of inelastic rhos remaining under the energy balance peak, i.e., having $z > 0.95$, was estimated using a triple-Regge analysis. It was also assumed that the topology cut did not remove any of the inelastic rhos with $z > 0.85$ from our sample. The effective triple-Pomeron coupling was parameterized as

$$G_{PPP}(t) = \beta \exp (B\ t)$$

Fits to the results of Hidaka[43] yielded

$$\beta = 0.9 \text{ mb/GeV}^2 \text{ and } B = 4 \text{ (GeV/c)}^{-2}$$

The relative numbers of inelastic rho events in our z bins were then predicted from the relation[44]

$$\frac{d\sigma}{dz} = \frac{\pi\beta}{B} \exp (B\, t_{max}) \frac{1}{1 - z}$$

where $t_{max} \simeq (1 - z)\ (m_\rho^2 + Q^2)$.

Neglecting acceptance variations with z (a 10 percent effect), it was calculated that the number of background rhos produced by inelastic diffraction and having $z > 0.95$ is approximately three times the corresponding number with $0.90 < z < 0.95$ and five times the 13 inelastic events with $0.85 < z < 0.90$ passing all other cuts. The result of lower energy inclusive ρ^0 photoproduction[38] that only half of the inclusive cross section is diffractive (conserves s-channel helicity) was then assumed for our case. The resulting background estimate was (7 ± 2) percent, depending on how the relative amounts of diffractive-inelastic and phase-space rhos were allowed to vary with z. (For $0.85 < z < 0.90$ they were taken as equal but the inelastics should predominate as z approaches z_{max}).

For hydrogen this background was estimated by extrapolation under the energy balance peak and was found to be (3 ± 2) percent. Extrapolation in deuterium again

resulted in a background estimate of about 8 percent. A purely theoretical estimate of this background can be derived from the work of Pirogov and Ter-Isaakyan.[45] The predicted maximum intercept at $t = 0$ of the inclusive rho production cross section (for $z > 0.95$) is approximately 5 $\mu b/GeV^2$, for $Q^2 = 0.05$ $(GeV/c)^2$ and a proton target. This cross section is of the order of 10 percent of our corresponding $\gamma^* p \rightarrow \rho p$ (i.e., elastic) cross section and in better agreement with the background correction used for deuterium.

Invariant Mass (m)

The opening angle cut eliminates most pairs with invariant mass less than 0.4 GeV. In addition, all rho mass peak signs disappear for m larger than 1.1 GeV. Therefore, in the analysis of the mass distributions only pairs for which $0.4 < m < 1.1$ GeV were considered. In the case of elastic rho photoproduction the tails of the mass distribution were found to be dominated by events due to diagrams other than the one resulting in a Breit-Wigner resonance. For this reason, in the case of the analysis of the t-distributions a more restrictive cut, namely $0.6 < m < 1.0$ was applied. This difference in the allowed invariant mass range for the two distributions studied was incorporated in the acceptance calculations.

Kinematic Range

This study was restricted to $Q^2 < 5.0$ $(GeV/c)^2$ for lack of events above this limit. Moreover only for $\nu > 80$ GeV were there events throughout this Q^2 range because low-Q^2, low-ν events were vetoed along with the unscattered beam by the N-veto counter.

The following construction was used to determine (for demonstration purposes) the fraction of scattered muons with given Q^2 and ν that would escape the N-veto. The momentum vector of a muon scattered by an angle θ lies with equal probability everywhere on the surface of a cone of half-angle θ and having the direction of the incident muon as its axis. We assume that the cone angle is preserved following passage through the CCM, but that the cone axis is bent by the magnetic field by an amount that is inversely proportional to the momentum of the scattered muon. A given set of $\{\nu, Q^2\}$ values then determines a unique ellipse on a plane at distance Z_h from the CCM center and parallel to the planes of the various downstream hdodscopes. This ellipse, which we approximate as a circle, is the intersection of the cone emerging from the CCM with the plane. The scattered muon corresponding to this set is equally likely to land on any point of the periphery of this circle at $Z = Z_h$. For a muon incident with momentum P_1 and emerging with momentum $P_2 \simeq P_1 - \nu$ after the scattering, the center of this circle

is situated at

$$X_c = - P_t * Z_h / P_2 \simeq - 2.22 * Z_h / P_2$$

where P_t is the transverse momentum kick of the CCM. The radius of the circle is given by

$$R_c = \Delta Z * (Q^2 - Q^2_{min})/(P_1 * P_2)^{1/2}$$

where ΔZ is the distance between the point of interaction and the plane at $Z = Z_h$. Therefore, for a fixed ν (and P_2) the radius increases like the square root of Q^2 and for a fixed Q^2 the radius increases with increasing ν.

The situation at the plane of the N-veto counter is illustrated in Figure 18, for which P_1 = 147.6 GeV and ΔZ = 21 m. A muon landing inside any of the three rectangles bounded by dashed lines will be vetoed. The large rectangle in the middle corresponds to the position of the scintillators of the N-veto counters. Its two satellite rectangles show the location of the thick portion of the lightguides of the same counter, which were found to also act as vetoes of indeterminate efficiency, and were, therefore, considered (by the software) as parts of the N-veto. It can be seen that for ν = 80 unless Q^2 is larger than approximately 3 the acceptance, i.e., the fraction of the circumference of a circle outside the rectangles, is close or equal to zero. (The size and the position of the N-veto were chosen to prevent the more numerous low-Q^2, low-ν events from saturating

the trigger.) For a fixed Q^2 (0.5 in the figure) as ν increases the acceptance also increases, until the circle starts intersecting the most negative x boundaries of the M hodoscope or until the momentum of the scattered muon becomes smaller than the CCM cutoff.

Factors such as the variable position of the interaction vertex, multiple scattering, and the beam phase-space combine in real life to smear the circles into annuli. These effects were incorporated in the Monte Carlo acceptance calculation and were found to constitute corrections of the order of 10 percent in the range $90 < \nu < 135$. Outside this range the corrections become larger due to the rapid decrease of the acceptance. In view of the uncertainties in the corrections we limited our study to this region of ν.

Muon Heading Toward N-Veto

For the purpose of the acceptance calculations the thick parts of the lightguides of the N-veto counters had to be considered as an integral part of the veto. Therefore the events in which the scattered muon was heading into this software veto had to be removed from the final sample. The reason some events of this kind were recorded is that the lightguides were not 100 percent effective as hardware vetoes. Moreover their effectiveness seemed to vary along their height making a simple average correction impossible.

CHAPTER V

DATA ANALYSIS

The final data set consisted of 459 events. These were grouped into eight bins to show the variation of the production cross section with Q^2 and ν. The distribution of the events and the boundaries of the bins are shown in Figure 19 together with Q^2_{min}, the minimum Q^2 allowed by kinematics for incident muons of momentum 150 GeV/c. The number of events and the averages of several kinematic quantities for each bin are listed in Table 3. Table 4 gives the distribution of the invariant mass, m of the $\pi^+ - \pi^-$ pair in each of the bins. The contents of Table 4 are shown plotted in Figure 20 after summing over ν. The strong Q^2 dependence of the ρ^o signal is already evident in the raw data. Table 5 gives the distribution of the events as a function of t, the square of the four-momentum transfer to the recoiling particle.

Raw Cross Sections Evaluation

We obtain average differential cross sections $\langle \frac{d\sigma}{dm} \rangle$ for each $[Q^2, \nu]$ bin by relating them to the number of elastic ρ^o events in the bin observed within a mass interval Δm

$$\Delta N_\rho = N_B N_T \left\langle \frac{d\sigma}{dm} \right\rangle \epsilon \, A \, \Delta m \qquad (V.1)$$

where N_B is the number of incident virtual photons within the corresponding $\Delta Q^2 \cdot \Delta\nu$ bin,

N_T is the number of scattering centers per unit area of the target,

ϵ is the product of all efficiency factors, and

A is the geometrical acceptance of the apparatus, a function of Q^2, ν, m, and t.

In equation (V.1) $\left\langle \frac{d\sigma}{dm} \right\rangle$ is the average differential cross section in the bin of width Δm, centered on m', defined by

$$\left\langle \frac{d\sigma}{dm} \right\rangle = \frac{1}{\Delta m} \int_{m' - \frac{\Delta m}{2}}^{m' + \frac{\Delta m}{2}} \frac{d\sigma}{dm} \, dm$$

The cross sections $\frac{d\sigma}{dt}$ are obtained by interchanging m and t.

In evaluating the cross section we have taken into account: (a) the variation of the cross section over the finite extent of the bins; (b) the effect on the acceptance of the angular dependence of ρ^o production, which arises from the spin structure of the $\gamma \to \rho^o$ transition; and (c) the variation of the virtual photon flux with Q^2 and ν. Thus, we write[46]

$$\frac{d\sigma[\mu N \to \mu N(\rho \to 2\pi)]}{dQ^2 d\nu dm}$$

$$= \Gamma_T(Q^2,\nu)W(\phi_\mu,\cos\theta,\phi)\ \frac{d\phi_\mu}{2\pi}\ \frac{d\cos\theta d\phi}{4\pi}\ \frac{d\sigma[\gamma^* N \to N(\rho \to 2\pi)]}{dm} \qquad (V.2)$$

where, as shown in Figure 21, ϕ_μ is the angle of intersection of the muon scattering plane with the rho production plane, θ and ϕ are the polar the azimuthal angles of the π^+ in the rest frame of the rho, and $W(\phi_\mu, \cos\theta, \phi)$ is the function describing the angular distribution, with normalization

$$\int W(\phi_\mu, \cos\theta, \phi)\ \frac{d\phi_\mu}{2\pi}\ \frac{d\cos\theta d\phi}{4\pi} = 1$$

These corrections are summarized by the factor I/J, the incorporation of which turns equation (V.1) into

$$N_\rho = N_\mu N_T \left\langle \frac{d\sigma}{dm} \right\rangle \epsilon \cdot (I/J) \qquad (V.3)$$

where N_ρ is one of the entries of Table 4, N_μ is the number of incident muons, and I is a multiple integral normalized by J and given by

$$I = \int_{\Delta m}\int_{t}\int_{Q^2}\int_{\nu}\int_{\phi_\mu}\int_{\cos\theta}\int_{\phi}\left[\frac{\Gamma_T(Q^2,\nu)}{2\pi} * A(Q^2,\nu,m,t,\phi_\mu,\cos,\phi)\right.$$

$$\left. * \frac{W(\phi_\mu,\cos\theta,\phi)}{4\pi} * G(Q^2,\nu,m,t)\right] dQ^2 d\nu dm dt d\phi_\mu d\cos\theta d\phi \qquad (V.4)$$

The integrations are over the full range of values covered in the bin. The function G describes the variation of the cross section within the integration volume. This is normalized by writing

$$J = (\Delta Q^2 \Delta\nu \Delta m \Delta t)^{-1} \int_{\Delta m}\int_{t}\int_{Q^2}\int_{\nu} G(Q^2,\nu,m,t) dQ^2 d\nu dm dt$$

The acceptance function A is the probability of detection of the scattered muon and both pions from the rho decay for the particular set of values of its arguments. As such it incorporates all apparatus efficiency corrections which depend on one or more of the integration variables. For more details and for the functional form of W used the reader is referred to the third section of this chapter.

The multiple integral of (V.4) was calculated by the Monte Carlo method of estimation because of the large number of variables. Details of the calculation are also given in the third section of this chapter. Here it suffices to say that the form for the function G for use in the final calculations could be reduced to that of the

square of the rho propagator, namely,

$$G = G(Q^2) = [m_\rho^2/(m_\rho^2 + Q^2)]^2 \qquad (V.5)$$

where m_ρ is the mass of the rho. As a result, the normalizing integral J assumed only one of four possible values. (One for each Q^2 range.) These four values are listed in Table 6, along with their corresponding Q^2 range.

The values of $\langle \frac{d\sigma}{dm} \rangle$ obtained from (V.3) correspond to data which have not been corrected for the smearing effects of the experimental resolution. These values are therefore referred to as the raw or smeared cross sections. The unfolding of the smearing from resolution effects was done by methods designed to match the particular parameterization chosen for the description of each distribution studied. These methods are discussed in the fourth section of this chapter. Here we give a description of the evaluation of each of the terms in (V.3).

Effective Luminosity

The effective luminosity L is defined as

$$L = N_\mu \, N_T \, \epsilon$$

The total number of incident muons, counted by a scaler which was gated by the experimental lifetime, for the runs included in this study was

$$N_\mu = 2.628 \times 10^{10} \text{ muons}$$

If we are to consider each nucleon as a scattering center, N_T is given by the product of the target length, the target density, and Avogadro's number. For our liquid deuterium target,

$$N_T = 1.168 \times 10^{25} \text{ nucleons/cm}^2$$

The efficiency ϵ is the product of the following seven independent corrections. Several of these have been determined in the muon-inclusive studies of the dataset.[25, 26]

Beam Reconstruction Efficiency, ϵ_1

As mentioned in the description of trackfinding in the beam region (Chapter III) the requirement of a clean incident muon track removed about 32 percent of the events from any further consideration. A correction of about 25 percent was made for the events lost only because of inefficiencies of the beam system. No correction was made for the difference which was attributed to truly "bad beam" resulting in spurious triggers.

For the measurement of this correction the elastic μ - e scatters were used as a monitor. These occurred with the same experimental conditions as the event triggers and were identifiable without reference to the incident beam. They were recorded throughout each run and were characterized by an opening angle (6 mrad) large enough for the accurate determination of the location of the vertex with respect

to the target. The inefficiency of the beam system is then the fraction of those triggers, identified as μ - e events originating in the target, for which the beam region track-finding programs failed to produce a clean incident muon tract. With this definition the average over all the runs was $\epsilon_1 = 0.756 \pm 0.010$.

Upstream Reconstruction
Efficiency, ϵ_2

Some 7 percent of otherwise perfectly good scattered muon candidates, detected in the downstream portion of the apparatus, linked to no upstream track, either in X or in Y. Such a link was required for momentum to be assigned, without which a track was bypassed as due to a halo muon. Since we have three particles in the final state and since each one of them is required to satisfy the same linking criteria the factor employed was $\epsilon_2 = 0.80 \pm 0.04$.

Pion Absorption
Correction, ϵ_3

Following the rho decay, each of the pions could be lost (i.e., not seen downstream) due to interactions in the intervening material. Absorption by the target material itself is substantial ($\simeq$ 12 percent per pion) but is incorporated in the Monte Carlo acceptance calculation. The probability of absorption of either pion by the material downstream of the target and upstream of the momentum measuring planes is estimated to be $\epsilon_3 = 0.980 \pm 0.005$.

Downstream Planes
Efficiency, ϵ_4

The value obtained from trackfinding studies and used for the muon inclusive analysis, namely $\epsilon_4 = 0.996 \pm 0.005$ was also adopted for this work. It is basically the result of a two-out-of-four requirement, with each of the four being more than 92 percent efficient.

Random Vetoeing
Correction, ϵ_5

Events may be lost when an improper veto is caused by accidental coincidence. This is the case when an N-counter is set by a real beam muon accompanying the interacting muon within the coincidence time gate. Muons arrived in r.f. buckets 2 nsec wide, separated by 18 nsec. Thus, the correction is the probability that two muons arrived in the same r.f. bucket. Estimates of this probability are provided by monitoring and comparing ratios of the form $T \cdot (S_{delayed})/T$, where T stands for some measure of the incident muon beam, S denotes the same or a different measure, and the subscript indicates a delay of the signal, typically 54 nsec. By taking into consideration the spatial distribution of the beam, the correction arrived at was $\epsilon = 0.994 \pm 0.030$.

Target Vessel
Subtraction, ϵ_6

The number of incident muons for the target-empty runs was approximately 12 percent of that corresponding to the target full ones. Moreover, the material of the target vessel that could produce a contamination in our final sample of events constituted only 2 percent of the mass of the deuterium target. As a result, the number of candidates for (IV.1) from the target-empty runs was statistically insignificant, making a simple subtraction impossible.

When all nuclear scatters are considered the ratio of target-empty to target-full in our region of interest is typically 0.08 with no apparent trend with Q^2 or ν. Since we are dealing with a subtraction the correction factor should be larger than 1.00. Based on these considerations the correction factor $\epsilon_6 = 1.05 \pm 0.03$ was applied.

Inelastic Background
Subtraction, ϵ_7

The final data sample of events, obtained following the application of all the cuts, is somewhat contaminated by inelastically produced rhos, accompanied by other undetected slow particles. As discussed in Chapter IV the t-cut reduces but does not eliminate this background and therefore a correction of 7 ± 2 percent had to be applied. Comparable estimates resulted from fitting the background outside the energy balance cut and extrapolating the fit

inside the cut. From these considerations we obtained $\epsilon_7 = 1.07 \pm 0.02$.

The overall efficiency is then $\epsilon = 0.659 \pm 0.046$ where the error includes a systematic error possibly as large as 7 percent. The resulting effective luminosity for this experiment is

$$L = (2.024 \pm 0.142) \times 10^{35} \text{ (muons x nucleons/cm}^2\text{)}$$

Monte Carlo
Acceptance Calculation

The multiple integral I is the only element of (V.3) that has not yet been given. As its definition by equation (V.4) shows, it is intimately related to the acceptance of our apparatus for the reaction of (IV.1). The quantitative nature of this relationship can be derived by comparing equations (V.1) and (V.3). This will be discussed later.

To estimate the integral of a function f(v) by Monte Carlo integration we select N different values of the variable v, uniformly over the interval of integration $\Delta v = b - a$, with $a < v < b$. The estimate for the integral

$$K = \int_a^b f(v)\, dv$$

is given by

$$K_{est.} = \Delta v * \left(\sum_{j=1}^{N} f(v_j) \right) / N$$

In the case of a multiple integral the index j refers to a set of values of the several variables of integration. Let Z_j denote the value of the integrand (the expression on square brackets) in (V.4) corresponding to a suitably chosen set j of values of the seven variables of integration. By forming a large number N of such sets the estimate for the multiple integral of interest is therefore given by

$$I = \prod_{k=1}^{7} \Delta v_k \; * \left[\left(\sum_{j=1}^{N} Z_j \right) / N \right] \equiv \prod_{k=1}^{7} \Delta v_k * S \tag{V.6}$$

This is the expression used for the evaluation of I, which appears in (V.3).

Within each Q^2 bin the values of all variables, except for t, were selected uniformly from their allowed range. The values of t were picked so as to simulate the exp (7t) distribution roughly characterizing the data (and our hydrogen results) thus improving the computational efficiency of the Monte Carlo calculation. As long as the apparatus acceptance does not vary significantly over the range of a variable, a judiciously chosen sampling method produces the same results while expediting the computations substantially for a desired level of accuracy. It was indeed found that for a given Q^2 bin the t-acceptance was flat within the calculation error estimates. This was also the case for the mass acceptance.

The preliminary cross sections calculated for the two ν regions of each Q^2 bin were found to be equal within errors, as was the case with our hydrogen results, and consistent with the slow (proportional to $a + b/\sqrt{\nu}$) energy variation expected from a diffractive process. Accordingly, an overage over ν, was taken giving half as many results with better statistics.

For the angular distribution function W we used the form predicted by Schilling and Wolf[47] under the assumptions of s-channel helicity conservation and natural parity exchange. It involves two amplitudes of relative phase angle δ. The trends of the variation of the parameters R_ρ and δ, determined by lower energy experiments[17] were extrapolated to the region of our measurements and were incorporated in the calculations. Specifically R_ρ was set to the lesser of Q^2 and 0.3 while $\cos\delta$ was set equal to 1.0. Our hydrogen results were also found to be consistent with such a behavior. This expression for W in (V.4) then becomes

$$W(\phi_\mu,\cos\theta,\phi) \equiv W(\cos\theta,\Psi) = 1.5*(1+\epsilon R_\rho)^{-1} * \{\sin^2\theta(1+\epsilon\cos 2\Psi) + 2\epsilon R_\rho\cos^2\theta - [2\epsilon(1+\epsilon)R_\rho]^{1/2}\sin 2\theta\cos\Psi\} \qquad (V.7)$$

where $\Psi = \phi - \phi_\mu$ (see Figure 21).

The direction and energy of the incident muon were selected so as to simulate the beam phase space used in the muon-inclusive analysis. The interaction vertex was chosen

uniformly along the target. Having checked that the scattering was kinematically allowed, the scattered muon was then propagated through the CCM and into the planes of the M and N hodoscopes. All corrections employed in the inclusive analysis, such as self-vetoing, were taken into consideration in determining the probability of a trigger by the scattered muon. Rho production and subsequent decay were then simulated and the probability of detection of each of the decay pions was determined. This included corrections for absorption in the target and for the effect of the desensitized region of the downstream chambers. Finally, a check was made whether the trial event satisfied the opening angle cut of 5 mrad, which was imposed on the data. The acceptance for each trial event consisted of the product of these individual "acceptances" and correction factors.

The product of the acceptance with the rest of the factors inside the square brackets in (V.4) for a trial event j has been designated as Z_j. Track was kept of the sum of these Z_j for each of the $\{Q^2 - \nu - m\}$ and $\{Q^2 - \nu - t\}$ bins of Tables 4 and 5 as well as of the number of trial events, whether they resulted in a $Z_j = 0$ or not, falling inside each of these three-dimensional volumes. Thus the values of the quantity $(\Sigma Z_j)/N$ corresponding to these or any coarser bins were known. The results for each of the four Q^2 regions, averaged over ν, are given in Table 7 for

the mass bins and in Table 8 for the t bins. The corresponding values of the product of the widths are listed in Table 6. Since the width of the t bins was variable, the entries in the last row of Table 6 have to be multiplied by the t-bin width, as indicated, in order to evaluate I using (V.6). In addition, for the t distributions Δm was taken as 0.7719, which is the fraction of the rho Breit-Wigner contained in the $0.6 < m < 1.0$ GeV mass range. This is all that is needed for the evaluation of the raw cross sections ($\Delta t = 1.0$ for $\frac{d\sigma}{dm}$).

The absolute value of the acceptance was obtained by combining equations (V.1) and (V.3) and using the relationship between the number of virtual photons (N_B) and that of muons (N_μ). In $\{Q^2 - \nu\}$ regions not affected by the Q^2_{min} cutoff the relation is

$$N_B = N_\mu * \left(\int \int \Gamma_T(Q^2,\nu)\, dQ^2 d\nu \right) \equiv N_\mu * \langle \Gamma_T \rangle \Delta Q^2 \Delta\nu$$

and can be used to derive lower limits (due to the opening angle cut in the Monte Carlo) of the acceptance. The result is then

$$A = \frac{8\pi^2 S}{J \langle \Gamma_T \rangle}$$

which gives acceptances in the 0.25 to 0.50 range, increasing with Q^2.

Distributions Studied

By solving equation (V.3) for $\langle \frac{d\sigma}{dm} \rangle$ or $\langle \frac{d\sigma}{dt} \rangle$ we obtain values of the smeared differential cross sections. These are given in Tables 9 and 10. The entries of the former are the cross sections per nucleon while those of the latter have been multiplied by 2 so as to give $\frac{d\sigma}{dt}$ per deuteron. The contents of Table 9 are also shown graphically in Figure 22, in which the ρ resonance signal is still evident.

Experimental Resolution

To extract the unmeasured cross sections the effects of our experimental resolution have to be taken into account. Since events were binned finely in m and t it is necessary to know how accurately each of these variables can be measured throughout the range of observations. The expressions

$$m^2 = m_\pi^2 \left(2 + \frac{P_+}{P_-} + \frac{P_-}{P_+}\right) + 4\, P_+ P_- \sin^2\left(\frac{\alpha}{2}\right)$$

and $t = -\nu^2\, \theta_{\gamma\rho}^2$

involve both laboratory momenta and angles. The studies of the μ - e elastic scatterings showed that the measurement error for a momentum p in GeV/c is given by

$$\frac{\Delta p}{p} = 0.035 * p\% \text{ (FWHM)}$$

The same studies have also determined that we can measure angles upstream with

$$\Delta\theta = 1.41 \text{ mrad (FWHM)}$$

which at $Q^2 = 2\, m_e\, \nu \simeq 0.11$ is equivalent to

$$\frac{\Delta Q^2}{Q^2} = 0.471 \text{ (FWHM)}$$

Since the energy lost by the muon is shared by two pions, the overwhelming majority of events have P_+ and P_- less than 100 GeV/c, and therefore measured to within better than 1.5 percent. Similarly, $\nu = E - E'$ is determined even more accurately since $E' < 60$ GeV always and E is measured to within a fraction of a percent. On the contrary, for most of the events $\Delta\theta$ constitutes a substantial fraction of the characteristic pair opening angles (α = 14 mrad for a symmetric 100 GeV pair) and of $\theta_{\gamma\rho}$. We therefore expect the uncertainty of the upstream angle measurements to dominate the error of determining m and t. For symmetric pairs in the region of the ρ mass peak the momentum uncertainties result in a Δm which is less than 1/3 of the Δm due to angle uncertainties. As a consequence, in calculating the smearing corrections the contribution from the momentum uncertainties was neglected.

The variation of $\frac{\Delta m}{m}$ as a function of m is shown in Figure 23. The results were obtained from a separate

Monte Carlo program, which calculated the resolution smearing corrections for the mass distributions.

The error in the measurement of t, assuming dominance of the angular errors and neglecting the momentum uncertainties, is given by,

$$\Delta t = 2\,\nu^2\,\theta\,\Delta\,\theta = 2\nu\,\sqrt{t}\,\Delta\,\theta$$

which for $\Delta\theta = 0.6 \times 10^{-3}$ and $\nu = 100$ GeV leads to

$$\Delta t = 0.12\,\sqrt{t} \simeq \frac{\sqrt{t}}{8}$$

and therefore,

$$\frac{\Delta t}{t} \simeq \frac{1}{8\sqrt{t}}$$

Mass Distributions

The possibility that nonresonant pion pairs might be included in our events was anticipated by Soding,[48] who was the first to point out that a $\pi^+ - \pi^-$ pair could be produced, without first forming a ρ meson, by the diffractive scattering of pions according to the diagrams of Figure 24. The amplitudes for these so-called "Drell-type" processes can interfere with the resonant amplitude and give rise to a shift in the position of the maximum and in the skewing of the peak. Soding made this suggestion in order to explain the shift in the value of the rho mass observed in rho photoproduction (compared to m_ρ from $e^+ - e^-$

annihilation). We have to take this effect into account in our analysis.

In Soding's original model this effect contributes almost the same amount to $\frac{d\sigma}{dm}$, independent of m. More recently, Bauer[49] improved the theoretical treatment of this effect by incorporating the possibility that both nonresonant pions scatter from the target. The resulting proper description requires that this nonresonant dipion background should vanish at $m = m_\rho$ and that it should then increase again. The shapes of the resonant, nonresonant background, and interference contributions to $\frac{d\sigma}{dm}$ are illustrated in Figure 25. The observed cross section is the sum of the three contributions and it is also shown.

Spital and Yennie[50] formulated Bauer's analysis in a way that can be easily compared to experimental results. The curves of Figure 25 correspond to a simplified form of their parameterization of $\frac{d\sigma}{dm}$. We parameterized our mass distributions using the same simplified form, namely,

$$\frac{d\sigma}{dm} = \frac{C_1 m m_\rho \Gamma}{(m_\rho^2 - m^2)^2 + m_\rho^2 \Gamma^2} \left[1 + C_2 \left(\frac{m_\rho^2 - m^2}{m^2} \right) + C_3 \left(\frac{m_\rho^2 - m^2}{m^2} \right)^2 \right] \tag{V.8}$$

where $\Gamma = \Gamma_\rho \frac{m_\rho}{m} \left(\frac{m^2 - 4m_\pi^2}{m_\rho^2 - 4m_\pi^2} \right)^{3/2}$.

In applying this formula we used $m_\rho = 0.77$ GeV and $\Gamma_\rho = 0.15$ GeV. Each set of coefficients $\{C_1, C_2, C_3\}$ corresponds to

a particular mixture of resonant, interference, and background contributions to $\frac{d\sigma}{dm}$.

A unique feature of this parameterization is that the total cross section for a given Q^2 bin has the value,

$$\sigma_\rho(Q^2) = \frac{\pi}{2}\,\Gamma_\rho \left.\frac{d\sigma}{dm}\right|_{m = m_\rho} = \frac{\pi}{2}\,\Gamma_\rho\,\frac{C_1}{\Gamma_\rho} = \frac{\pi}{2}\,C_1 \;\ldots \qquad (V.9)$$

in which only the coefficient of the Breit-Wigner term appears. Thus, we avoid uncertainties, inherent in different parameterizations, arising from the particular way of handling the large width of the rho.

The parameterization chosen here involves three functions of the mass,

$$\frac{d\sigma}{dm}(m) = C_1\,[F_1(m) + C_2F_2(m) + C_3F_3(m)].$$

Each measured value of the raw $\frac{d\sigma}{dm}$ tabulated in Table 9 corresponds to the integral of the right-hand side of the above equation over the appropriate mass bin, once the smearing has been taken into account. Estimates of the integral of each of the smeared F_i, i.e., $F_i(m) \rightarrow F_i(m \pm \delta m)$, were obtained for each mass bin j by Monte Carlo integration. These integrals are denoted by

$$K_i^j = \int_{\text{mass bin } j} F_i(m \pm \delta m)\,dm \qquad (i = 1, 2, 3)$$

with values listed in Table 11. The smeared cross sections could then be directly fitted to

$$\frac{d\sigma}{dm}\,(\text{smeared})\Big|_{\text{bin } j} = C_1(K_1^j + C_2K_2^j + C_3K_3^j). \qquad (V.10)$$

This method avoids integrations during fitting.

At the same time we obtained estimates of the integrals of the unsmeared functions F_i. These are denoted by

$$M_i^j = \int_{\text{mass bin } j} F_i(m)\, dm \qquad (i = 1, 2, 3)$$

with values listed in Table 12. For each mass bin j we can write

$$\frac{d\sigma}{dm}\,(\text{unsmeared})\Big|_{\text{bin } j} = r_j * \frac{d\sigma}{dm}\,(\text{smeared})\Big|_{\text{bin } j}$$

where the resolution correction factor r_j is determined by the corresponding pair of coefficients $\{C_2, C_3\}$, obtained from the fit, given by

$$r_j = (M_1^j + C_2M_2^j + C_3M_3^j)/(K_1^j + C_2K_2^j + C_3K_3^j) \qquad (V.11)$$

The main effect of the resolution was to broaden and to lower the rho mass peak by shifting events to its sides. For the best fits the magnitude of this correction never exceeded 10 percent.

t -Distributions

The t dependence of diffractive rho production by real and virtual photons incident on protons is, as expected, a simple exponential in t. In the case of deuterium target, when the recoiling particle is not detected, the situation is more complicated. Allowance has to be made for the possibility of coherent production by the deuterium nucleus, for the screening of one nucleon by the other, and for Fermi motion. Indeed, the most prominent feature of the raw t distributions was an excess of events in the region of small t, where the coherent contribution is expected to be relatively strongest.

The formalism for the scattering of high energy particles incident on deuterons has been developed by Franco and Glauber.[51] The predictions of the Glauber theory for photoproduction of rho mesons in deuterium give a good account of the observations[52, 53] and suggest the parameterization

$$\frac{d\sigma}{dt}(\gamma^* d \to d\rho^o \text{ or } pn\rho^o) = 4|T_o|^2\left[\frac{1}{2}(1 + S(t))e^{Bt} - Ge^{3Bt/4}\right] \tag{V.12}$$

where S(t) is the deuteron form factor, G stands for the Glauber shadowing correction at t = 0, and where the amplitudes for rho production off bare protons and bare neutrons were assumed to be equal and given by

$$f_p = f_n = T_o \exp(Bt/2).$$

In this notation, the contribution of the coherent component is given by[52]

$$\frac{d\sigma}{dt}(\gamma^* d \to \rho^o d) = 4|T_o|^2 \left[S^2(\tfrac{t}{4})e^{Bt} - S(\tfrac{t}{4})\, Ge^{3Bt/4}\right] \quad . \qquad (V.13)$$

In order to simplify the calculations we used the Hulthen wavefunction for the deuteron obtaining,

$$S(t) = \left(\frac{1}{2\alpha} + \frac{1}{2\beta} - \frac{2}{\alpha + \beta}\right)^{-1}$$

$$\times \frac{1}{u}\left[\tan^{-1}\left(\frac{u}{2\alpha}\right) + \tan^{-1}\left(\frac{u}{2\beta}\right) - 2\tan^{-1}\left(\frac{u}{\alpha + \beta}\right)\right]$$

where $t = u^2$. Following Fridman,[54] the wavefunction parameters α and β were set to 0.0456 and 0.260 GeV/c, respectively. The value used for the shadowing correction was

$$G = \frac{\sigma_{tot}(\rho N)}{4\pi} \left\langle \frac{1}{r^2} \right\rangle_{n-p} \simeq 0.068$$

Using a Monte Carlo calculation in a manner similar to that of the mass distributions, estimates of the smeared (i.e., $t \to t \pm \delta t$) and unsmeared integrals of the fitting function given by (V.12) were obtained for each of the 12 t-bins. Since the fitting function involves the unknown slope parameter B, these estimates were obtained for

several values of B in the range $3 < B < 11$ $(GeV/c)^{-2}$. It was found that the resolution correction varied linearly and rather slowly with B, i.e., that

$$r_j \text{ (t bins)} = C_j + D_j * B$$

The values of C_j and D_j corresponding to each of the t-bins are listed in Table 13. The unsmeared value of the cross section for each t-bin can be obtained by multiplying the raw cross section by the r_j corresponding to the value of the slope B.

CHAPTER VI

RESULTS

The results given below were obtained by bin maximum likelihood fits to the integral of the function parameterizing the differential cross sections. It was assumed that events populated the various bins according to the Poisson distribution. To each set of the parameters of the fit there corresponds a calculable probability for observing the number of events contained in each bin. The product of the probabilities over all (m or t) bins across each Q^2 range was maximized separately by adjusting the variables of the fit. The software employed for this purpose relied on the MINUIT package.

Mass Cross Sections

In the case of the mass distributions the output of the fitting program gave one set of coefficients $\{C_1, C_2, C_3\}$ for each of the four Q^2 regions. These sets are presented in Table 14 together with the maximum likelihood chisquared,

$$\chi^2 = \sum_{\text{bins}} (N_{\text{observed}} - N_{\text{expected}})^2 / N_{\text{expected}} \quad ,$$

corresponding to each of the best fits.

The values of the resolution correction factors r_j of (V.11) corresponding to the best fits are listed in Table 15. It can be seen that none of them exceeds 10% as it was already mentioned.

Figures 26 through 29 show the unsmeared fitting functions corresponding to the best fits together with the cross sections, corrected for resolution. The data points are the bin-centered values of the measured cross sections. This makes a direct visual comparison fair. The quality of the fit is good.

The presence of a nonresonant dipion background, with its resulting complications, is supported by the data. Except for our highest Q^2 range, the fits to a pure Breit-Wigner term are poor. The amount of this background is found to decrease with increasing Q^2. In Figure 25 we show approximately the relative strengths of the three terms for the region $0.1 < Q^2 < 0.3$ $(\mathrm{GeV}/c)^2$. Quantitative estimates of this background are obtained by comparing the integral of the fit to the integral of the Breit-Wigner term alone over the same mass range. For $Q^2 < 0.1$ $(\mathrm{GeV}/c)^2$ and $0.4 < m_{\pi\pi} < 1.1$ GeV the contamination, defined as the relative difference of the two integrals, amounts to 18.7 percent. The restriction $0.6 < m_{\pi\pi} < 1.0$ GeV reduces this contamination to 7.5 percent in the same Q^2 range and results in proportionately similar reductions in the other

three Q^2 ranges. This provides justification, based on our own data, for the decision to impose the $0.6 < m_{\pi\pi} < 1.0$ GeV restriction in the analysis of the t-distributions.

The total cross section for the process for each Q^2 region, $\sigma_\rho(Q^2)$, was calculated from the corresponding C_1 according to equation (V.9). The results (cross sections per nucleon) are presented in Table 16 together with the corresponding average values of Q^2. As in the acceptance calculation, these averages were obtained assuming that the cross section has the Q^2 variation of the square of the rho propagator. Such a relationship implies that a plot of $\sigma_\rho(Q^2)$ against $(m_\rho^2/(Q^2 + m_\rho^2))^2$ should yield a straight line through the origin, with a slope equal to $\sigma_\rho(Q^2 = 0)$, which is the rho photoproduction cross section at our energy. Our results are plotted in this way in Figure 30 and are found to be consistent with such a relationship. The value of the slope resulting from the fit is

$$\sigma_\rho(Q^2 = 0) = 8.7 \pm 0.4 \ \mu\text{barns}.$$

Thus, our data predicts the value of the total cross section of the reaction $\gamma p \rightarrow \rho^0 p$, for incident real photons at 112 GeV. This result is in agreement with that obtained from our hydrogen data.

The mass distributions were also analyzed using the Soding parameterization, i.e., assuming a constant background

term. The extraction of $\sigma_\rho(Q^2)$ is less clear cut in this case but the fits also resulted in a Q^2 variation of C_1 consistent with that of the square of the rho propagator.

We compare directly results of different experiments, performed at different energies, by considering the ratio $\sigma_\rho(Q^2)/\sigma_\rho(0)$. Figure 31 shows the Q^2 variation of this ratio for our results and for data from a lower energy experiment.[15] The square of the rho propagator gives a good fit to both datasets.

Vector meson dominance models[9, 10] predict that the Q^2 dependence of this ratio is given by the product of the square of the rho propagator with the factor $(1 + \epsilon R_\rho)$. (See pages 5 and 6 for the definitions of ϵ and R_ρ, respectively.) At comparable Q^2 the average value of ϵ for the Cornell experiment is twice as large as ours and, for fixed Q^2, R_ρ decreases with increasing energy. (See page 14 for the Q^2 and energy variation of R_ρ.) Therefore the comparison presented in Figure 31 would seem to contradict the predictions of Vector Dominance. The complete theoretical prediction for this ratio must, however, incorporate corrections for kinematic effects such as the variation, at fixed energy, of the virtual photon flux with Q^2 and the cutoff due to the minimum allowable t, $t_{min} = ((m_\rho^2 + Q^2)/2\nu)^2$. Such corrections, while negligible at our energy, provide a compensating effect to the $(1 + \epsilon R_\rho)$ factor at

lower energies, bringing the Cornell and other energy data (as long as $W > 2$ GeV) in agreement with the VDM prediction.[13] At our energy, on the other hand, both ϵ and R_ρ are small. The average value of ϵ for our highest Q^2 bin is 0.44 and our hydrogen results for R_ρ, which are best described by $R_\rho = 0.17\ Q^2/m_\rho^2$, yield $R_\rho = 0.7$ at $Q^2 = 2.4$ GeV^2/c^2. (The measurement is $R_\rho = 0.5$, with large errors.) Therefore, the curve predicted by VDM is higher than that of Figure 31 by about 30 percent in the vicinity of our highest Q^2 point (7 percent for the second highest). Since our highest Q^2 cross section is only measured to 25 percent and since there are large uncertainties in the R_ρ parameterization, such a shift would still be consistent with our results. A more accurate measurement is needed to decide the issue. Until then equation (I.5) should be used as the best account of the Q^2 variation of our measurements.

There exist many measurements of the rho photoproduction cross section at lower energies. By comparing these measurements to the extrapolation of our results to $Q^2 = 0$ we extend the study of the energy variation of the cross section for the process $\gamma p \rightarrow \rho^o p$ by a factor of five in incident photon energy. Figure 32 presents a comparison of our extrapolated results to those from two other experiments[55, 56] performed at lower energies. The curve in the same figure corresponds to the right hand side of

equation (I.4) and is calculated using the value of the rho-photon coupling constant obtained by colliding beam experiments. The good agreement between the data and the curve justifies combining the basic tenets of Vector Meson Dominance and quark structure of hadrons (from which the curve resulted) to relate the rho photoproduction cross section to that of elastic pion-proton scattering. (At higher energies the latter is more likely to be measured first and it can then be used to predict the former.) In addition, the slow energy variation of the rho photoproduction cross section is a strong indication that the process is diffractive.

t Cross Sections

The $\frac{d\sigma}{dt}$ cross sections were derived from the analysis of dipions with invariant mass m restricted to $0.6 < m < 1.0$ GeV to minimize the effects of the nonresonant background. The appropriate correction for the loss of the portion of the Breit-Wigner resonance outside this mass range was applied. The results were fitted to the functional form of equation (V.12). Since the resolution smearing correction depends on one of the parameters of the fit, the slope B, the unsmeared cross sections also vary with B. With few exceptions, the resolution corrections are less than 10 per cent. In Figures 33 through 36 we show the best fits and the $\frac{d\sigma}{dt}$ cross sections, corrected for resolution by the amount corresponding to the

value of B indicated in each figure. The agreement is good.

The output of the fits to the t-distributions consists of values for the quantities $4|T_o|^2$ and B appearing in (V.12). The former, when multiplied by 0.932 (= 1 - G), yields the t = 0 intercept, while B corresponds to the $\frac{d\sigma}{dt}$ slope for a proton target. The values of these two parameters resulting in the best fits are given for each of the four Q^2 regions in Table 17. They correspond to fits in the range $t_{min} < |t| < 0.4$ $(GeV/c)^2$ except for the highest Q^2 bin for which the upper limit could be increased to 0.6 $(GeV/c)^2$. (The background is smaller at higher Q^2). Contributions from the neglected D-wave admixture become important around t = 0.5 $(GeV/c)^2$ and therefore the parameterization used is not expected to be valid too far beyond this point.

A typical contour on which the logarithm of the product of the probabilities differs by 0.5 from its maximum can be traced by drawing a line joining the symbol "1" in Figure 37. The errors listed in Table 17 include the maximum excursion of this correlation ellipse.

The values of the slope parameter B obtained for each of the four Q^2 regions are presented graphically in Figure 38. The corresponding results from our hydrogen data are also shown. We conclude that the results are consistent with no change in B with Q^2. This result is in agreement with the observed flatness of $\langle p_T^2 \rangle$ of hadrons in our data,[57]

independent of Q^2. This increase of $\langle p_T^2 \rangle$ with Q^2 has been postulated by Cheng and Wu, in Reference 11, to predict a corresponding decrease of $B(Q^2)$.

A comparison of equations (V.12) and (V.13) shows that the relative amounts of coherent and incoherent contributions to the observed cross section are determined by the value of the slope B. For $B \simeq 7\ (\mathrm{GeV/c})^{-2}$ the coherent contribution amounts to 40 percent. At $t = 0$ the final state $\rho^o d$ dominates (over $pn\rho^o$) and, extrapolating out data to $Q^2 = 0$, we predict that at our energy the $t = 0$ intercept of the cross section for $\gamma d \rightarrow \rho^o d$ is $234.6 \pm 19.2\ \mu b/GeV^2$. This has to be compared to corresponding lower energy measurements of the same quantity[52, 53, 58] in the range 300 to 500 $\mu b/GeV^2$. Our prediction is consistent with the observed decrease of cross section with energy.

The Q^2 variation of the $t = 0$ intercepts, and consequently, for a fixed B, of the total cross section, is consistent with that of the square of the rho propagator. Also, within errors, the value of $|T_o|^2$ obtained from our hydrogen data agrees with the deuterium result, once our hydrogen t-results are normalized to yield the same cross sections for rho production as obtained from the analysis of the mass distributions in the same Q^2 range. (The hydrogen $\frac{d\sigma}{dt}$ refer to dipions with $0.6 < m < 1.0$ and not to rhos.)

Conclusions

In this paper we have shown how rho mesons appear in virtual photon processes by a diffractive mechanism. In particular we show that our measurements of the virtual photoproduction of rhos exhibit the following characteristics.

The measured Q^2 variation of the total cross section is described well by that of the square of the rho propagator and is consistent with VDM predictions.

The estimate for the photoproduction cross section at our energy, obtained by extrapolation to $Q^2 = 0$, agrees with the expectation that it should be proportional to the elastic pion-proton cross section, scaled by a factor prescribed by Vector Dominance. Such a slow variation with energy is indicative of the diffractive nature of the process.

There is no evidence for flattening of the diffraction peak with increasing Q^2, although the experiment lacks the sensitivity necessary for a definitive determination of the issue. Coherent rho production by virtual photons has been seen for the first time. It is manifested as an enhancement of the cross section in the forward ($|t| < 0.1$ GeV^2) region compared to the extrapolation from larger $|t|$ values and is described well by Glauber theory.

We have estimated that 40 percent of our events are due to coherent scatters. Although their presence is only evident in the low $|t|$ region, they have Q^2 values throughout

the accepted range, as indicated by the persistence of the enhancement in all Q^2 bins. The observed Q^2 dependence of the cross section is the same as that in the case of single nucleon (i.e., proton) targets. This constitutes evidence in favor of the conclusion that both coherent and incoherent rho production are characterized by the same Q^2 variation. Observations of the production from a higher A nucleus, where most of the events will be coherent, are needed in order to answer this question definitely.

We find that the Q^2 variation of the cross section can be described without any reference to t and, conversely, that the t variation does not depend on Q^2. Thus the cross section may be factorized into a product of functions each only involving one of these two variables. Thus, for a given energy s, the cross section can be written as

$$\sigma_\rho(s, Q^2, t) = \sigma_\rho(s, 0, 0) * f(Q^2) * g(t)$$

where f and g are the functions determined by our analysis.

REFERENCES

1. M. L. Good and W. D. Walker, Phys. Rev. 120, 1857 (1960) and references therein.
2. L. N. Hand, Phys. Rev. 129, 1834 (1963).
3. D. Benaksas et al., Phys. Lett. 39B, 289 (1972).
4. R. P. Feynman, Photon-Hadron Interactions, W. A. Benjamin, Inc., Reading, Massachusetts (1972), p.90.
5. L. Stodolsky, Phys. Rev. Lett. 18, 135 (1967).
6. H. Joos, Phys. Lett. 24B, 103 (1967).
7. J. J. Sakurai, Phys. Rev. Lett. 22, 981 (1969).
8. D. Schildknecht, Springer Tracts in Modern Physics, 63, Springer-Verlag, Berlin, 1973, p. 57.
9. C. F. Cho and G. J. Gounaris, Phys. Rev. 186, 1619 (1969).
10. H. Fraas and D. Schildknecht, Nucl. Phys. B 14, 543 (1969).
11. H. Cheng and T. T. Wu, Phys. Rev. 183, 1324 (1969); R. W. Griffith, Phys. Rev. 188, 2112 (1969); H. T. Nieh, Phys. Lett. 38B, 100 (1972); J. B. Kogut, Phys. Rev. D 5, 1152 (1972).
12. H. Fraas, B. J. Read, and D. Schildknecht, Nucl. Phys. B 88, 301 (1975).
13. G. Wolf, in Proceedings of the 1975 International Symposium on Lepton and Photon Interactions at High Energies, edited by W. T. Kirk (Stanford Linear

Accelerator Center, Stanford, Calif., 1975), p. 795.

14. J. T. Dakin et al., Phys. Rev. D 8, 687 (1973).

15. L. Ahrens et al., Phys. Rev. D 9, 1894 (1974).

16. J. Ballam et al., Phys. Rev. D 10, 765 (1974).

17. P. Joos et al., Nucl. Phys. B 113, 53 (1976).

18. R. F. Mozley, in Proceedings of the 1975 International Symposium on Lepton and Photon Interactions at High Energies, edited by W. T. Kirk (Stanford Linear Accelerator Center, Stanford, Calif., 1975), p. 783.

19. C. Driver et al., Nucl. Phys. B 38, 1 (1972).

20. K. B. Burns et al., Nucl. Instr. and Meth. 106, 171 (1973).

21. R. H. Heisterberg, Thesis, University of Chicago (1976), unpublished.

22. H. L. Anderson et al., Rev. Sci. Instr. 23, 707 (1952).

23. T. A. Nunamaker, Rev. Sci. Instr. 42, 1701 (1971).

24. T. A. Nunamaker and D. B. Turner, Nucl. Instr. and Meth. 113, 445 (1973).

25. S. H. Pordes, Thesis, Harvard University (1976), unpublished.

26. G. I. Kirkbride, Thesis, Oxford University (1976), unpublished.

27. The parameterization used for $\nu W_2(\omega)$ is given in G. Miller et al., Phys. Rev. D 5, 528 (1972).

28. T. Kirk, T. Quirk, and S. C. Wright, On-Line Sub-Routines III, E98 Internal Report (1973), unpublished.

29. H. S. Matis, Thesis, University of Chicago (1976), unpublished.

30. W. R. Francis, First Test of the O.H.I. Trackfinding Program, E98 Internal Report (unpublished), 7/8/75.

31. S. H. Pordes, Track-Finding Efficiency, E98 Internal Report (unpublished), 1/3/76.

32. Off-Line Analysis Notes, E98 Internal Document, 1974 (unpublished); E-98 Fermilab-Oxford Analysis, E98 Internal Document, 1975 (unpublished).

33. W. R. Francis et al., Phys. Rev. Lett. 38, 633 (1977).

34. Bruno Rossi, High-Energy Particles, Prentice-Hall Inc., New York (1952), p. 83.

35. I am indebted to Dr. W. R. Francis for pointing this out to me.

36. Paul Urban, Topics in Applied Quantumelectrodynamics, Springer-Verlag, Wien 1970, p. 168-227.

37. W. R. Francis, Radiative Corrections to $\mu p \rightarrow \mu p \pi^+ \pi^-$, E98 Internal Report (unpublished), June 1976.

38. E. Kogan et al., Nucl. Phys. B 122, 383 (1977).

39. C. del Papa et al., Phys. Rev. Lett. 40, 90 (1978).

40. G. Wolf, Nucl. Phys. B 26, 317 (1971).

41. D. S. Ayres et al., Phys. Rev. Lett. 37, 1724 (1976).

42. B. A. Gordon, Inclusive Rho Meson Production, E98 Internal Report (unpublished), June 1976.

43. K. Hidaka, Phys. Rev. D 16, 690 (1977).

44. K. Kajantie, in Proceedings of the 1973 CERN-JINR School of Physics, edited by O. Kofoed-Hansen (CERN, Geneva, 1973), p. 152.

45. Yu. F. Pirogov and N. L. Ter-Isaakyan, Sov. J. Nucl. Phys. 22, 279 (1976).

46. Equation 12 in B. Dieterle, Nuovo Cimento, 11A, 523 (1972).

47. K. Schilling and G. Wolf, Nucl. Phys. B 61, 381 (1973).

48. P. Soding, Phys. Lett. 19, 702 (1966).

49. T. Bauer, Phys. Rev. D 3, 2671 (1971).

50. R. Spital and D. R. Yennie, Phys. Rev. D 9, 126 (1974).

51. V. Franco and R. J. Glauber, Phys. Rev. 142, 1195 (1966).

52. Y. Eisenberg et al., Nucl. Phys. B 104, 61 (1976).

53. G. Alexander et al., Nucl. Phys. B 104, 397 (1976).

54. A. Fridman, Fortschr. Phys. 23, 243 (1975).

55. Aachen-Berlin-Bonn-Hamburg-Heidelberg-Munchen Collaboration, Phys. Rev. 175, 1669 (1968).

56. R. Anderson et al., Phys. Rev. D 1, 27 (1970).

57. W. A. Loomis et al., Phys. Rev., to be published.

58. R. L. Anderson et al., Phys. Rev. D 4, 3245 (1971).

TABLE 1

EXPERIMENTS ON RHO PRODUCTION BY VIRTUAL PHOTONS

Item	SLAC-SPCH[a]	Cornell[b]	SLAC-HBC[c]	DESY[d]	UCSC-SLAC[e]	FNAL E98 (CHIO)[f]
Beam Particles	e^-	e^-	μ^-	e^-	μ^+	μ^+
Beam Energy (GeV)	19.5	12	16	7.2	14	147
Target	4 cm LH_2	1.3 cm LH_2	1 m LH_2	9 cm LH_2	40 cm LH_2[g]	1.2 m LH_2, LD_2
Spectrometer Features	Wide Aperture, 17 KGm magnet	Two-arm, Small Solid Angle	Fast-cycling, hybrid bubble chamber	~ 4π, 18 KGm magnet, streamer chamber	~ 4π, 32 KGm magnet, streamer chamber	Large aperture, 74 KGm magnet
(Other) Track-Measuring Detectors	Optical Spark Chambers	Magnetostrictive Spark Chambers	Magnetostrictive Spark Chambers	Proportional Chambers	Spark Chambers	Proportional and Spark Chambers
Particles Detected in the Final State	e, π^+, π^-	e, p	μ, π^+, π^-, p	e, π^+, π^-, p	μ, π^+, π^-, p but not always	μ, π^+, π^-
Q^2 range (GeV^2/c^2)	0.25 - 2.0	0.4 - 2.2	.05 - 2.5	0.3 - 1.4	0.3 - 2.5	0.01 - 5.0
ν range (GeV)	5 - 16	2.7 - 8.6	1.7 - 13	0.6 - 5.1	2 - 12	90 - 135

[a]Ref. 14. [b]Ref. 15. [c]Ref. 16. [d]Ref. 17. [e]Ref. 18. [f]This experiment.

[g]Data were also taken with a LD_2 target but no results have been reported.

TABLE 2

HADRON ASSIGNMENT TO HALO BY TEST

Test Failed		Percentage[a]
(1)	Linking to muon chamber track	8.7
(2)	Y projection missing y of vertex	7.4
(3)	None of upstream linked tracks aiming towards vertex	6.2
(4)	1 and 2 above	3.9
(5)	1 and 3 above	1.9
(6)	2 and 3 above	5.0
(7)	1 and 2 and 3 above	3.2

[a]The remaining 63.7 percent of the tracks were associated with the triggering interaction.

TABLE 3

BIN KINEMATICS

Q^2 range (GeV^2/c^2)	$\langle Q^2 \rangle$ (GeV^2/c^2)	$\langle \nu \rangle$ (GeV)	$\langle \epsilon \rangle$	Events
.010 - 0.10	0.052	101.69	0.38	97
.025 - 0.10	0.067	119.20	0.15	77
0.10 - 0.30	0.181	103.70	0.49	64
0.10 - 0.30	0.171	122.16	0.24	99
0.30 - 1.00	0.510	102.41	0.53	42
0.30 - 1.00	0.514	121.40	0.29	50
1.00 - 5.00	1.812	100.62	0.55	17
1.00 - 5.00	1.875	123.53	0.29	13

TABLE 4

EVENT DISTRIBUTION INTO THE m BINS

	$0.0 < Q^2 < 0.1$		$0.1 < Q^2 < 0.3$		$0.3 < Q^2 < 1.0$		$1.0 < Q^2 < 5.0$	
m range (GeV)	$90<\nu<112.5$	$112.5<\nu<135$	$90<\nu<112.5$	$112.5<\nu<135$	$90<\nu<112.5$	$112.5<\nu<135$	$90<\nu<112.5$	$112.5<\nu<135$
0.4 - 0.5	5	5	2	4	4	1	0	0
0.5 - 0.6	10	8	5	10	3	3	1	1
0.6 - 0.7	19	15	9	18	6	7	4	4
0.7 - 0.8	32	32	28	34	21	19	4	5
0.8 - 0.9	23	9	12	26	7	13	4	1
0.9 - 1.0	8	7	6	4	0	7	3	2
1.0 - 1.1	0	1	2	3	1	0	1	0

TABLE 5

DISTRIBUTION OF THE EVENTS WITH 0.6 < m < 1.0 GeV INTO THE t BINS

-t range (GeV^2/c^2)	$0.0 < Q^2 < 0.1$		$0.1 < Q^2 < 0.3$		$0.3 < Q^2 < 1.0$		$1.0 < Q^2 < 5.0$	
	$90<\nu<112.5$	$112.5<\nu<135$	$90<\nu<112.5$	$112.5<\nu<135$	$90<\nu<112.5$	$112.5<\nu<135$	$90<\nu<112.5$	$112.5<\nu<135$
0.80 - 0.60	3	3	0	2	2	2	1	1
0.60 - 0.40	0	1	1	4	2	4	1	0
0.40 - 0.30	5	1	3	6	3	3	0	0
0.30 - 0.20	8	12	5	8	2	2	0	1
0.20 - 0.16	5	2	1	6	1	3	0	0
0.16 - 0.12	13	6	6	7	5	4	1	1
0.12 - 0.10	7	3	3	2	2	0	1	1
0.10 - 0.08	3	1	3	5	3	1	0	1
0.08 - 0.06	6	6	6	5	3	5	1	1
0.06 - 0.04	8	5	5	6	2	2	2	1
0.04 - 0.02	9	14	8	12	3	8	2	2
0.02 - 0.00	15	9	14	19	6	12	6	3

TABLE 6

ACCEPTANCE-RELATED QUANTITIES DEPENDING ONLY ON Q^2

	J^a	$\prod_{k=1}^{7} \Delta V_k$ (for $\frac{d\sigma}{dm}$)[b]	$\frac{1}{\Delta t} \prod_{k=1}^{7} \Delta V_k$ (for $\frac{d\sigma}{dt}$)[b, c]
Q^2 range (GeV^2/c^2)			
0.0 - 0.1	0.857	35.531	274.26
0.1 - 0.3	0.570	71.061	548.52
0.3 - 1.0	0.250	248.714	1919.82
1.0 - 5.0	0.040	1421.223	10970.42

[a]See page 81 for the definition of J and page 82 for its evaluation.

[b]See page 88 for the relation of this quantity to the acceptance.

[c]The t bin width is variable.

TABLE 7

VALUES OF THE ACCEPTANCE-RELATED QUANTITY S[a] AND OF ITS ESTIMATED ERROR[b] FOR THE m BINS

m range (GeV)	$0.0 < Q^2 < 0.1$	$0.1 < Q^2 < 0.3$
0.3 - 0.4	2.19E-08 +/- 6.90E-09	8.01E-09 +/- 2.16E-09
0.4 - 0.5	2.56E-07 +/- 2.07E-08	1.21E-07 +/- 8.19E-09
0.5 - 0.6	2.48E-07 +/- 2.02E-08	1.42E-07 +/- 7.77E-09
0.6 - 0.7	2.75E-07 +/- 2.28E-08	1.32E-07 +/- 7.57E-09
0.7 - 0.8	2.95E-07 +/- 2.20E-08	1.33E-07 +/- 7.48E-09
0.8 - 0.9	2.82E-07 +/- 2.09E-08	1.44E-07 +/- 9.11E-09
0.9 - 1.0	2.63E-07 +/- 2.13E-08	1.41E-07 +/- 8.63E-09
1.0 - 1.1	2.55E-07 +/- 2.00E-08	1.35E-07 +/- 7.58E-09
1.1 - 1.2	2.94E-07 +/- 2.17E-08	1.36E-07 +/- 7.90E-09
1.2 - 1.3	2.93E-07 +/- 2.21E-08	1.38E-07 +/- 8.47E-09

m range (GeV)	$0.3 < Q^2 < 1.0$	$1.0 < Q^2 < 5.0$
0.3 - 0.4	2.16E-09 +/- 5.67E-10	1.15E-10 +/- 4.24E-11
0.4 - 0.5	2.20E-08 +/- 1.51E-09	1.10E-09 +/- 1.02E-10
0.5 - 0.6	2.40E-08 +/- 1.61E-09	1.29E-09 +/- 1.23E-10
0.6 - 0.7	2.40E-08 +/- 1.78E-09	1.27E-09 +/- 1.11E-10
0.7 - 0.8	2.40E-08 +/- 1.51E-09	1.27E-09 +/- 1.12E-10
0.8 - 0.9	2.43E-08 +/- 1.69E-09	1.10E-09 +/- 9.44E-11
0.9 - 1.0	2.23E-08 +/- 1.60E-09	1.27E-09 +/- 1.10E-10
1.0 - 1.1	2.45E-08 +/- 1.56E-09	1.29E-09 +/- 1.04E-10
1.1 - 1.2	2.33E-08 +/- 1.47E-09	1.47E-09 +/- 1.30E-10
1.2 - 1.3	2.61E-08 +/- 1.64E-09	1.19E-09 +/- 1.08E-10

[a]The quantity S is defined by equation (V.6) in page 58.

[b]The error, being the Monte Carlo estimate, is purely statistical.

TABLE 8

VALUES OF THE ACCEPTANCE-RELATED QUANTITY S[a] AND OF ITS ESTIMATED ERROR[b] FOR THE t BINS

t range (GeV^2/c^2)	$0.0 < Q^2 < 0.1$	$0.1 < Q^2 < 0.3$
0.800 - 0.600	2.84E-07 +/- 9.33E-08	1.98E-07 +/- 5.71E-08
0.600 - 0.400	3.15E-07 +/- 4.95E-08	1.32E-07 +/- 1.65E-08
0.400 - 0.300	3.54E-07 +/- 4.92E-08	1.77E-07 +/- 2.07E-08
0.300 - 0.200	2.79E-07 +/- 3.17E-08	1.26E-07 +/- 1.20E-08
0.200 - 0.160	2.70E-07 +/- 3.59E-08	1.10E-07 +/- 1.26E-08
0.160 - 0.120	3.20E-07 +/- 3.94E-08	1.28E-07 +/- 1.22E-08
0.120 - 0.100	2.76E-07 +/- 4.31E-08	1.19E-07 +/- 1.39E-08
0.100 - 0.080	3.06E-07 +/- 4.34E-08	1.30E-07 +/- 1.42E-08
0.080 - 0.060	2.56E-07 +/- 3.50E-08	1.32E-07 +/- 1.25E-08
0.060 - 0.040	2.30E-07 +/- 3.08E-08	1.59E-07 +/- 1.38E-08
0.040 - 0.020	2.46E-07 +/- 3.00E-08	1.32E-07 +/- 1.06E-08
0.020 - 0.000	2.69E-07 +/- 2.80E-08	1.60E-07 +/- 1.35E-08

t range (GeV^2/c^2)	$0.3 < Q^2 < 1.0$	$1.0 < Q^2 < 5.0$
0.800 - 0.600	1.96E-08 +/- 5.90E-09	1.41E-09 +/- 4.45E-10
0.600 - 0.400	2.66E-08 +/- 3.78E-09	1.77E-09 +/- 2.94E-10
0.400 - 0.300	2.47E-08 +/- 3.37E-09	1.55E-09 +/- 2.69E-10
0.300 - 0.200	2.55E-08 +/- 2.22E-09	1.12E-09 +/- 1.31E-10
0.200 - 0.160	2.18E-08 +/- 2.53E-09	1.45E-09 +/- 2.06E-10
0.160 - 0.120	2.23E-08 +/- 2.59E-09	1.04E-09 +/- 1.58E-10
0.120 - 0.100	2.46E-08 +/- 3.16E-09	1.44E-09 +/- 2.28E-10
0.100 - 0.080	2.27E-08 +/- 3.11E-09	1.32E-09 +/- 2.50E-10
0.080 - 0.060	2.54E-08 +/- 3.42E-09	1.27E-09 +/- 1.78E-10
0.060 - 0.040	2.26E-08 +/- 2.56E-09	1.41E-09 +/- 1.86E-10
0.040 - 0.020	2.11E-08 +/- 1.98E-09	9.28E-10 +/- 1.08E-10
0.020 - 0.000	2.51E-08 +/- 2.59E-09	9.62E-10 +/- 1.30E-10

[a]The quantity S is defined by equation (V.6) in page 58.

[b]The error, being the Monte Carlo estimate, is purely statistical.

TABLE 9

RAW[a] m DIFFERENTIAL CROSS SECTIONS, PER NUCLEON, IN μBARNS/GeV

m range (GeV)	$0.0 < Q^2 < 0.1$	$0.1 < Q^2 < 0.3$	$0.3 < Q^2 < 1.0$	$1.0 < Q^2 < 5.0$
0.4 - 0.5	4.64 +/- 1.52[b]	1.95 +/- 0.81	1.13 +/- 0.51	0.00 +/- 0.13[c]
0.5 - 0.6	8.66 +/- 2.16	4.19 +/- 1.11	1.24 +/- 0.51	0.21 +/- 0.15
0.6 - 0.7	14.69 +/- 2.80	8.07 +/- 1.62	2.69 +/- 0.77	0.87 +/- 0.32
0.7 - 0.8	25.82 +/- 3.76	18.44 +/- 2.56	8.25 +/- 1.40	0.98 +/- 0.34
0.8 - 0.9	13.51 +/- 2.59	10.46 +/- 1.82	4.09 +/- 0.96	0.63 +/- 0.29
0.9 - 1.0	6.79 +/- 1.84	2.81 +/- 0.91	1.56 +/- 0.60	0.55 +/- 0.25
1.0 - 1.1	0.47 +/- 0.47	1.46 +/- 0.66	0.20 +/- 0.20	0.11 +/- 0.11

[a]That is, not corrected for resolution.

[b]Errors statistical only.

[c]Error shown corresponds to $\frac{d\sigma}{dm}$ resulting if one event had been observed in the bin.

TABLE 10

RAW[a] t DIFFERENTIAL CROSS SECTIONS, PER DEUTERON, IN μBARNS/GeV^2

t range (GeV^2/c^2)	$.0 < Q^2 < .1$	$.1 < Q^2 < .3$	$.3 < Q^2 < 1.$	$1. < Q^2 < 5.$
0.800 - 0.600	3.26 +/- 1.71[b]	0.52 +/- 0.39	1.31 +/- 0.76	0.26 +/- 0.20
0.600 - 0.400	0.49 +/- 0.50	1.94 +/- 0.90	1.45 +/- 0.63	0.10 +/- 0.10
0.400 - 0.300	5.24 +/- 2.26	5.23 +/- 1.85	3.13 +/- 1.35	0.00 +/- 0.24[c]
0.300 - 0.200	22.17 +/- 5.56	10.55 +/- 3.09	2.02 +/- 1.03	0.32 +/- 0.32
0.200 - 0.160	19.98 +/- 8.00	16.31 +/- 6.44	5.90 +/- 3.03	0.00 +/- 0.63[c]
0.160 - 0.120	45.85 +/- 11.94	26.07 +/- 7.65	12.97 +/- 4.58	1.73 +/- 1.25
0.120 - 0.100	55.97 +/- 19.74	21.54 +/- 9.96	5.23 +/- 3.76	2.50 +/- 1.81
0.100 - 0.080	20.15 +/- 10.47	31.51 +/- 11.66	11.32 +/- 5.87	1.36 +/- 1.39
0.080 - 0.060	72.43 +/- 23.14	42.87 +/- 13.55	20.23 +/- 7.65	2.85 +/- 2.05
0.060 - 0.040	87.11 +/- 26.82	35.54 +/- 11.15	11.38 +/- 5.84	3.82 +/- 2.26
0.040 - 0.020	144.24 +/- 34.85	78.00 +/- 18.54	33.60 +/- 10.61	7.76 +/- 3.98
0.020 - 0.000	137.75 +/- 31.56	106.10 +/- 20.53	46.21 +/- 11.89	16.85 +/- 6.06

[a]That is, not corrected for resolution.

[b]Errors statistical only.

[c]Error shown corresponds to $\frac{d\sigma}{dt}$ resulting if one event had been observed in the bin.

TABLE 11

INTEGRALS OF THE SMEARED FUNCTIONS PARAMETERIZING THE MASS DIFFERENTIAL CROSS SECTIONS[a]

Mass range of integration (GeV)	j	(Breit-Wigner) K_1^j	(Interference) K_2^j	(Background) K_3^j
0.4 - 0.5	1	0.082	0.141	0.256
0.5 - 0.6	2	0.345	0.286	0.259
0.6 - 0.7	3	1.839	0.571	0.221
0.7 - 0.8	4	5.308	0.226	0.057
0.8 - 0.9	5	3.459	-0.497	0.094
0.9 - 1.0	6	1.468	-0.473	0.158
1.0 - 1.1	7	0.818	-0.370	0.169

[a]See page 96 for the definition of these integrals.

TABLE 12

INTEGRALS OF THE UNSMEARED FUNCTIONS PARAMETERIZING THE MASS DIFFERENTIAL CROSS SECTIONS[a]

Mass Range of integration (GeV)	j	(Breit-Wigner) M_1^j	(Interference) M_2^j	(Background) M_3^j
0.4 - 0.5	1	0.074	0.135	0.253
0.5 - 0.6	2	0.328	0.292	0.271
0.6 - 0.7	3	1.605	0.567	0.221
0.7 - 0.8	4	5.698	0.274	0.045
0.8 - 0.9	5	3.426	-0.550	0.099
0.9 - 1.0	6	1.400	-0.469	0.159
1.0 - 1.1	7	0.799	-0.366	0.168

[a]See page 97 for the definition of these integrals.

TABLE 13

COEFFICIENTS DETERMINING THE t RESOLUTION CORRECTION FACTOR[a]

-t range (GeV^2/c^2)	j	C_j	D_j
0.80 - 0.60	1	1.338	-0.086
0.60 - 0.40	2	1.178	-0.045
0.40 - 0.30	3	1.168	-0.035
0.30 - 0.20	4	1.095	-0.017
0.20 - 0.16	5	1.055	-0.008
0.16 - 0.12	6	1.064	-0.008
0.12 - 0.10	7	1.040	-0.002
0.10 - 0.08	8	1.128	-0.012
0.08 - 0.06	9	1.011	0.005
0.06 - 0.04	10	1.022	0.005
0.04 - 0.02	11	0.955	0.017
0.02 - 0.00	12	0.913	0.005

[a]Given by $r_j = C_j + D_j * B$.

TABLE 14

RESULTS OF THE FITS TO THE MASS DIFFERENTIAL CROSS SECTIONS[a]

Item	$0.0 < Q^2 < 0.1$	$0.1 < Q^2 < 0.3$	$0.3 < Q^2 < 1.0$	$1.0 < Q^2 < 5.0$
C_1 (μbarns)	4.63 ± 0.34[b]	3.24 ± 0.24	1.34 ± 0.14	0.24 ± 0.06
C_2	1.91 ± 0.36	1.44 ± 0.33	1.45 ± 0.45	0.69 ± 0.73
C_3	2.44 ± 0.70	1.24 ± 0.56	0.90 ± 0.69	0.69 ± 1.99
χ^2 (NDF = 3)	7.59	1.99	4.86	5.27

[a]The functional form of the fit is given by equation (V.8) in page 95.

[b]The errors are statistical only.

TABLE 15

MASS RESOLUTION CORRECTION FACTORS[a]

m range (GeV)	$0.0<Q^2<0.1$	$0.1<Q^2<0.3$	$0.3<Q^2<1.0$	$1.0<Q^2<5.0$
0.4 - 0.5	0.973	0.966	0.963	0.960
0.5 - 0.6	1.016	1.006	1.003	0.994
0.6 - 0.7	0.930	0.918	0.917	0.901
0.7 - 0.8	1.077	1.078	1.079	1.076
0.8 - 0.9	0.955	0.964	0.963	0.979
0.9 - 1.0	0.941	0.939	0.934	0.949
1.0 - 1.1	0.976	0.972	0.968	0.975

[a]Given by equation (V.11) in page 97.

TABLE 16

Q^2 VARIATION OF THE TOTAL CROSS SECTION

Q^2 range (GeV^2/c^2)	$\langle Q^2 \rangle$ (GeV^2/c^2)	$\left[\frac{m_\rho^2}{\langle Q^2 \rangle + m_\rho^2}\right]^2$	$\sigma(\langle Q^2 \rangle)$ per $D_2/2$ (μbarns)	$\sigma(\langle Q^2 \rangle)$ for H_2 [a] (μbarns)
0.0 - 0.1	0.05	0.854	7.28 ± 0.54[b]	6.79 ± 0.86[b]
0.1 - 0.3	0.19	0.565	5.09 ± 0.38	4.30 ± 0.57
0.3 - 1.0	0.60	0.244	2.11 ± 0.22	1.29 ± 0.31
1.0 - 5.0	2.40	0.039	0.38 ± 0.09	0.31 ± 0.11

[a]Private communication from W. R. Francis.

[b]The errors are statistical only.

TABLE 17

RESULTS OF THE FITS TO THE t DIFFERENTIAL CROSS SECTIONS

Item	$0.0 < Q^2 < 0.1$	$0.1 < Q^2 < 0.3$	$0.3 < Q^2 < 1.0$	$1.0 < Q^2 < 5.0$
$4\|T_o\|^2$ ($\mu b/(GeV/c)^2$)	224.4 ± 29.8	137.5 ± 17.8	57.9 ± 10.6	18.4 ± 5.1
$B((GeV/c)^{-2})$	7.1 ± 0.9	7.0 ± 1.0	7.5 ± 1.4	12.6 ± 2.4
χ^2/NDF	12.80/7	2.95/7	8.83/7	8.42/8

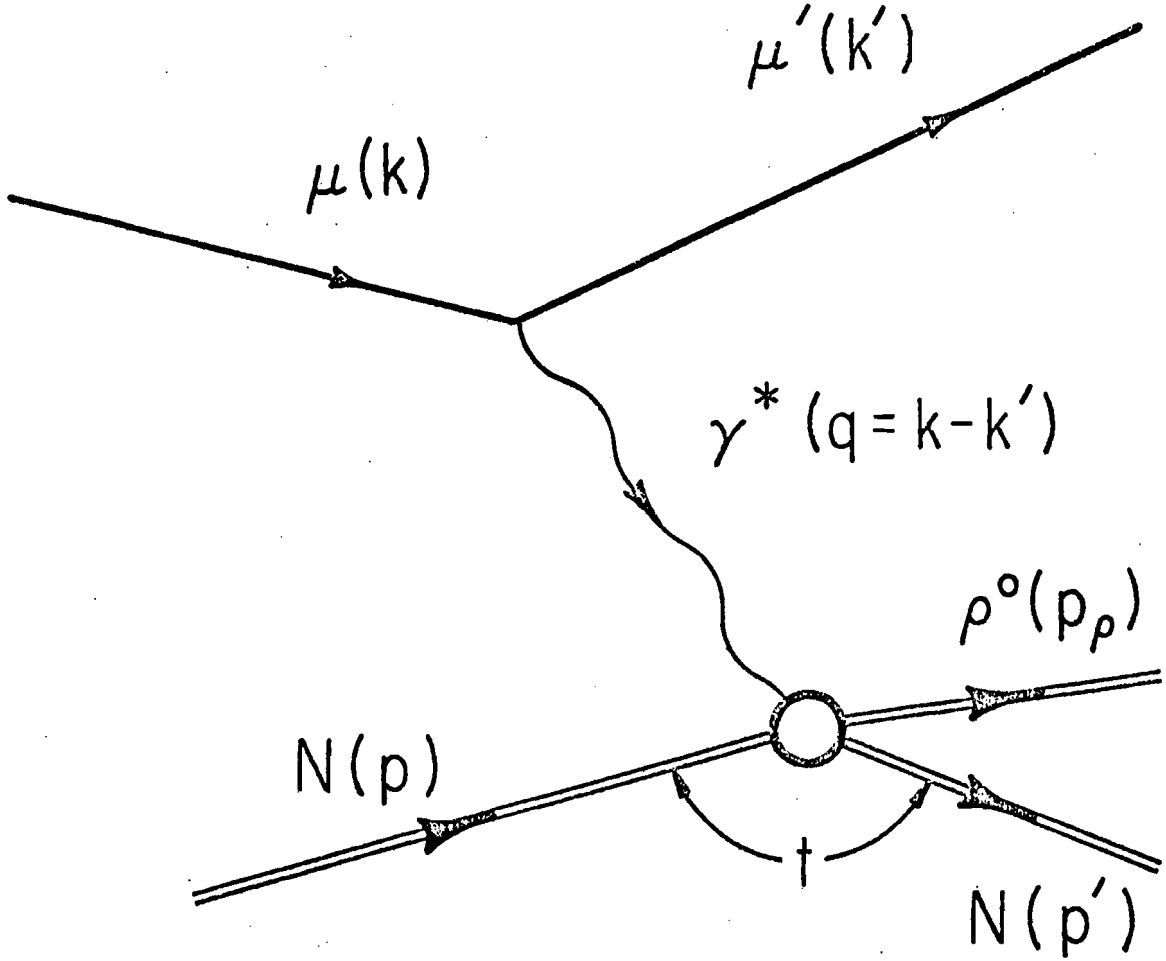

Figure 1.--Feynman diagram for diffractive rho muoproduction via single photon exchange.

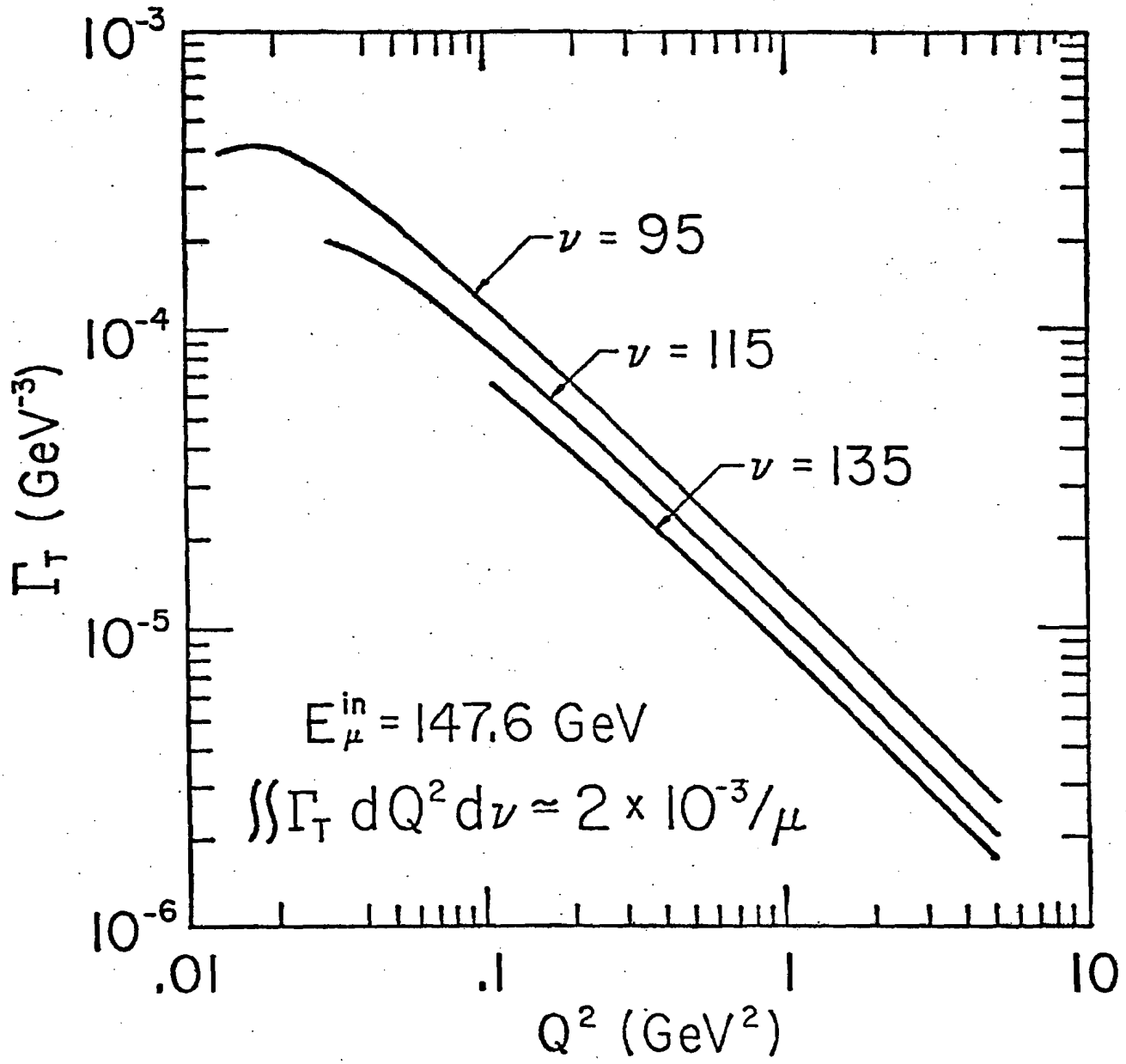

Figure 2.--Variation of the virtual photon flux factor with Q^2, for three values of ν.

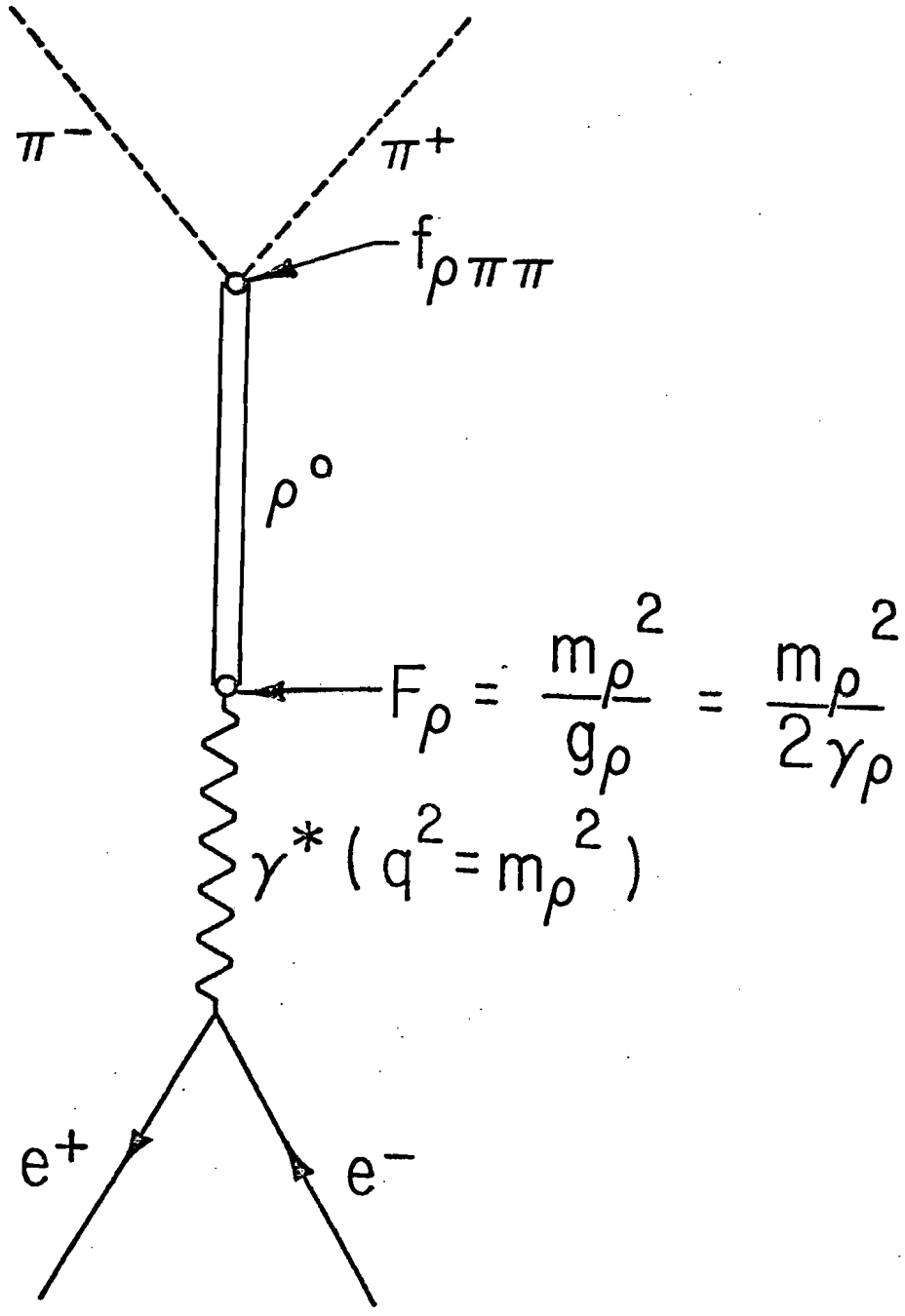

Figure 3.--Feynman diagram for rho production by timelike virtual photons from e^+ - e^- annihilation. The most common notations for the coupling constants involved are shown explicitly.

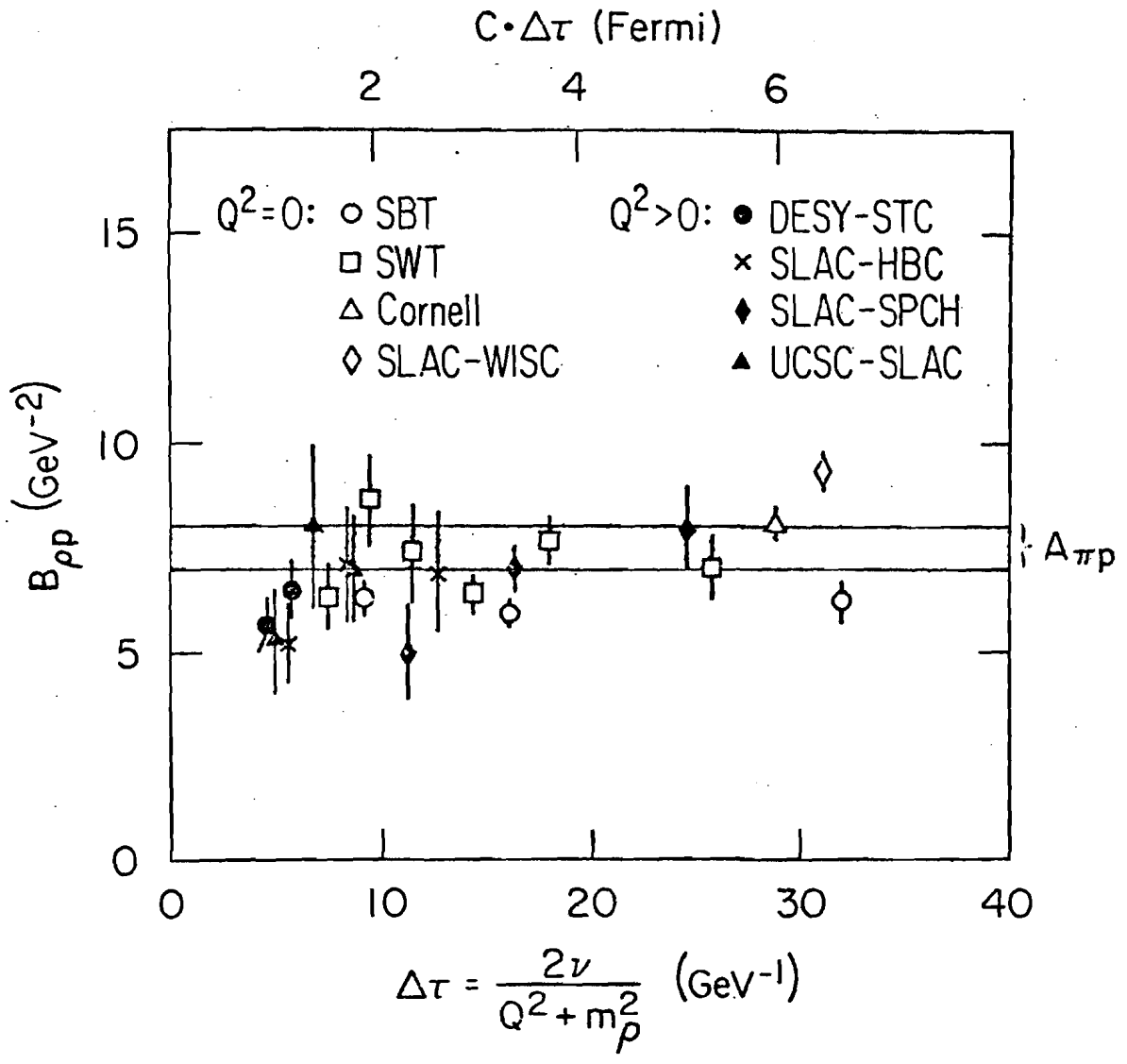

Figure 4.--Slope of the diffractive peak as a function of the $\gamma \to \rho$ transition time. The slope parameterizes the t differential cross section for the elastic production of rhos by real ($Q^2 = 0$) or virtual ($Q^2 > 0$) photons incident on protons. This figure comes from Reference 13, a review of experiments other than our own. Our measurements correspond to $\Delta\tau > 32$ GeV^{-1}, with a lowest average $\Delta\tau = 91$ GeV^{-1} (for our highest Q^2 range).

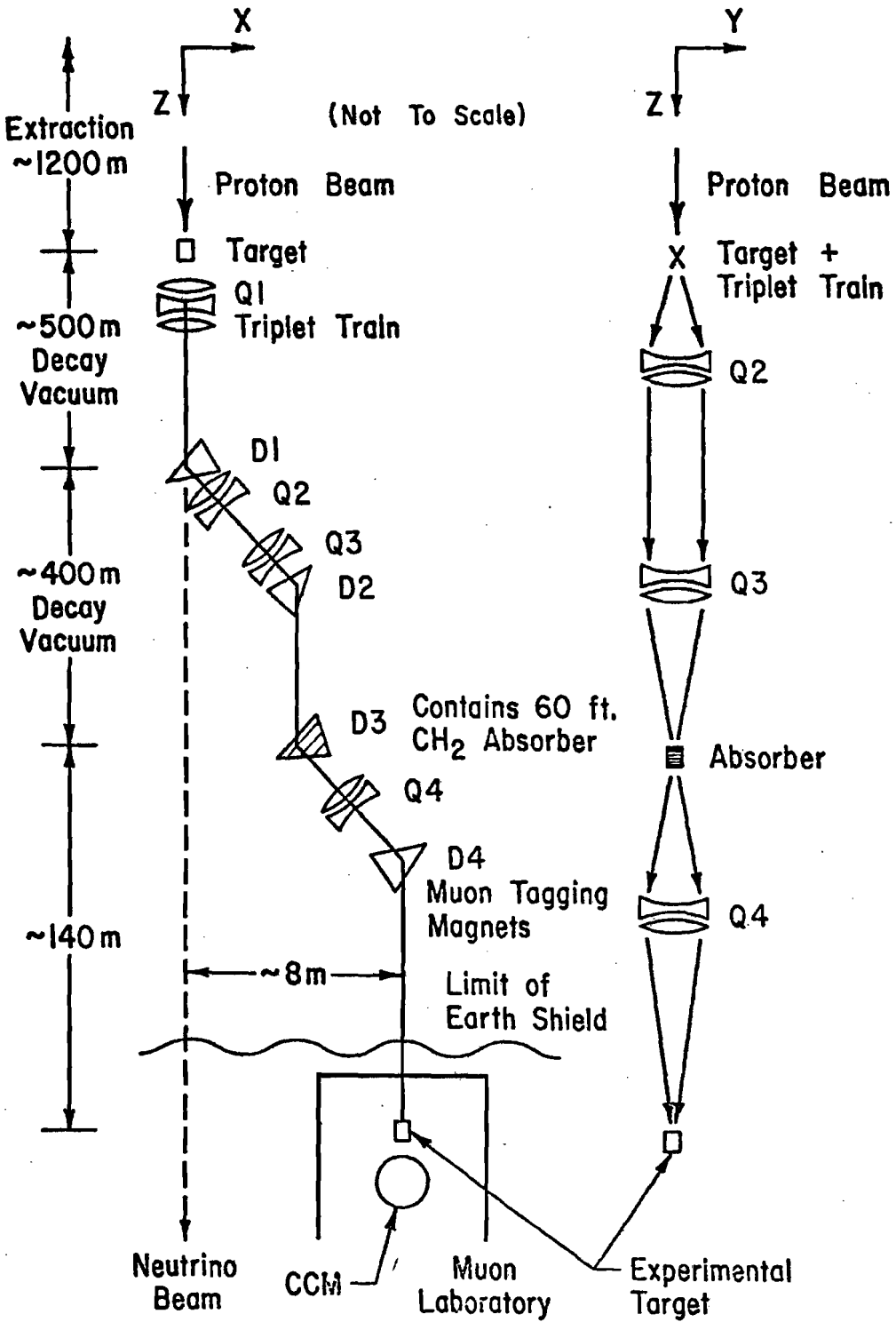

Figure 5.--Schematic and optics of the muon beam line. The letters Q and D are used to denote a quadrupole or a dipole magnet, respectively.

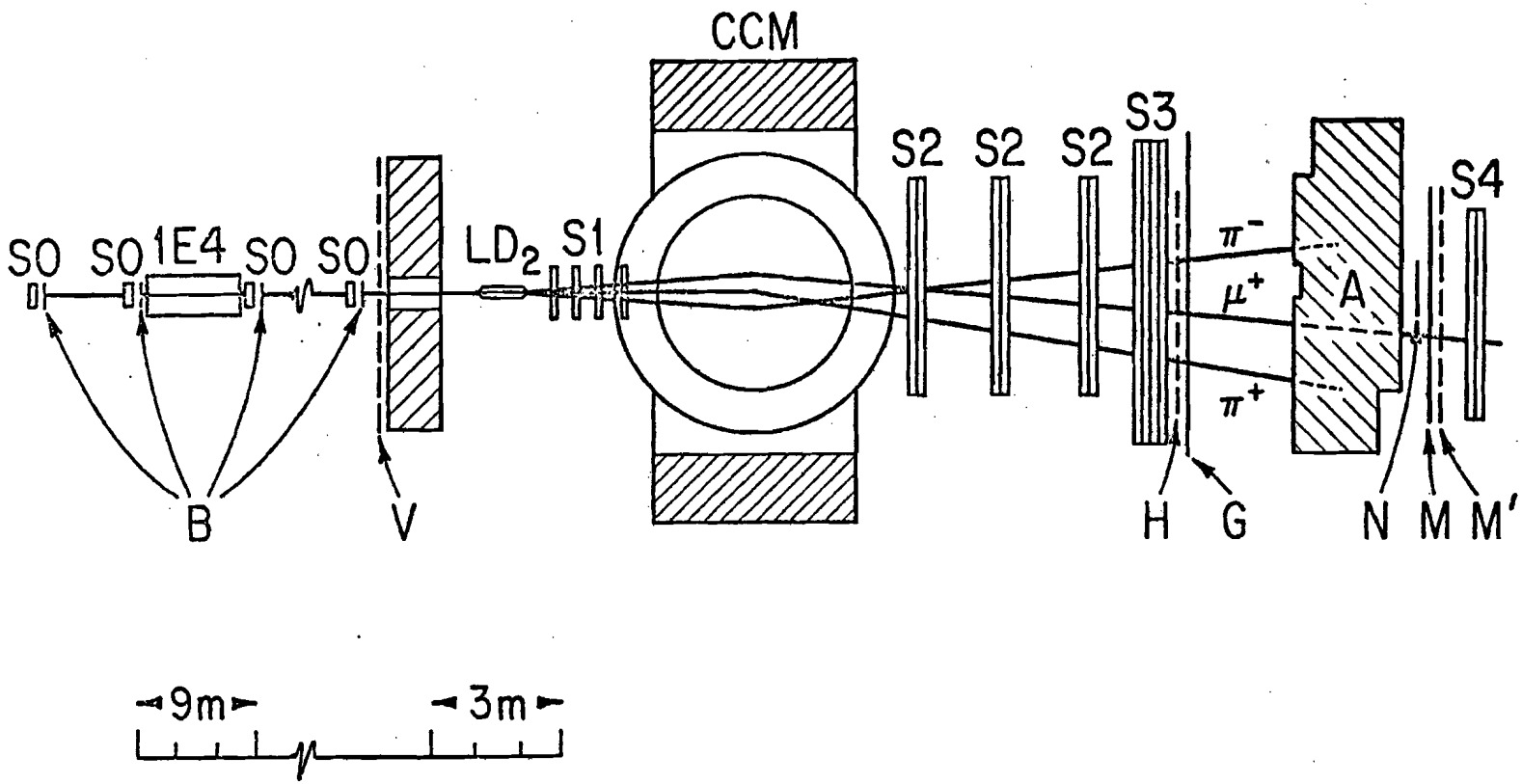

Figure 6.--Diagram of the apparatus. S0-4 are wire chambers, 1E4 is the beam muon tagging magnet, LD_2 is the liquid deuterium target, CCM is the spectrometer magnet, A is the steel hadron absorber, and B, V, H, G, N, M, and M' are scintillator hodoscopes. The lines emanating from the target represent the tracks seen when the apparatus is triggered by a typical event of the reaction under study.

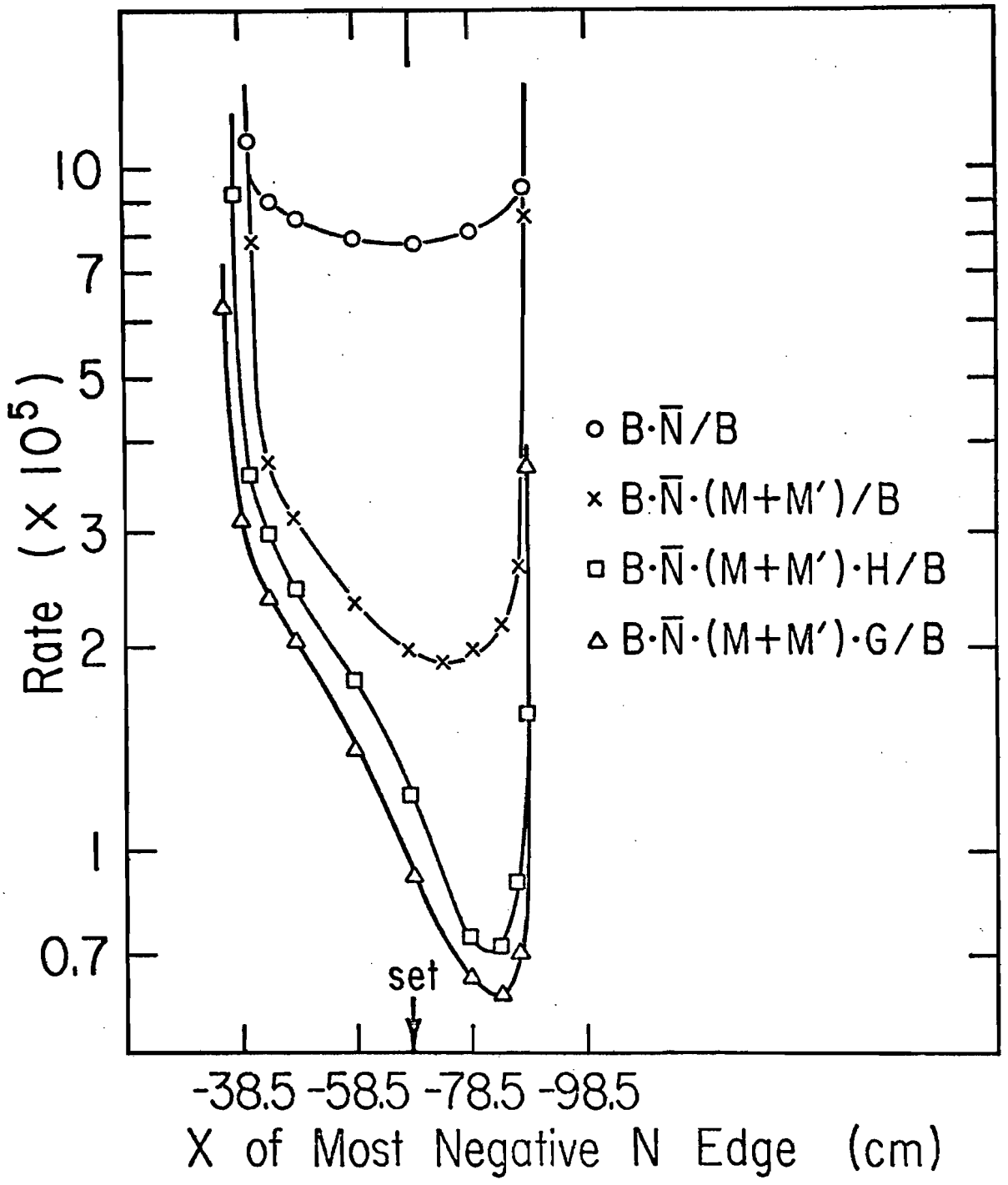

Figure 7.--Variation of several counting rates as a function of the position of the N-veto counter across the beam. The origin of the x-axis is the point where the undeflected, nominal beam intersects the plane of the N counter. The CCM bends positively charged particles towards negative X.

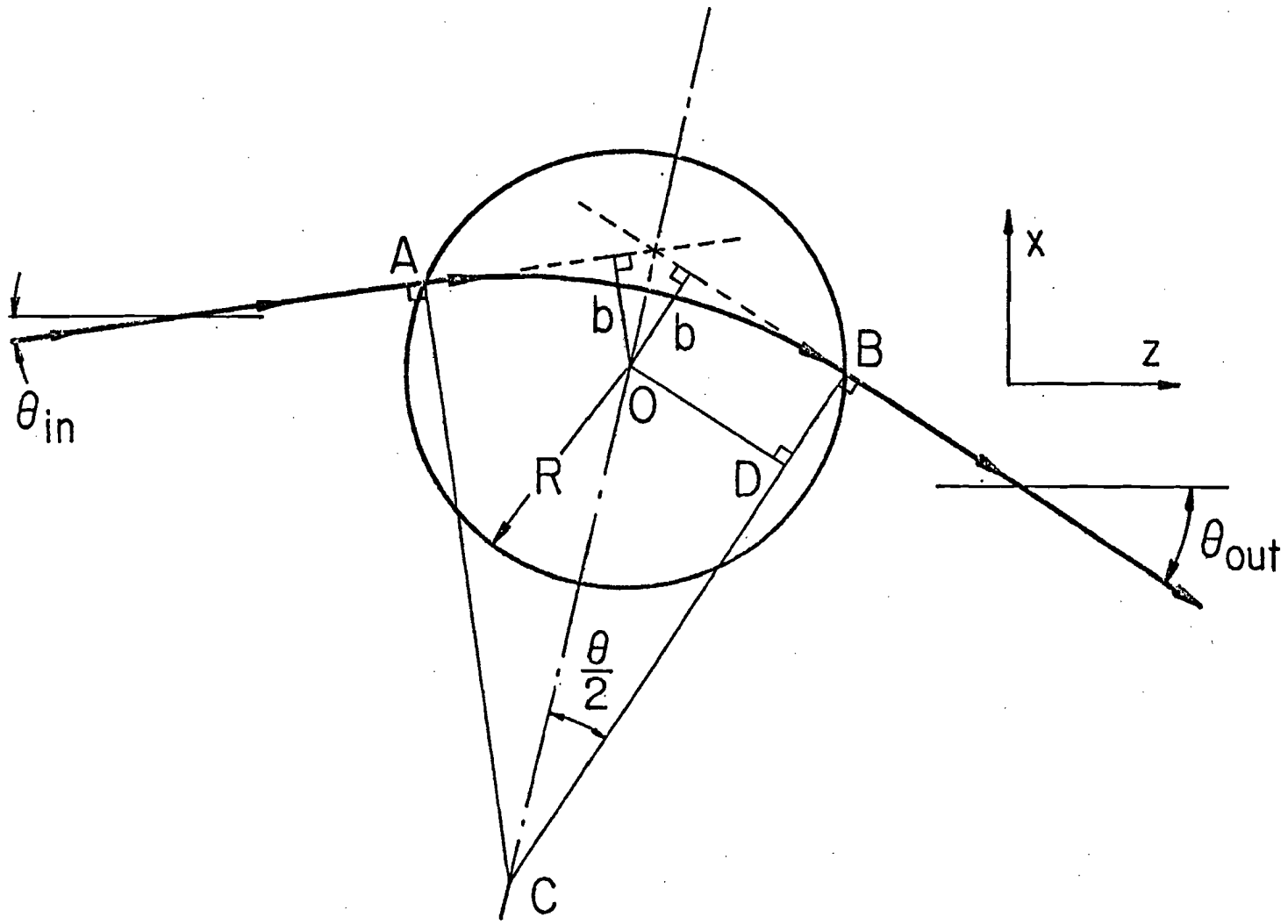

Figure 8.--Geometry of a bending plane trajectory for a sharp-edged model of the CCM field. Inside the field region (circle of center O and radius R) the particle path is a segment of the circle with center C and radius CA = CB. The entry and exit trajectories are tangents to this circle at A and B and their impact parameters (b) are equal.

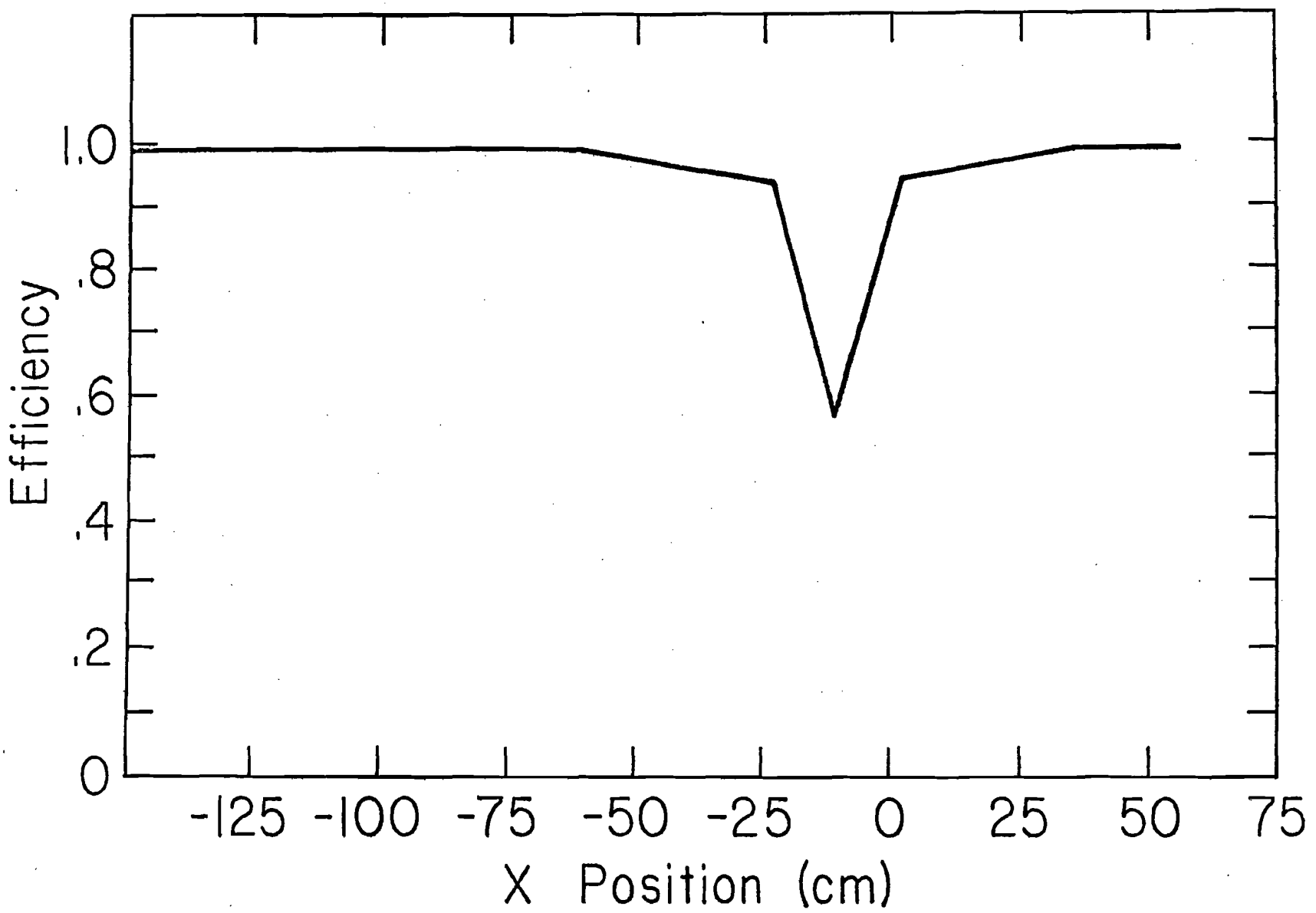

Figure 9.--Downstream trackfinding efficiency variation along the horizontal direction. The curve refers to the active area of the 6 m chambers. The dip occurs in the region surrounding the deadener and is primarily due to confusion from too many tracks near the beam.

Figure 10.--Tertiary tape information about an event. This event exhibits the downstream signature that characterizes the reaction under study. Track slopes are expressed in tenths of a radian and track intercepts in quarters of a millimeter. Distances along the z-axis are given in quarters of a centimeter while distances perpendicular to it are given in quarters of a millimeter. In these units the product of a slope with a z-distance is expressed in quarters of a millimeter and is directly comparable to all distances transverse to the z-axis.

```
EVENT     647   RUN     692

G HODOSCOPE 1 TO 20  0 0 0 0 0 0 0 0 1 1          1 0 0 0 0 0 0 0 0 0
H HODOSCOPE 1 TO 24  0 0 0 0 0 0 0 1 1 1 0 0        0 1 0 0 0 0 0 0 0 0 0 0
N HODOSCOPE 1 TO 22  0 0 0 0 0 0       0 0 0 0 0 0          0 0 0 1 0 0 0     0 0 0
N HODOSCOPE 1 TO 13  0 0 0 0 0 0 0 0 0 0 0 0 0
* HODOSCOPE 1 TO 20  0 0 0 0 0 0 0 0 0 0          0 0 0 0 0 1 0 0 0 0

MUON CHAMBER TRACKS

TRACK NO.      X-SLOPE      X-INTCPT      Y-SLOPE      Y-INTCPT      NO.OF SPARKS      X-CHISQ      Y-CHISQ
    1          -1.5554      6688.3        -0.2645      1091.9          4             0.784E+02
COUNTERS LATCHED      G 10      H 14      H 0      N 0      H' 16          CODE 1 2 4 816  CLASS   2

    2          -0.4236      -227.4        -0.1455      635.3           4             0.540E+01
COUNTERS LATCHED      G 9       H 10      H 16     N 8      H' 16          CODE 1 2 4 016  CLASS   1

    3          -0.1340      161.0         -0.4329      2924.4          3             0.116E+02
COUNTERS LATCHED      G 0       H 0       H 0      N 0      H' 0           CODE 1 0 0 8 0  CLASS   0

HADRON CHAMBER TRACKS

TRACK NO.      X-SLOPE      X-INTCPT      Y-SLOPE      Y-INTCPT      NO.OF. SPARKS      CHISQ      G-SPARKS      N-SPARKS      MOMENTUM
    1          -0.6826      -91.0         0.1218       190.7           17            0.968E+02     54.000        1.000         31.3212      HADR
COUNTERS LATCHED      G 11      H 8       H 0      N 0      H' 0           CODE 1 2 4 016  CLASS   1

    2          -0.4286      -189.8        -0.0149      -156.1          20            0.378E+02     20.000        10.000        53.3624      MUON
COUNTERS LATCHED      G 9       H 10      H 16     N 0      H' 16          CODE 1 2 4 016  CLASS   1

    3          -0.1490      153.2         0.0165       -16.0           19            0.496E+03     23.000        19.000        0.0
COUNTERS LATCHED      G 0       H 0       H 0      N 0      H' 0           CODE 1 0 0 8 0  CLASS   0

    4          0.3634       -186.9        -0.0560      -190.7          19            0.360E+02     8.000         52.000        69.3710      HADR
COUNTERS LATCHED      G 10      H 14      H 0      N 0      H' 0           CODE 1 2 4 016  CLASS   1


LINKING RESULTS

HADRON TRACK NO.   1 IS LINKED TO MUON TRACK NO.   0      HADRON TRACK NO.   2 IS LINKED TO MUON TRACK NO.   2
HADRON TRACK NO.   3 IS LINKED TO MUON TRACK NO.   3      HADRON TRACK NO.   4 IS LINKED TO MUON TRACK NO.   0

THERE ARE   1 HADRON TRACKS WHICH COULD BE THE SCATTERED MUON: TRACKS NO.  2

KINEMATIC QUANTITIES

Q-SQUARED (GEV/C)**2          NU (GEV)                          DELTA PLONG     TOTAL ENERGY DOWNSTREAM
   0.0200     0.0       0.0      89.8230     0.0       0.0          -0.8661          144.0547

THE INCIDENT MUON HAD AN ENERGY OF     143.185 GEV
    1          -0.0009     -172.6      -0.0002      -128.1

PROPORTIONAL CHAMBER TRACKS

VERTEX FOUND AT: X =    -159.16   Y =    -101.18   Z =   -2489.25

THERE ARE    5 UPSTREAM TRACKS STARTING AT    14

TRACK NO.      X-SLOPE      X-INTCPT      Y-SLOPE      Y-INTCPT      NO.OF SPARKS      X-CHISQ      Y-CHISQ
    1          0.0          0.0           -0.0495      -222.3          3             0.190E+00     0.0           0.0
    2          0.0          0.0           -0.0207      -154.8          3             0.198E+00     0.0           0.0
    3          -0.0084      -183.7        0.0          0.0             4             0.508E+01     0.0           0.0
    4          0.0292       -87.9         0.0          0.0             4             0.616E+00     0.0           0.0
    5          0.0          0.0           0.1098       172.2           2             0.160E+03     0.0           0.0

TWO POINT TRACKS IN THE M.W.P.C.S WHICH POINT TO DOWNSTREAM IMPACT PARAMETERS START AT    18
    1          0.0          0.0           0.1098       172.2

UPSTREAM AND DOWNSTREAM LINKING

THERE ARE    4 DNSTREAM TRACKS STARTING AT     7
HADRON TRACK NO.   1 IS LINKED TO UPSTREAM TRACKS   4   5
HADRON TRACK NO.   2 IS LINKED TO UPSTREAM TRACKS   1   2   3
HADRON TRACK NO.   4 IS LINKED TO UPSTREAM TRACKS   1   2   3

THERE ARE  1 SCATTERED MUONS AND  2 HADRONS.
```

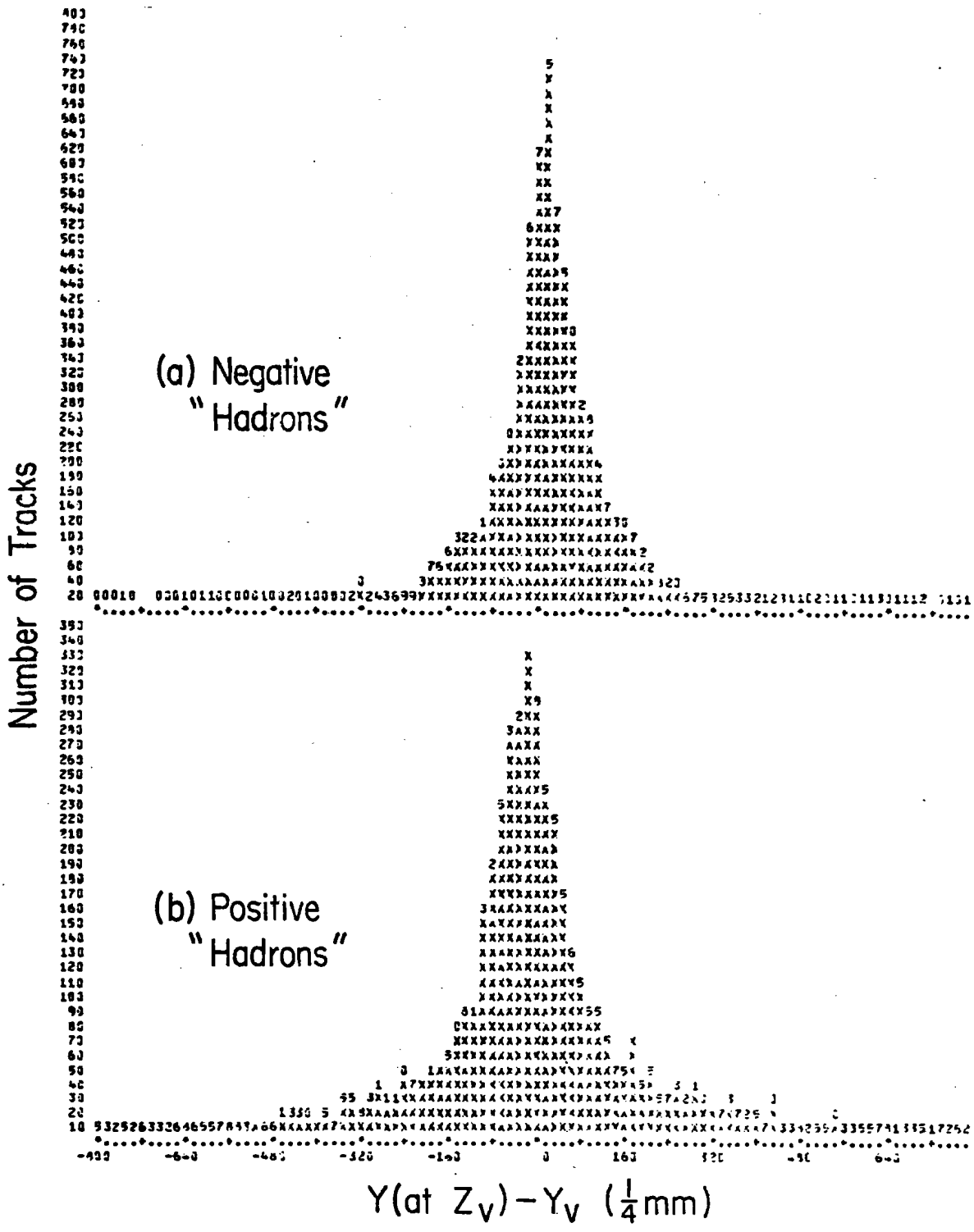

Figure 11.--Projection to the vertex of downstream Y-Z "hadron" tracks. We plot the difference between the projection of the track at the z of the vertex and the y of the vertex separately for tracks of (a) negatively charged and (b) positively charged particles assigned momentum, except for the scattered muon track. The wider wings of the positives indicate that they are contaminated by halo muons. A cut at ± 200 quarter millimeters was imposed.

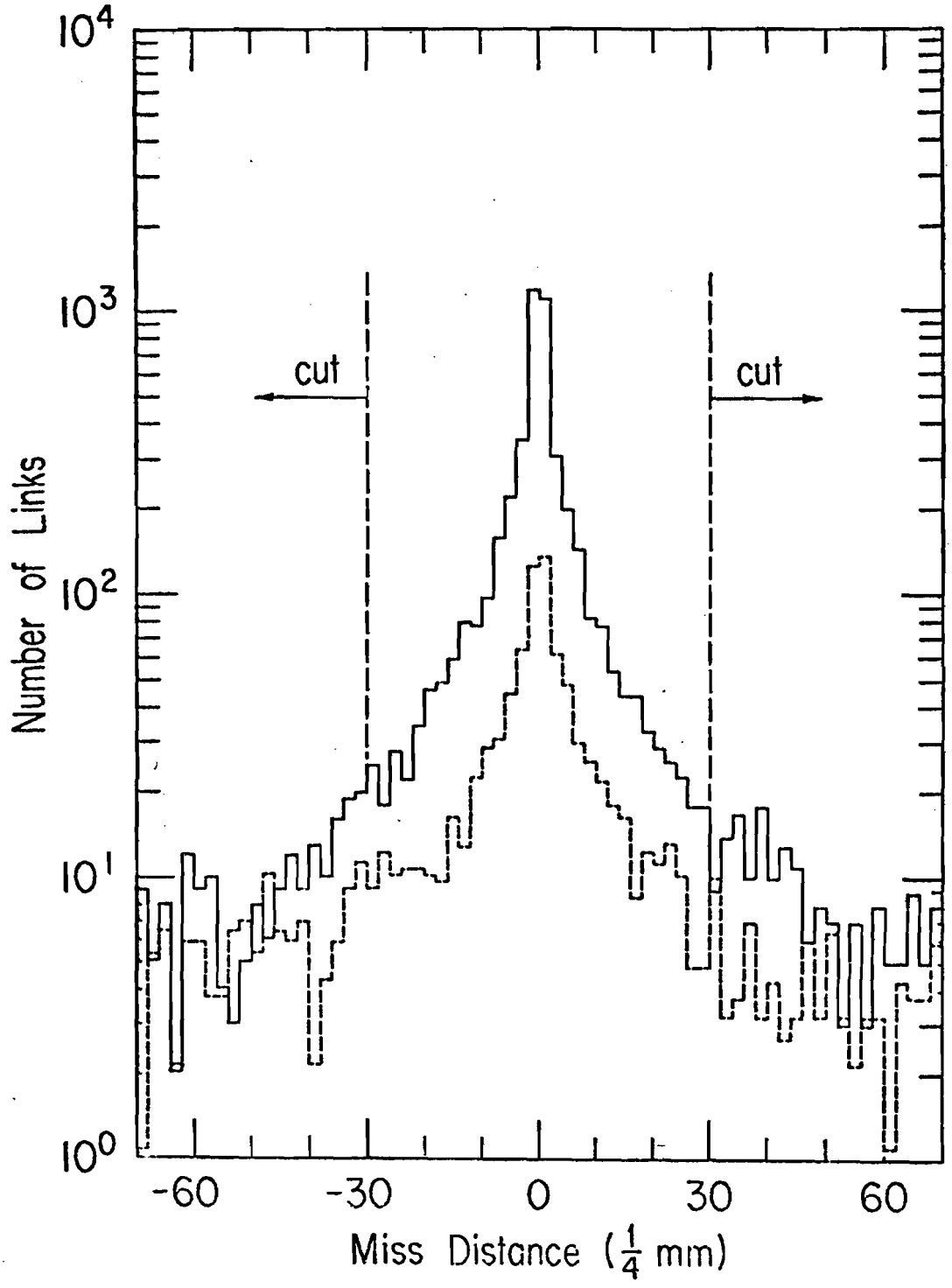

Figure 12.--Projection to the vertex of upstream X-Z "hadron" tracks. The solid line shows the distribution of the difference between the track's projection at the z of the vertex from the x of the vertex, for tracks linking to downstream "hadron" tracks which point, within ± 200 quarter millimeters, to the y of the vertex. The dashed line is our estimate for the maximum background by halo muons.

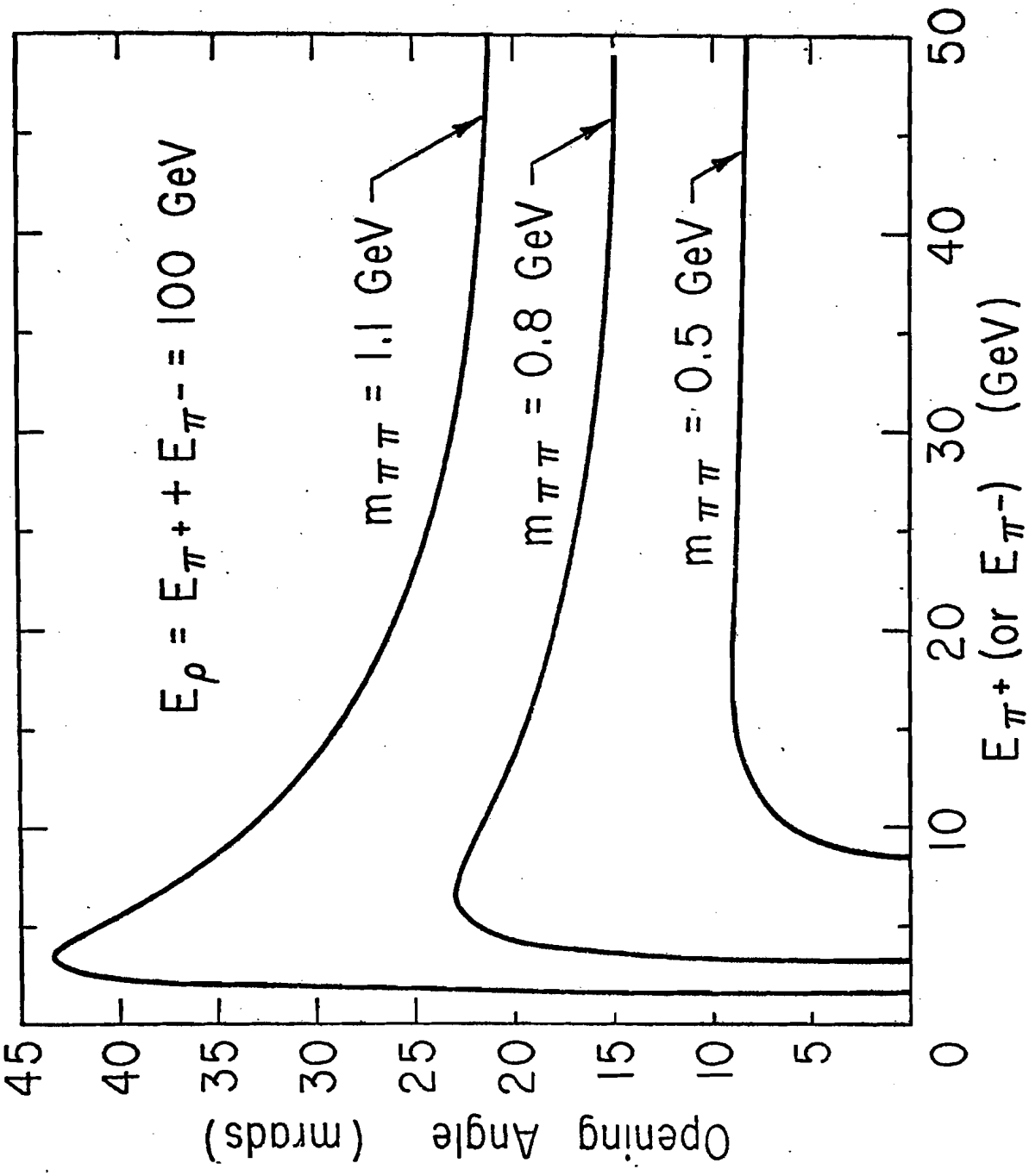

Figure 13.--Pion pair opening angle vs. pion energy for 100 GeV ρ decay. Most of the opening angles are expected to fall inside the 10 to 20 mrad range.

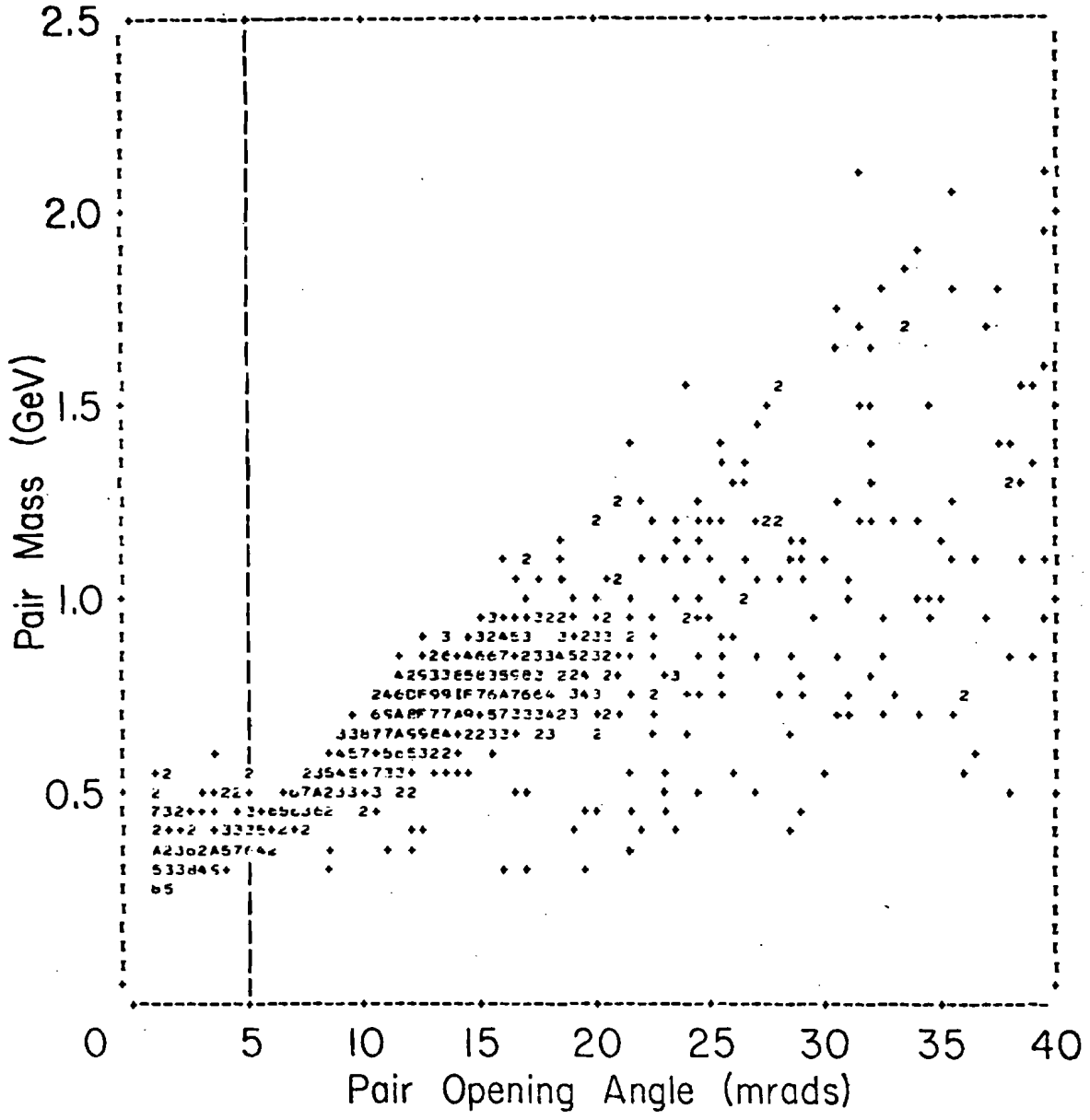

Figure 14.--Pion pair mass vs. opening angle. The symbols +, 2-9, and A-U indicate 1, 2-9, and 10-30 events, respectively, falling in a bin. The indicated 5 mrad cut in opening angle preferentially removes events with small invariant dipion mass.

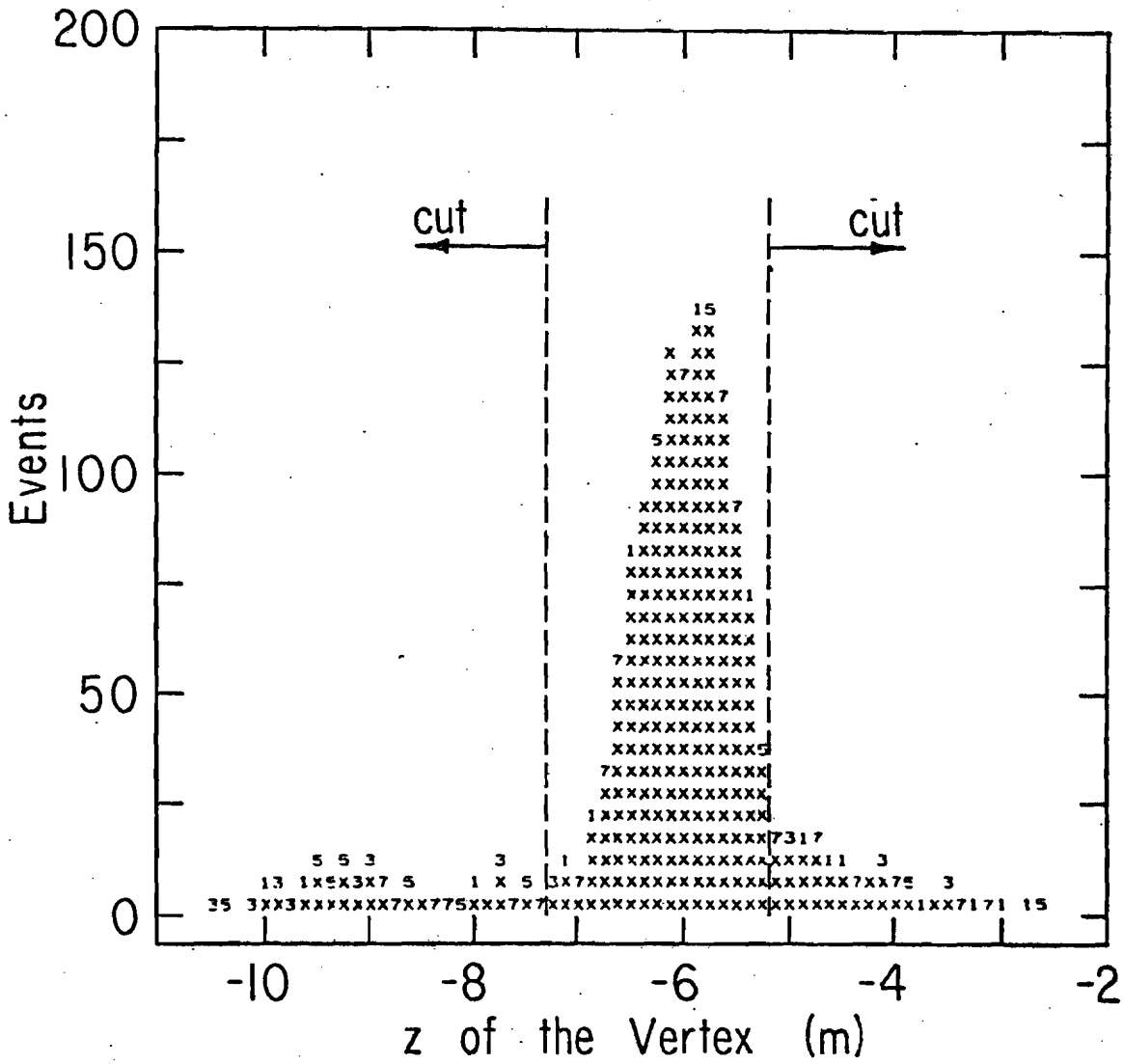

Figure 15.--Z position of the interaction vertex. The target peak is sharp, in spite of the low average Q^2, due to the presence of the pion tracks. The secondary peak at -9.5 m is produced by the material of the set of beam hodoscopes and beam chambers nearest to the target.

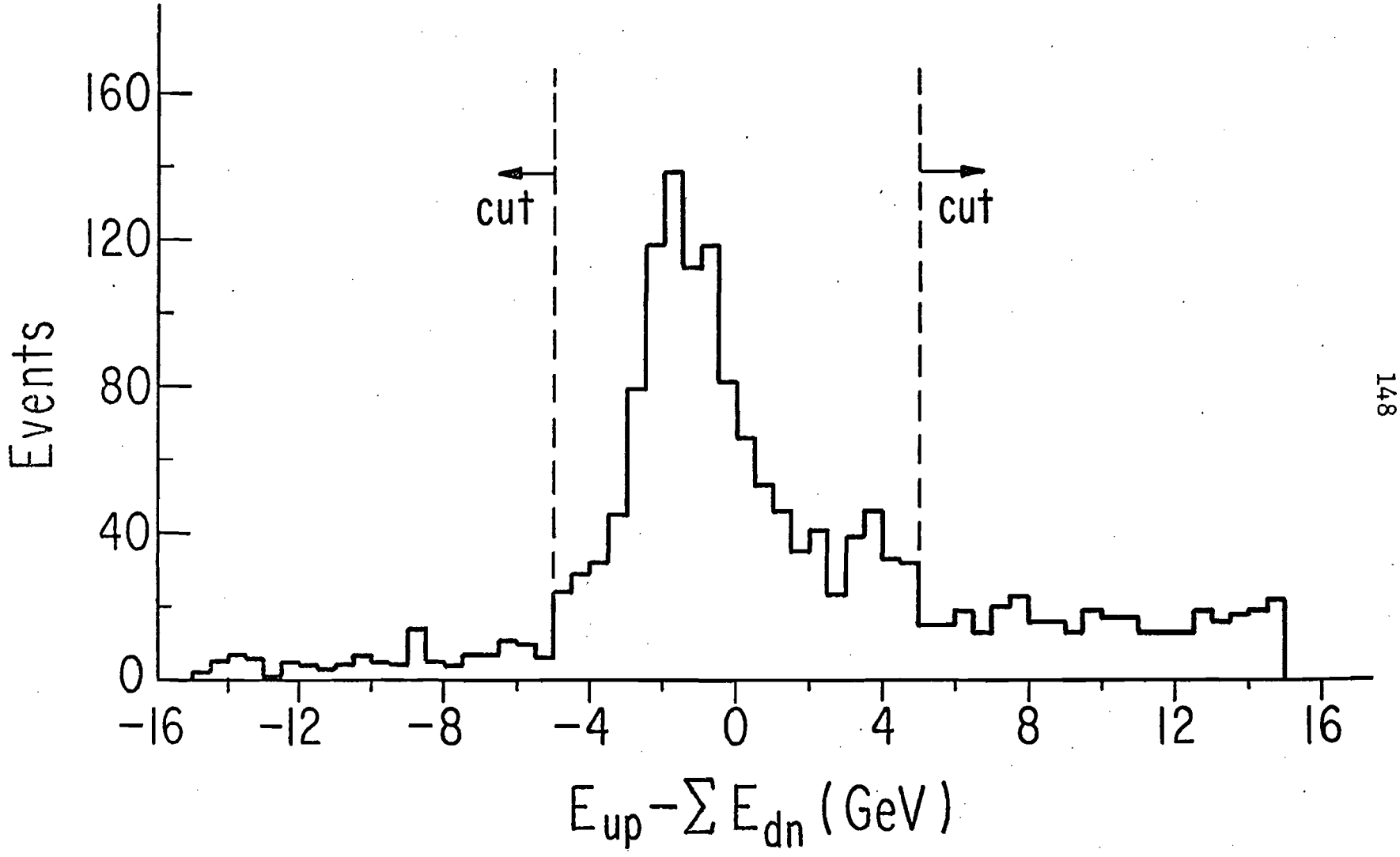

Figure 16.--Energy balance distribution. Events with unobserved neutral particles (including photons) in the final state populate the tail of upstream energy excess, which is seen to be higher.

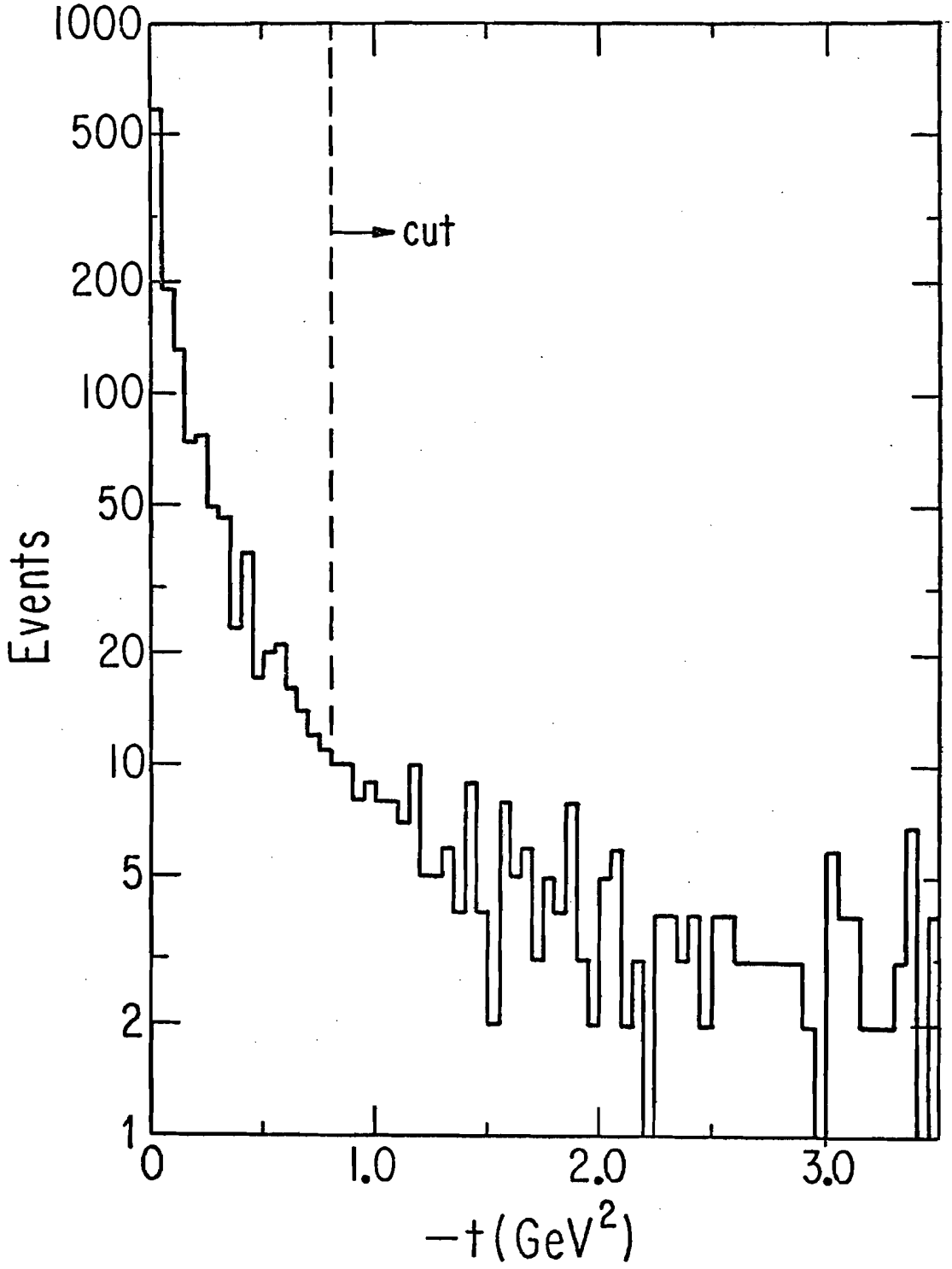

Figure 17.--Event t distribution. An excess of events is evident in the very forward direction. It corresponds to coherent production ($\gamma^* d \rightarrow \rho d$). The cut at $t = -0.8$ GeV^2 enhances the diffractively produced signal.

Figure 18.--Scattered muon acceptance variation with Q^2 and ν. The large rectangle, outlined by dashed lines, indicates the position of the N veto counter. The two small satellite rectangles are the (software) vetoes and correspond to the thick portion of the light guides of the same counter. Each set of $\{Q^2, \nu\}$ values determines a unique circle at the plane of the N counter. The scattered muon is equally likely to land on any point of the periphery of this circle. The acceptance is the fraction of the circumference of this circle outside the rectangles. For $\nu < 80$ GeV most of the events with $Q^2 < 3$ GeV^2/c^2 are vetoed.

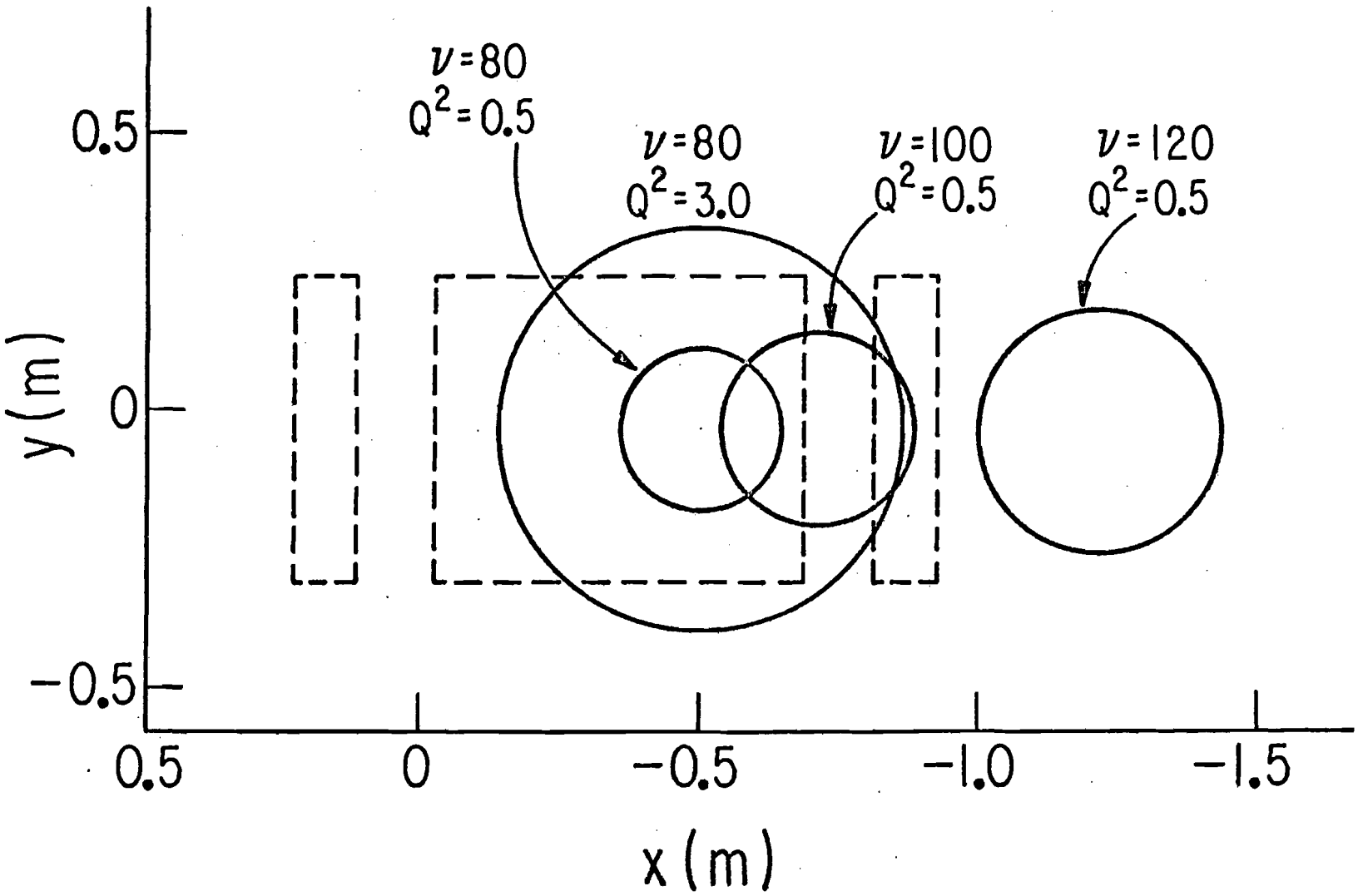
ν=80
Q²=0.5
ν=80
Q²=3.0
ν=100
Q²=0.5
ν=120
Q²=0.5
0.5
0
−0.5
y (m)
0.5
0
−0.5
−1.0
−1.5
x (m)

Figure 19.--Q^2-ν distribution of the events passing all cuts. The boundaries of the bins are shown together with the minimum kinematically allowed Q^2 for 150 GeV incident muons. The latter line is not an imposed boundary but explains the observed lack of events below it.

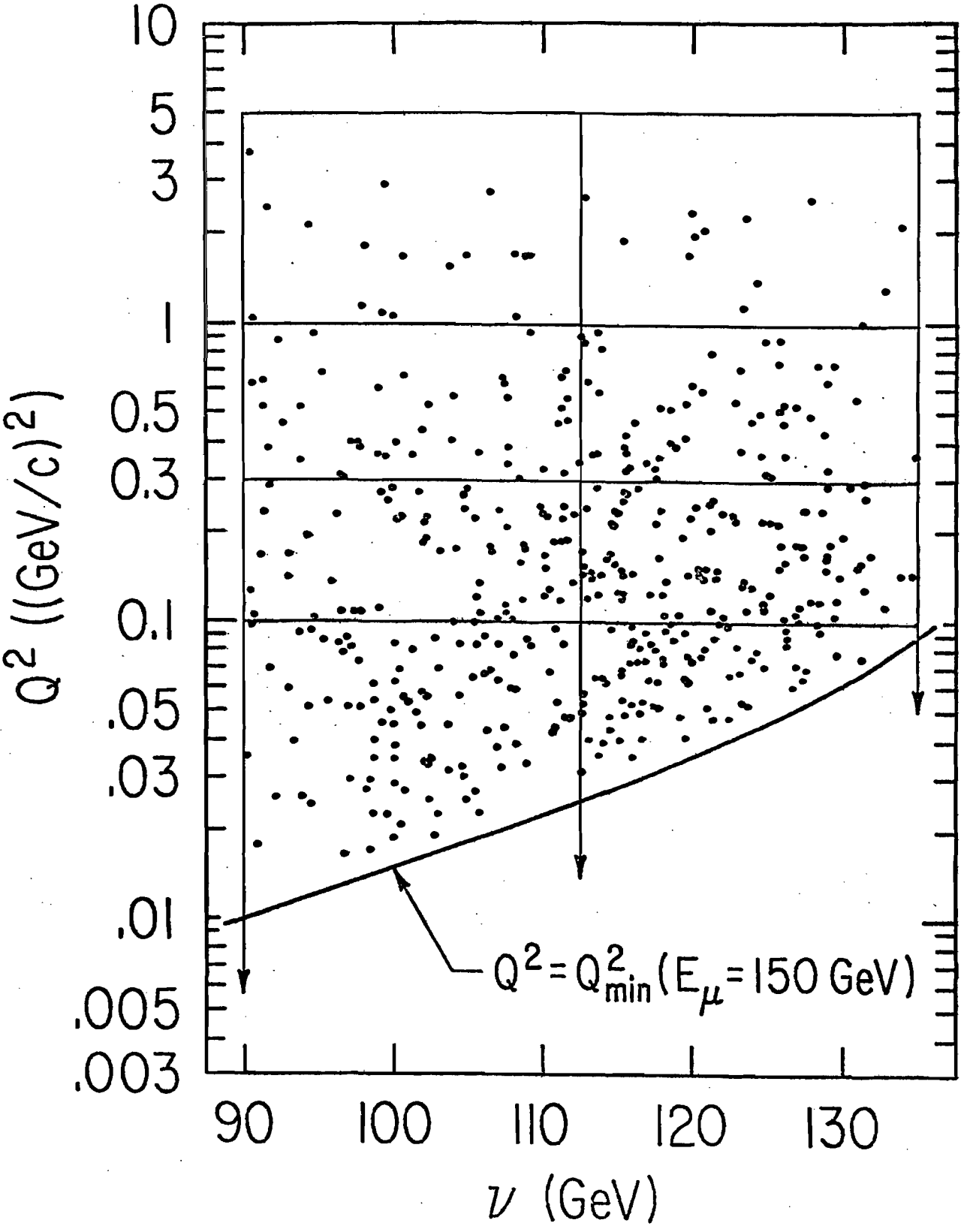
10
5
3
1
0.5
0.3
0.1
.05
.03
.01
.005
.003
Q^2 ((GeV/c)^2)
$Q^2 = Q^2_{min}(E_\mu = 150$ GeV)
90
100
110
120
130
ν (GeV)

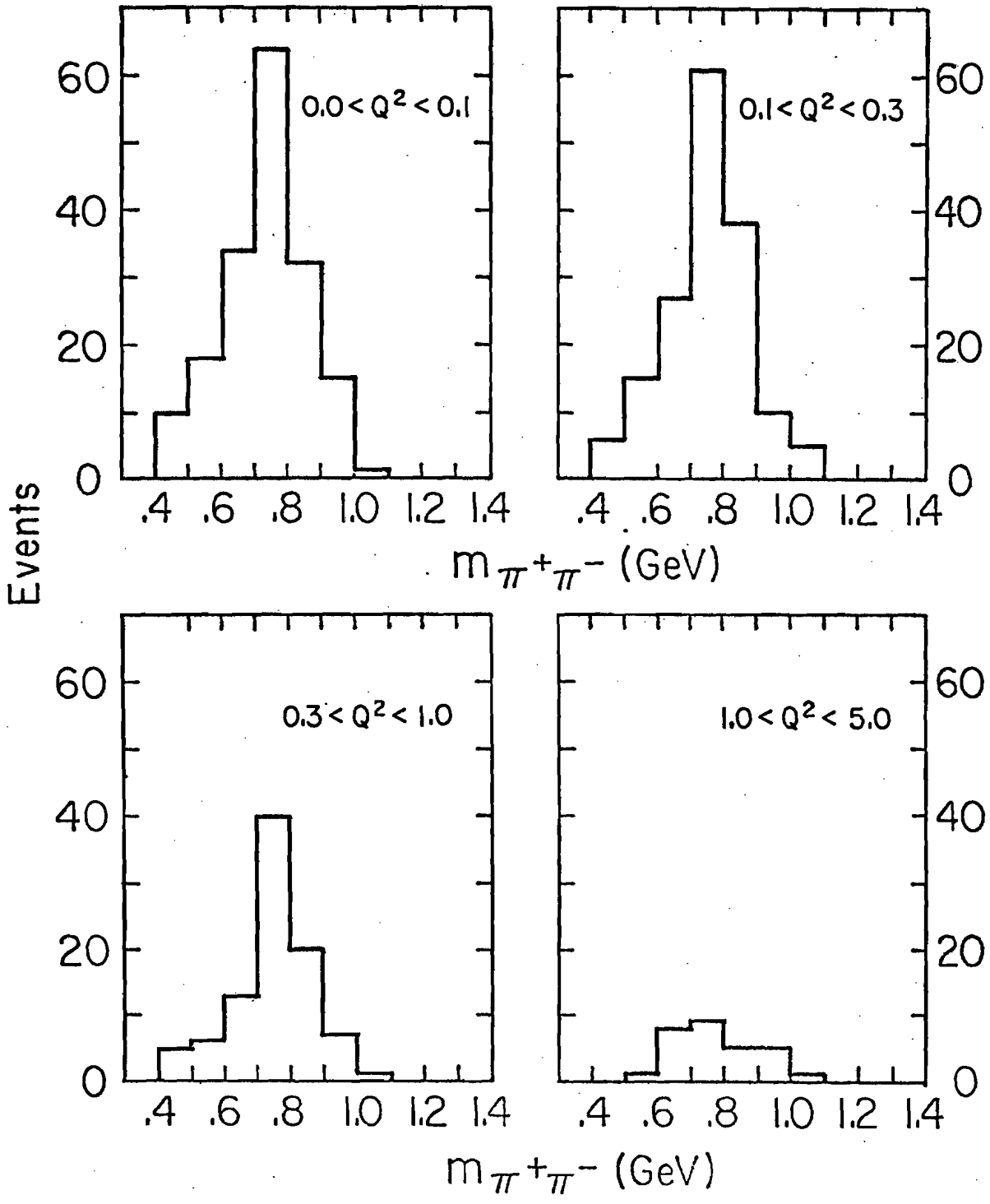

Figure 20.--Dipion invariant mass histograms for the four Q^2 ranges. The presence of a ρ^o signal, which depends strongly on Q^2, is already evident.

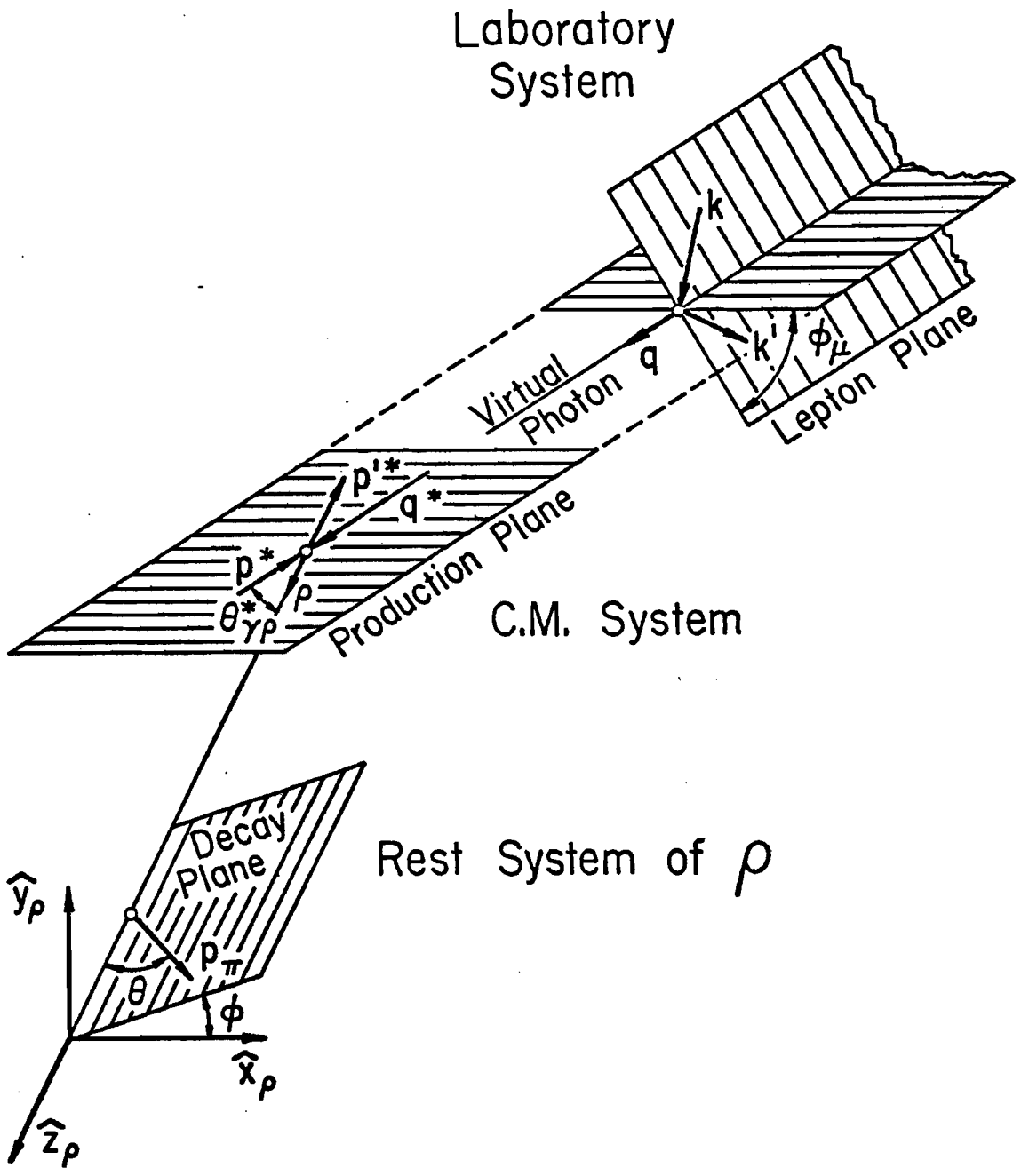

Figure 21.--Definition of the angles of the rho-decay angular distribution. The angle between the μ scattering plane and the ρ production plane is designated as ϕ_μ. The polar and azimuthal angles of the π^+ in the rest frame of the ρ are designated by θ and ϕ, respectively. The functional form of the angular distribution is given in page 89.

Figure 22.--Raw mass differential cross sections, per nucleon, for the four Q^2 ranges. The ρ signal persists as a result of the flatness of the acceptance across m, for a given Q^2 range (see Table 7). The slow increase of the acceptance with increasing Q^2 does not result in any significant change in the strong Q^2 dependence, observed at the event distribution level (see Table 4 and Figure 20).

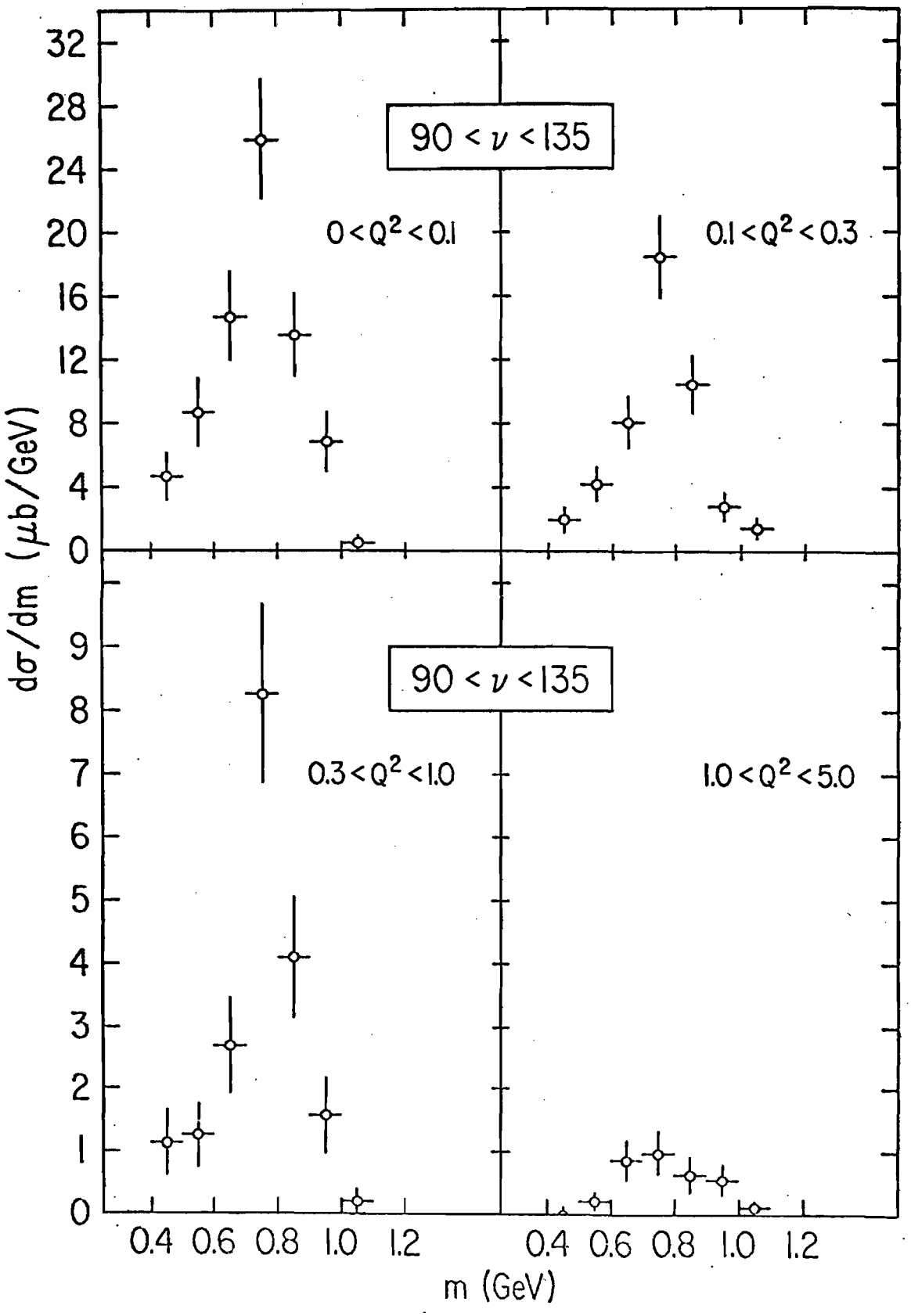
90 < ν < 135
0 < Q² < 0.1
0.1 < Q² < 0.3
90 < ν < 135
0.3 < Q² < 1.0
1.0 < Q² < 5.0
dσ/dm (μb/GeV)
m (GeV)
0
4
8
12
16
20
24
28
32
0
1
2
3
4
5
6
7
8
9
0.4
0.6
0.8
1.0
1.2

Figure 23.--Mass resolution. The curve joins the Monte Carlo estimates of the standard deviation of the fractional mass uncertainty. The mass resolution is approximately 30 MeV at $m = m_\rho$.

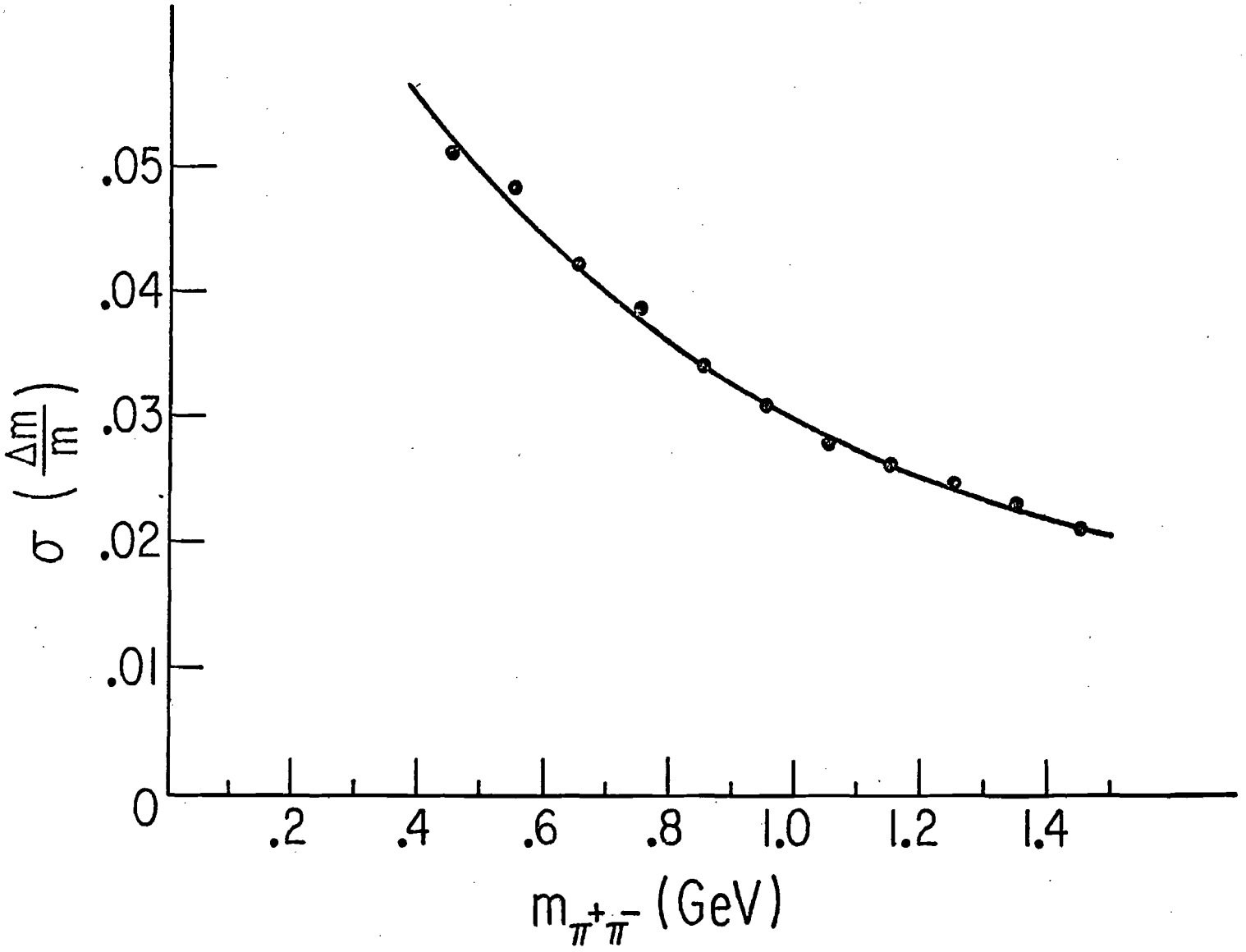
.05
.04
.03
.02
.01
0
σ (Δm/m)
.2
.4
.6
.8
1.0
1.2
1.4
m_{π+π−} (GeV)

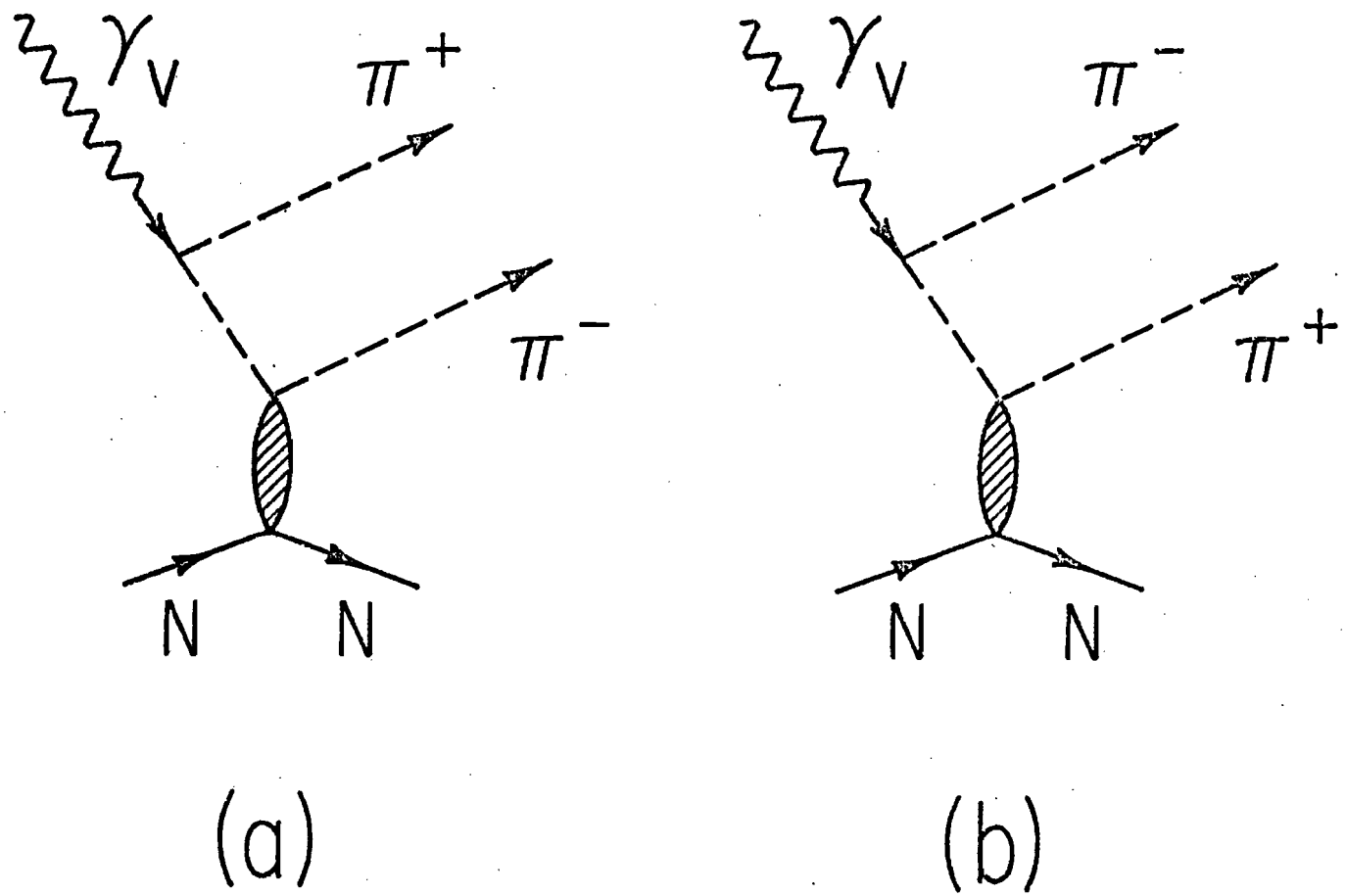

Figure 24.--Simulation of ρ production by the diffractive scattering of nonresonant pions. The scattered pion may be either (a) the negative or (b) the positive member of the pair observed in the final state. Such processes constitute a background. In addition, their amplitudes interfere with and distort the resonant signal.

Figure 25.--Resonant, nonresonant background, and interference components of the mass spectra. The functional form of each component is given by equation (V.8) in page 95.

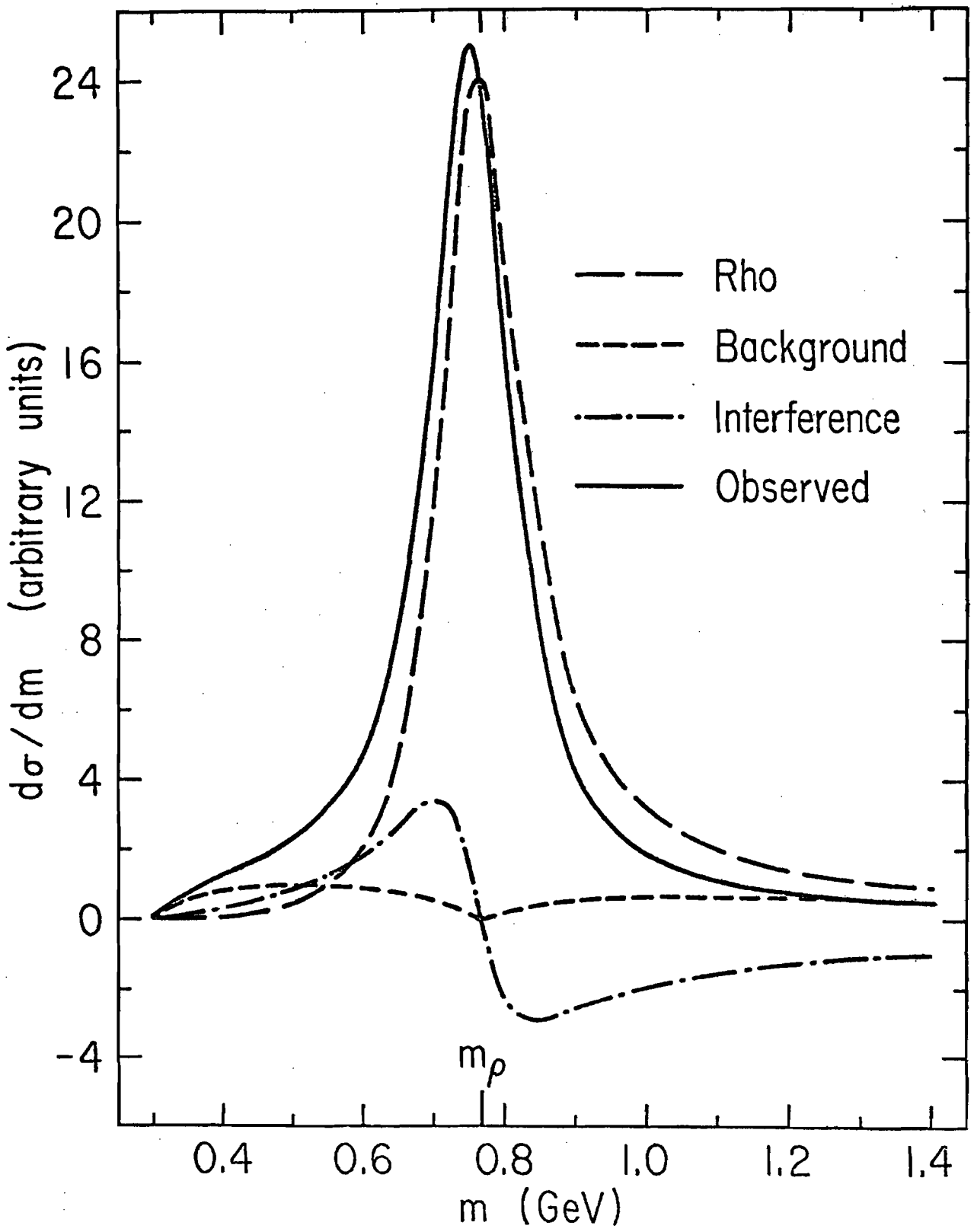
24
20
16
12
8
4
0
-4
dσ/dm (arbitrary units)
Rho
Background
Interference
Observed
m_ρ
0.4
0.6
0.8
1.0
1.2
1.4
m (GeV)

Figure 26.--Mass differential cross sections and fit for $0.0 < Q^2 < 0.1$ GeV^2/c^2. The data points have been corrected for resolution and then adjusted to represent the bin-centered values of the measured cross section, to allow a direct visual comparison. The functional form of the fit is that of equation (V.8) in page 95, with coefficients given in Table 14.

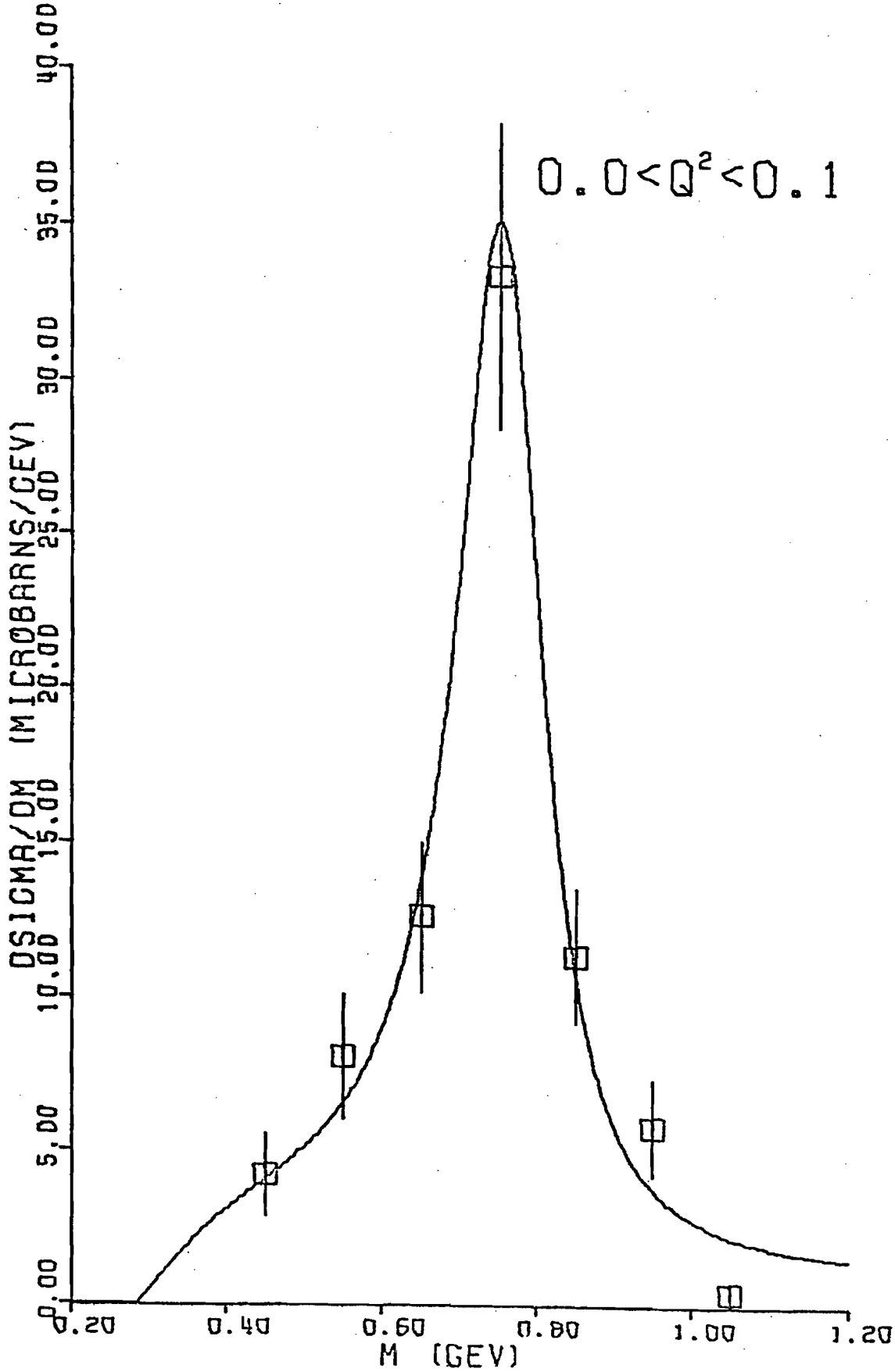
0.0<Q²<0.1
DSIGMA/DM (MICROBARNS/GEV)
0.00
5.00
10.00
15.00
20.00
25.00
30.00
35.00
40.00
0.20
0.40
0.60
0.80
1.00
1.20
M (GEV)

Figure 27.--Mass differential cross sections and fit for $0.1 < Q^2 < 0.3$ GeV^2/c^2. The data points have been corrected for resolution and then adjusted to represent the bin-centered values of the measured cross section, to allow a direct visual comparison. The functional form of the fit is that of equation (V.8) in page 95, with coefficients given in Table 14.

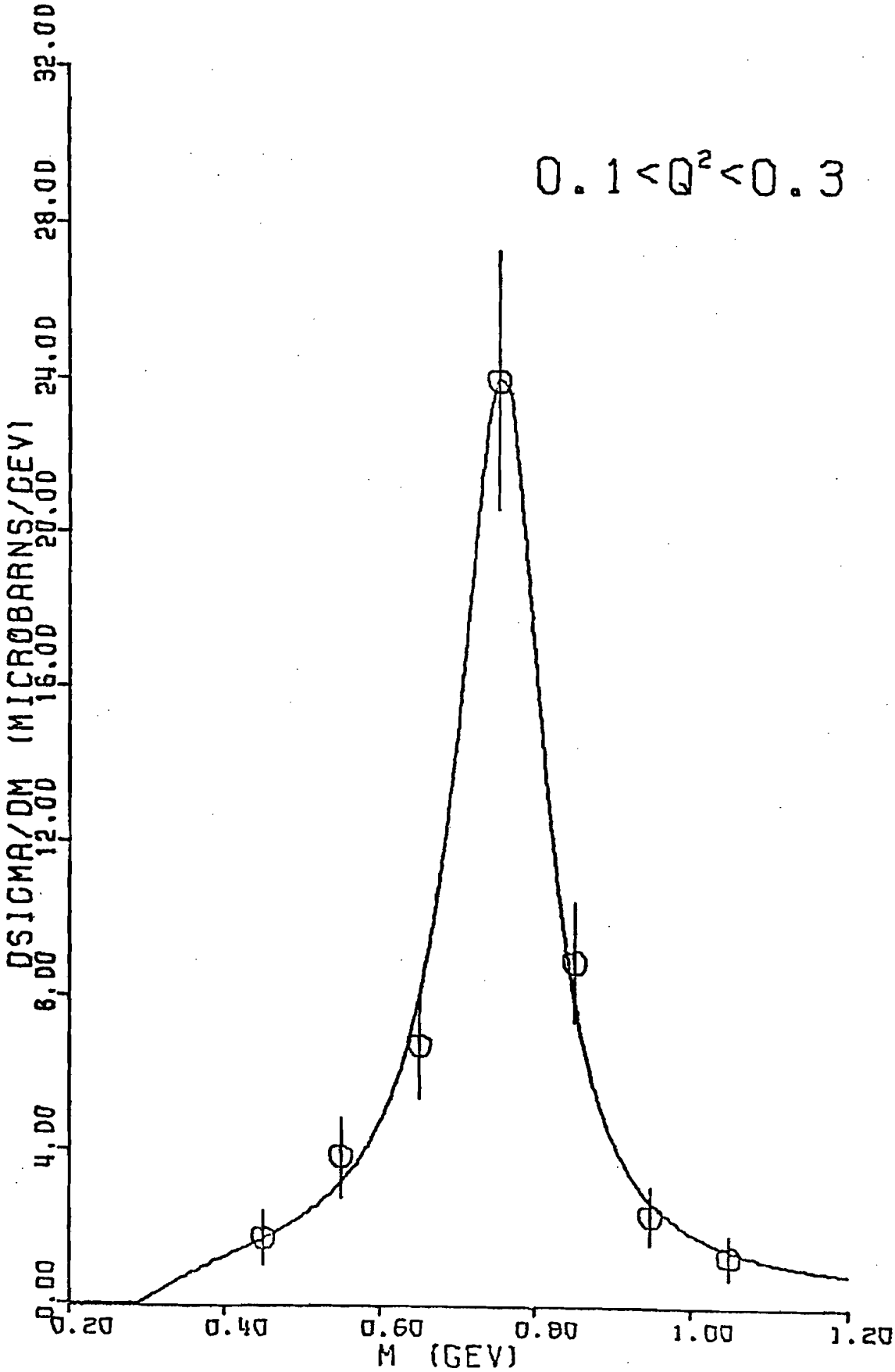
0.1<Q²<0.3
DSIGMA/DM (MICROBARNS/GEV)
0.00
4.00
8.00
12.00
16.00
20.00
24.00
28.00
32.00
0.20
0.40
0.60
0.80
1.00
1.20
M (GEV)

Figure 28.--Mass differential cross sections and fit for $0.3 < Q^2 < 1.0$ GeV^2/c^2. The data points have been corrected for resolution and then adjusted to represent the bin-centered values of the measured cross section, to allow a direct visual comparison. The functional form of the fit is that of equation (V.8) in page 95, with coefficients given in Table 14.

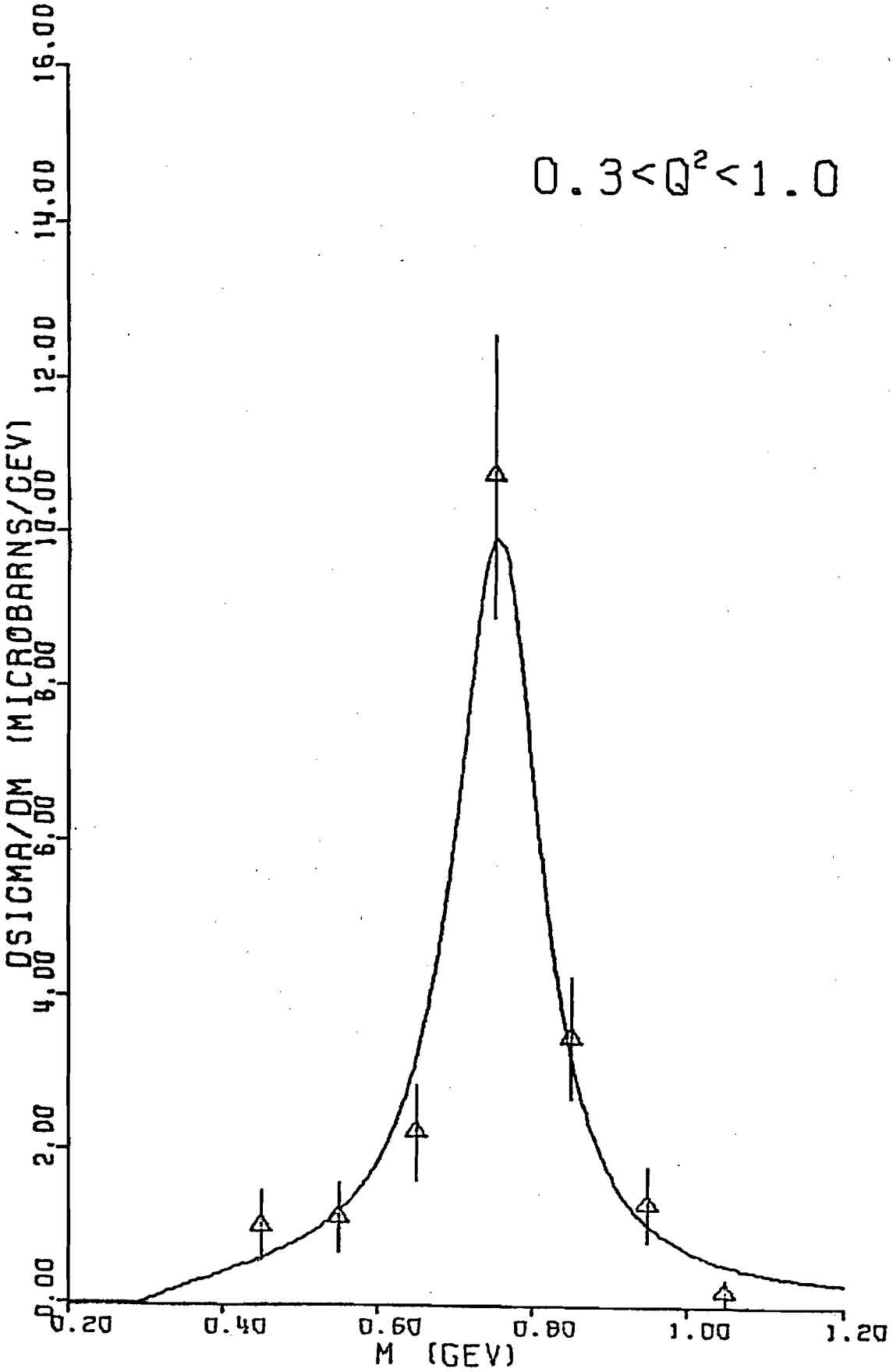
0.3<Q²<1.0
DSIGMA/DM (MICROBARNS/GEV)
0.00
2.00
4.00
6.00
8.00
10.00
12.00
14.00
16.00
0.20
0.40
0.60
0.80
1.00
1.20
M (GEV)

Figure 29.--Mass differential cross sections and fit for $1.0 < Q^2 < 5.0$ GeV^2/c^2. The data points have been corrected for resolution and then adjusted to represent the bin-centered values of the measured cross section, to allow a direct visual comparison. The functional form of the fit is that of equation (V.8) in page 95, with coefficients given in Table 14.

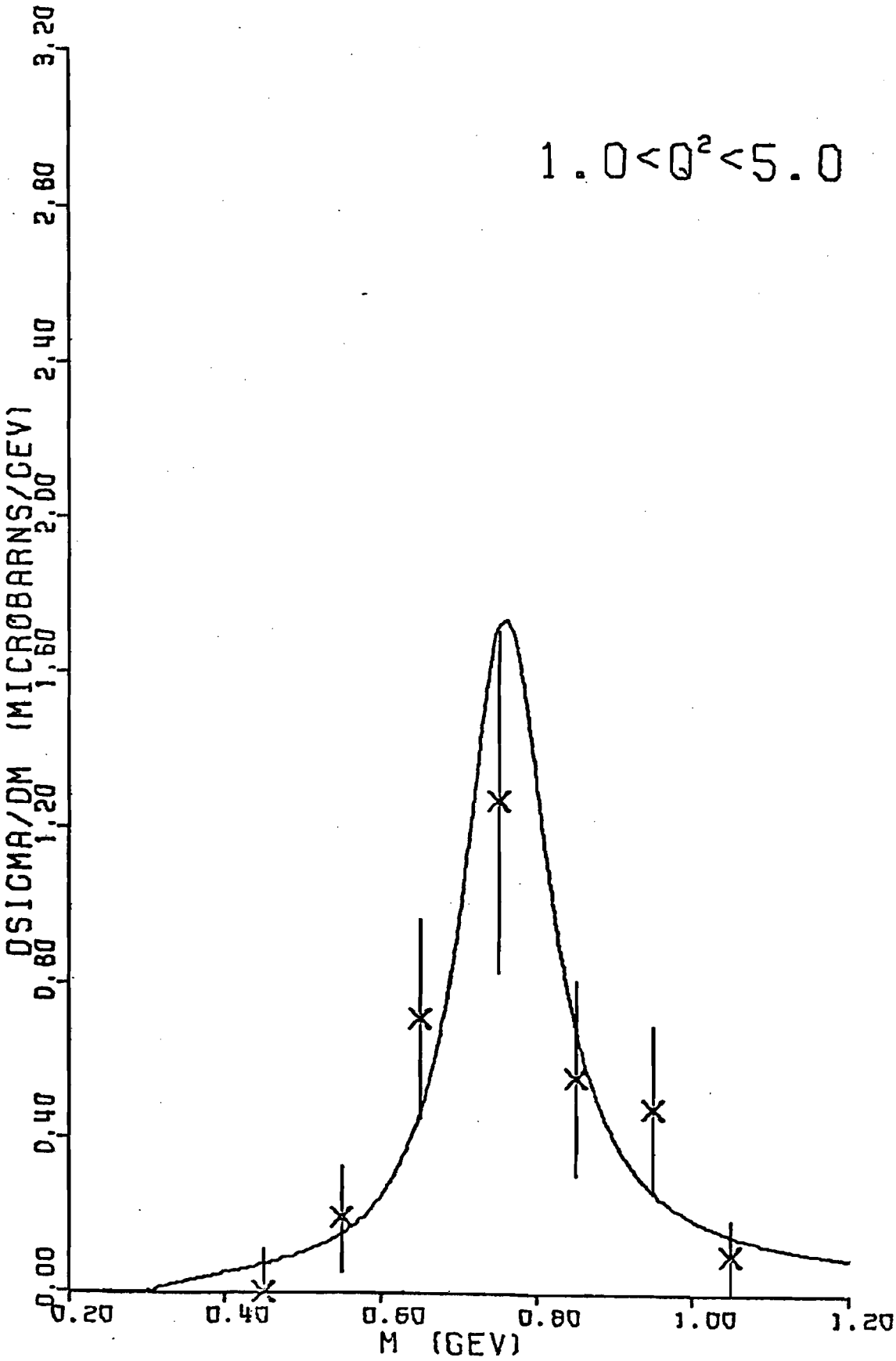
1.0<Q²<5.0
DSIGMA/DM (MICROBARNS/GEV)
0.00
0.40
0.80
1.20
1.60
2.00
2.40
2.80
3.20
0.20
0.40
0.60
0.80
1.00
1.20
M (GEV)

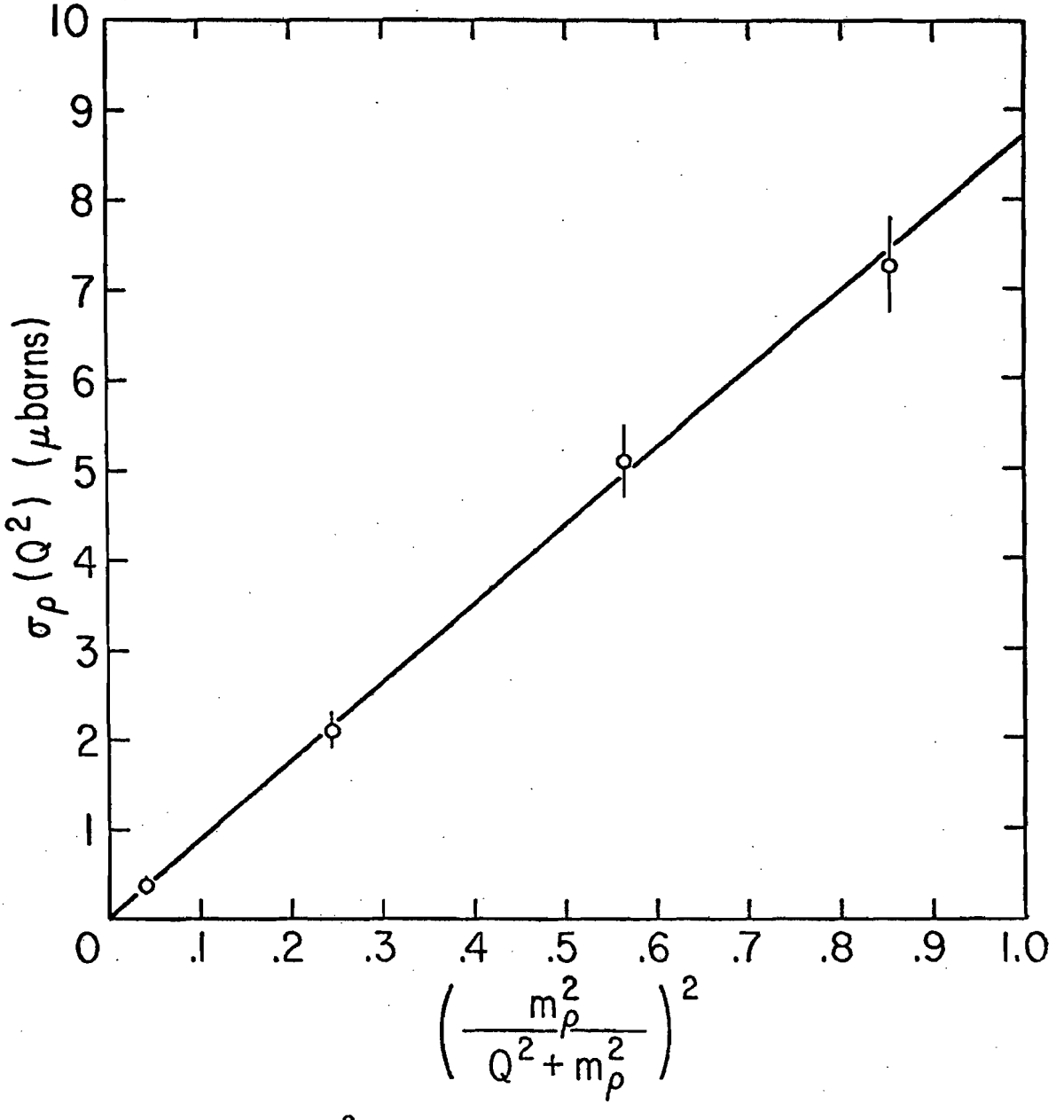

Figure 30.--Q^2 variation of the total ρ production cross section. Our results are consistent with a variation given by the square of the ρ propagator and shown by the straight line in this plot. The extrapolation to $Q^2 = 0$ predicts that the rho photoproduction cross section, $\sigma(\gamma p \rightarrow \rho p)$, is 8.7 ± 0.4 μbarns for incident (real) photons of energy 112 GeV.

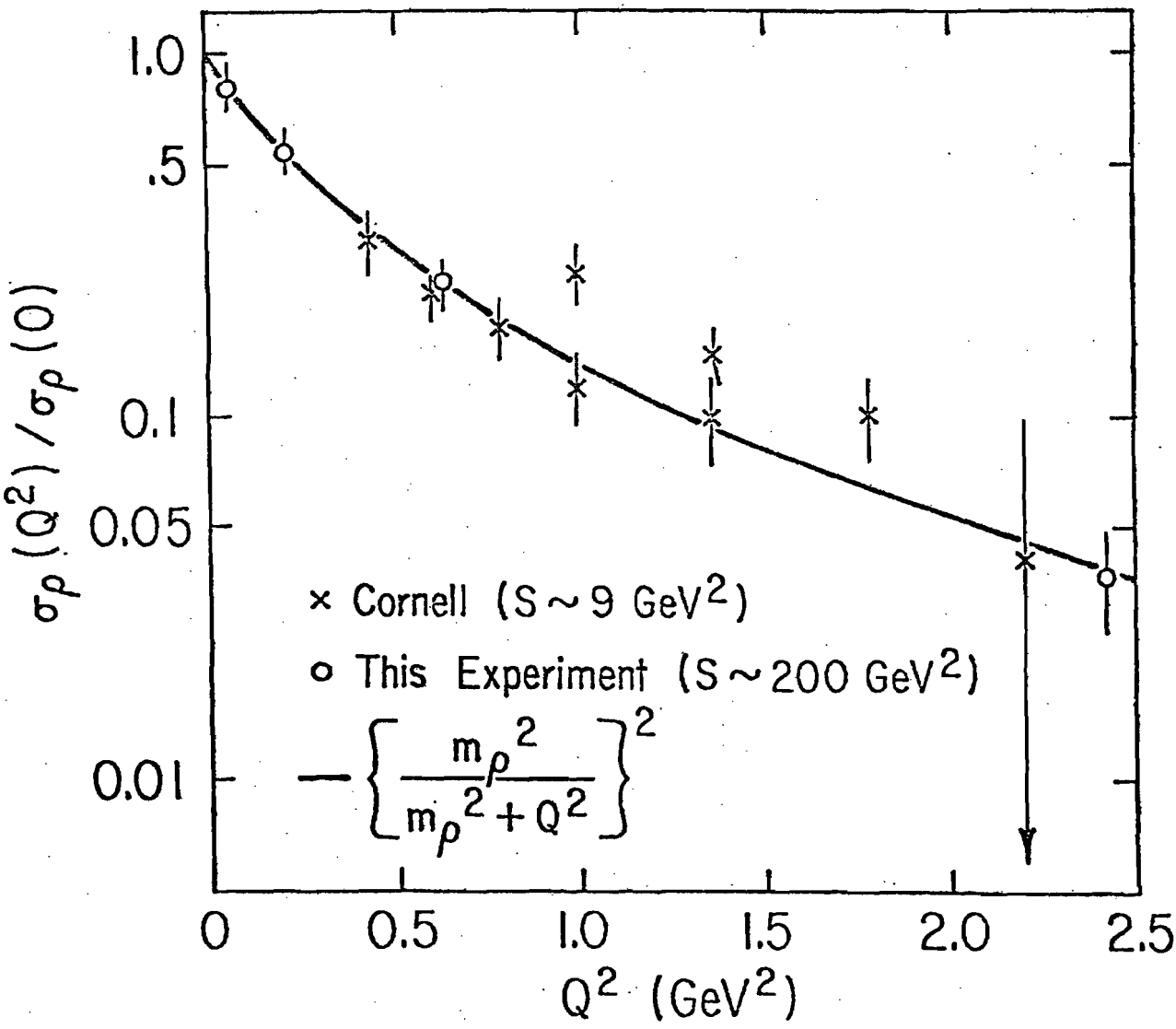

Figure 31.--Comparison of $\sigma_\rho(Q^2)$ measured by experiments performed at different energies. The curve shows the variation of the square of the ρ propagator and gives a good fit to both data sets. The "Cornell" data points are from Reference 15.

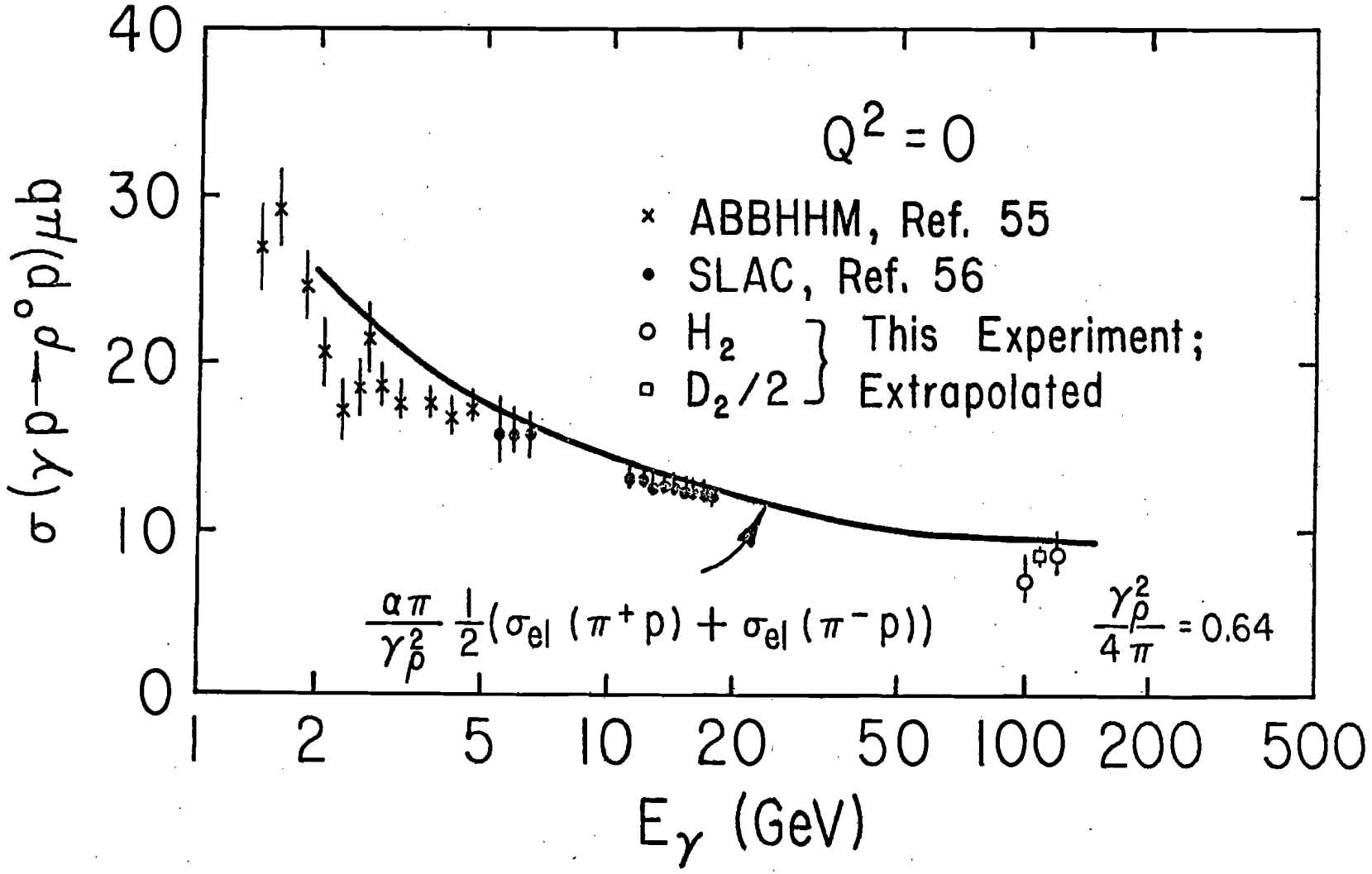

Figure 32.--Energy variation of $\sigma(\gamma p \to \rho p)$. Our and lower energy data are consistent with the prediction, resulting from the combination of Vector Dominance and quark structure of hadrons ideas, shown by the curve. (See equation [I.4] in page 9.) The slow energy variation is indicative of the diffractive nature of the process.

Figure 33.--t differential cross sections and fit for $0.0 < Q^2 < 0.1$ GeV^2/c^2. The data points have been corrected for resolution. The functional form of the fit is given by equation (V.12) in page 98, with coefficients given in Table 17.

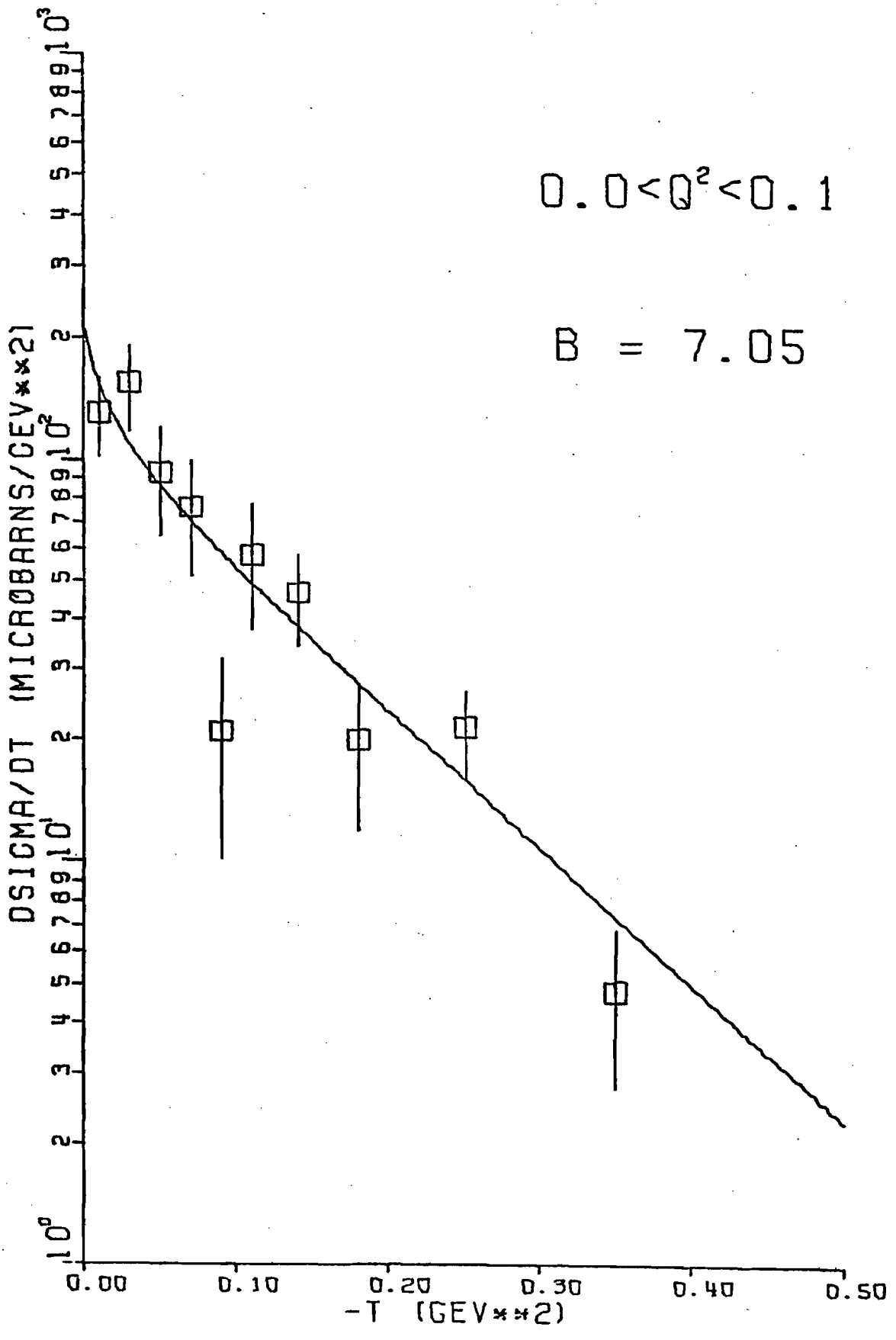
0.0<Q²<0.1
B = 7.05
DSIGMA/DT (MICROBARNS/GEV**2)
-T (GEV**2)
0.00
0.10
0.20
0.30
0.40
0.50

Figure 34.--t differential cross sections and fit for $0.1 < Q^2 < 0.3$ GeV^2/c^2. The data points have been corrected for resolution. The functional form of the fit is given by equation (V.12) in page 98, with coefficients given in Table 17.

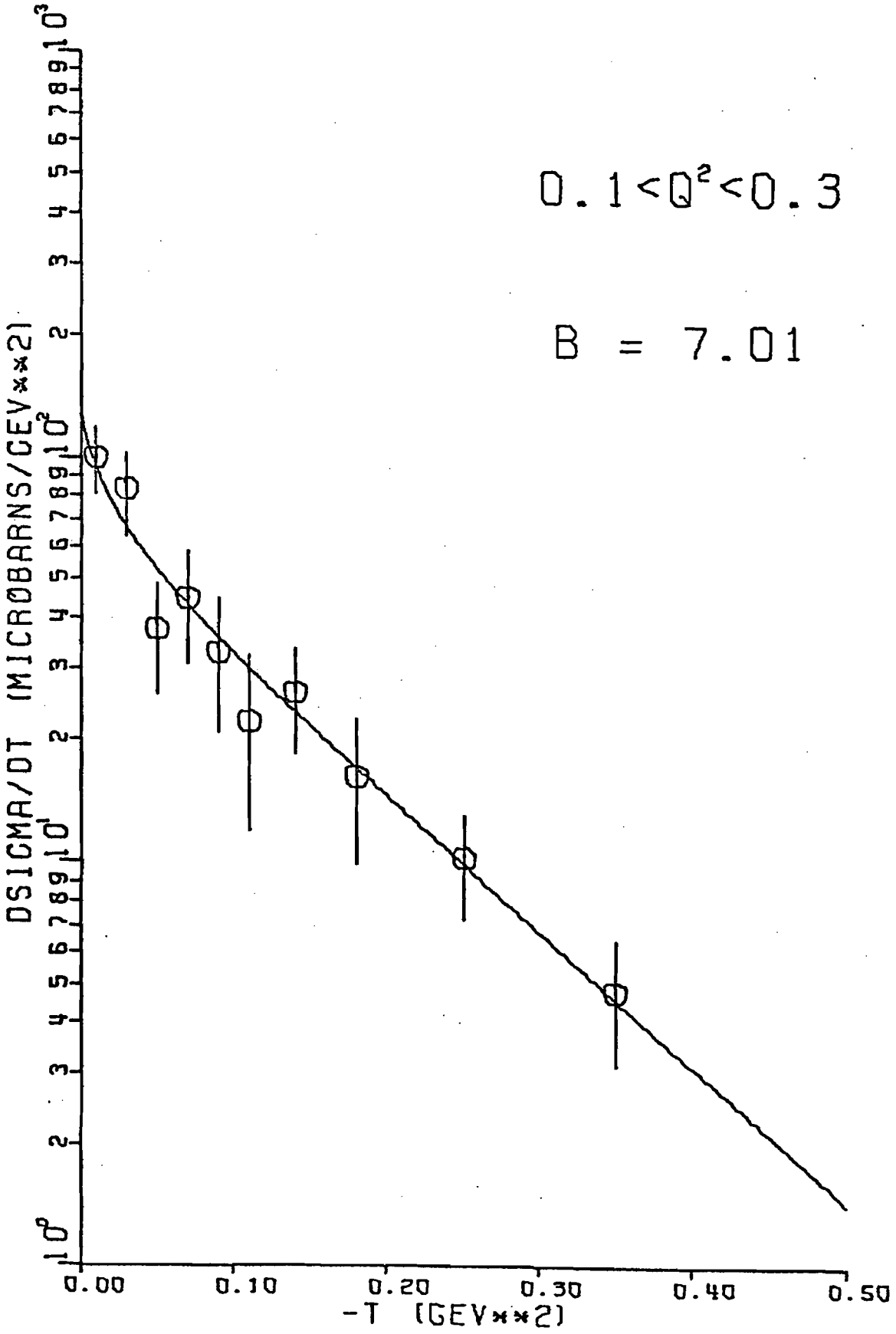
0.1<Q²<0.3
B = 7.01
DSIGMA/DT (MICRØBARNS/GEV**2)
-T (GEV**2)
0.00
0.10
0.20
0.30
0.40
0.50

Figure 35.--t differential cross sections and fit for $0.3 < Q^2 < 1.0$ GeV^2/c^2. The data points have been corrected for resolution. The functional form of the fit is given by equation (V.12) in page 98, with coefficients given in Table 17.

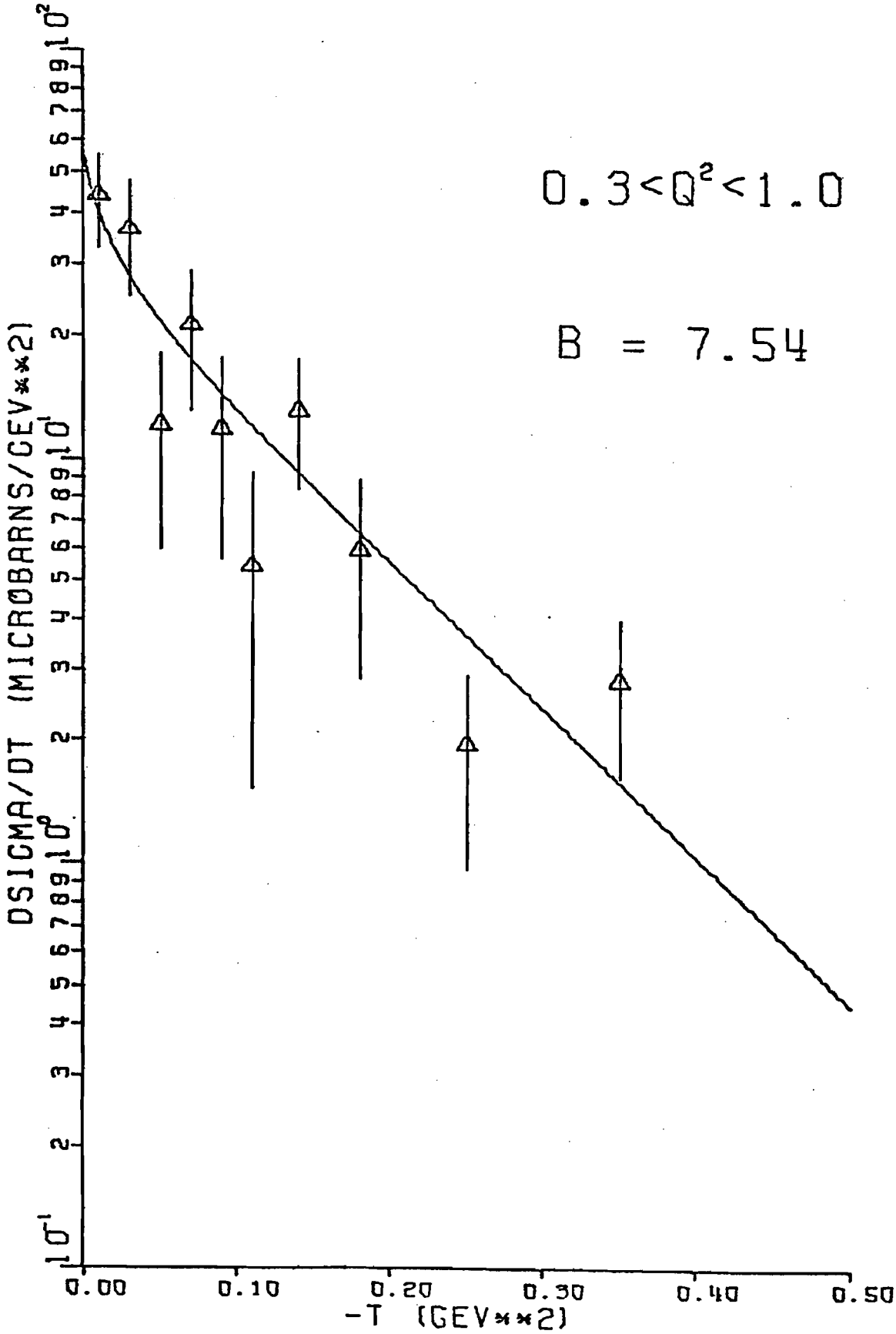
0.3<Q²<1.0
B = 7.54
DSIGMA/DT (MICROBARNS/GEV**2)
-T (GEV**2)
0.00
0.10
0.20
0.30
0.40
0.50

Figure 36.--t differential cross sections and fit for $1.0 < Q^2 < 5.0$ GeV^2/c^2. The data points have been corrected for resolution. The functional form of the fit is given by equation (V.12) in page 98, with coefficients given in Table 17.

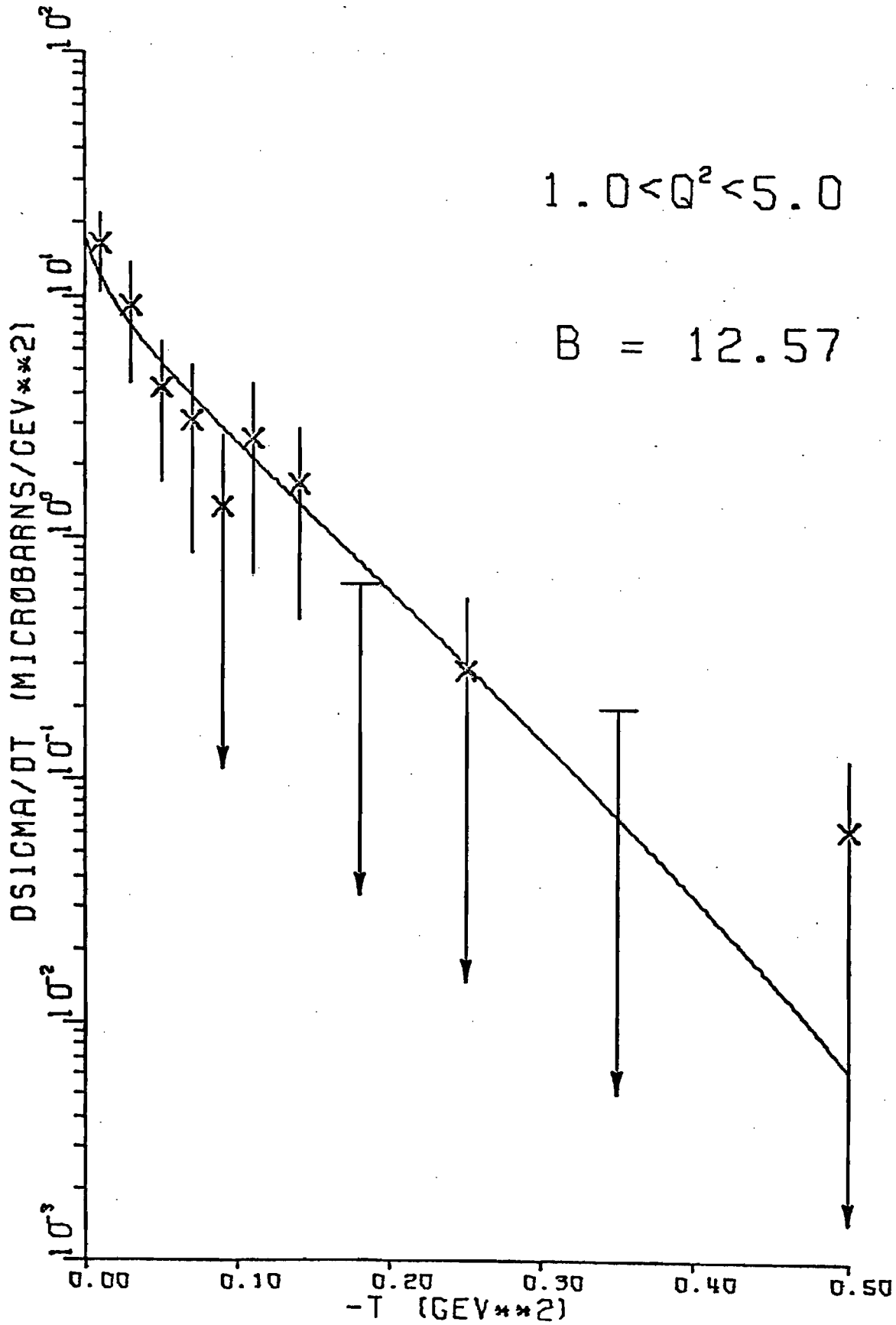
1.0<Q²<5.0
B = 12.57
DSIGMA/DT (MICROBARNS/GEV**2)
10²
10¹
10⁰
10⁻¹
10⁻²
10⁻³
0.00
0.10
0.20
0.30
0.40
0.50
-T (GEV**2)

Figure 37.--Contours of equal probability for the $0.3 < Q^2 < 1.0$ fit to the t differential cross sections. The inner ellipse determines the $\pm 1\ \sigma$ errors.

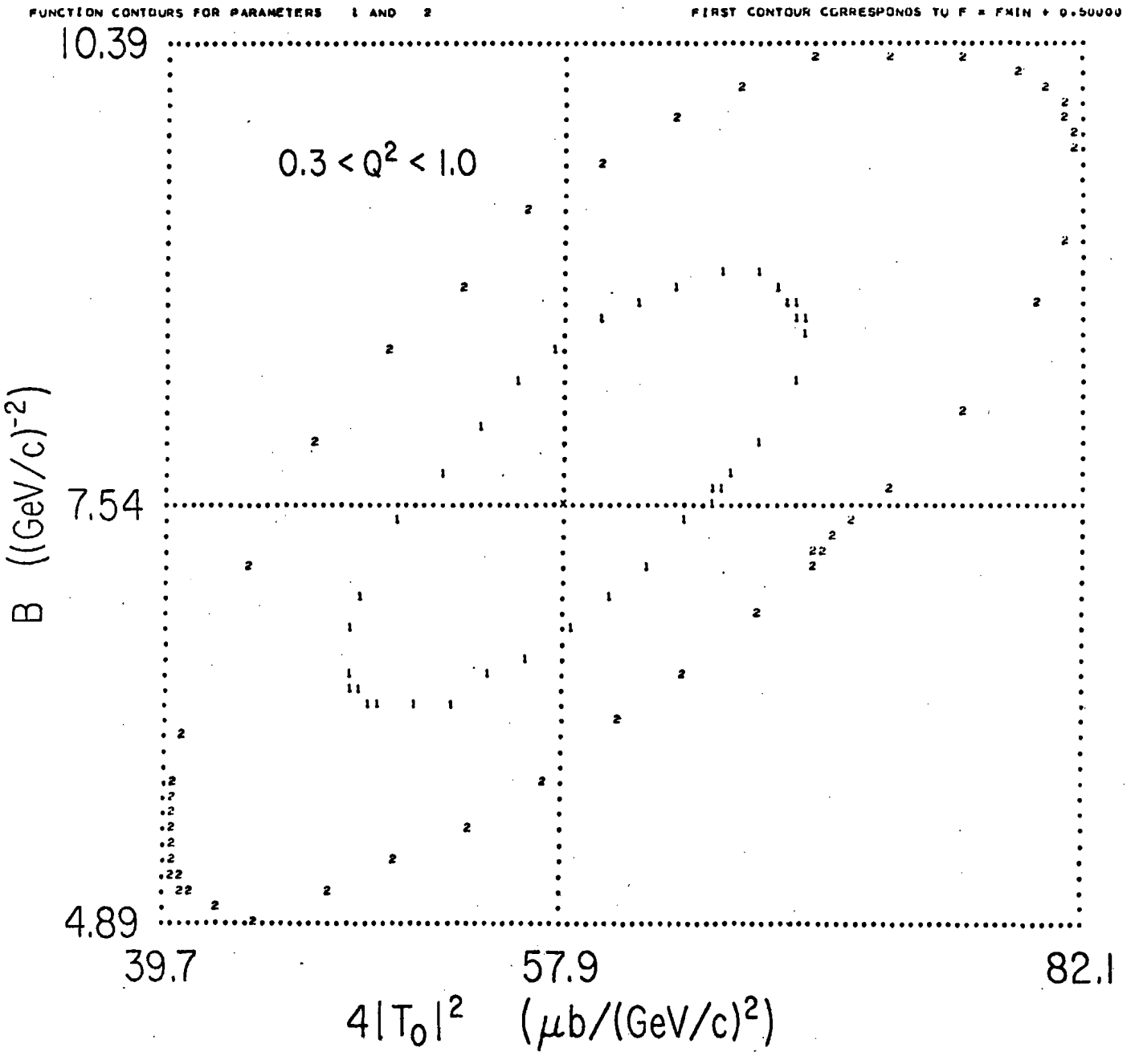
FUNCTION CONTOURS FOR PARAMETERS 1 AND 2
FIRST CONTOUR CORRESPONDS TO F = FMIN + 0.50000
0.3 < Q² < 1.0
10.39
7.54
4.89
B ((GeV/c)⁻²)
39.7
57.9
82.1
4|T₀|² (μb/(GeV/c)²)

Figure 38.--Q^2 variation of B, the $\frac{d\sigma}{dt}$ slope. The comparison of our H_2 and D_2 results shows that they are consistent with $B = 7\ GeV^{-2}$, independent of Q^2. This is evidence against the concept of photon shrinkage with increasing Q^2 (see the discussion in pages 10-13). Moreover, this evidence comes from a kinematic region for which $\Delta\tau > 30\ GeV^{-1}$, i.e., far from any threshold effects. (See page 14 and compare with Figure 4.)

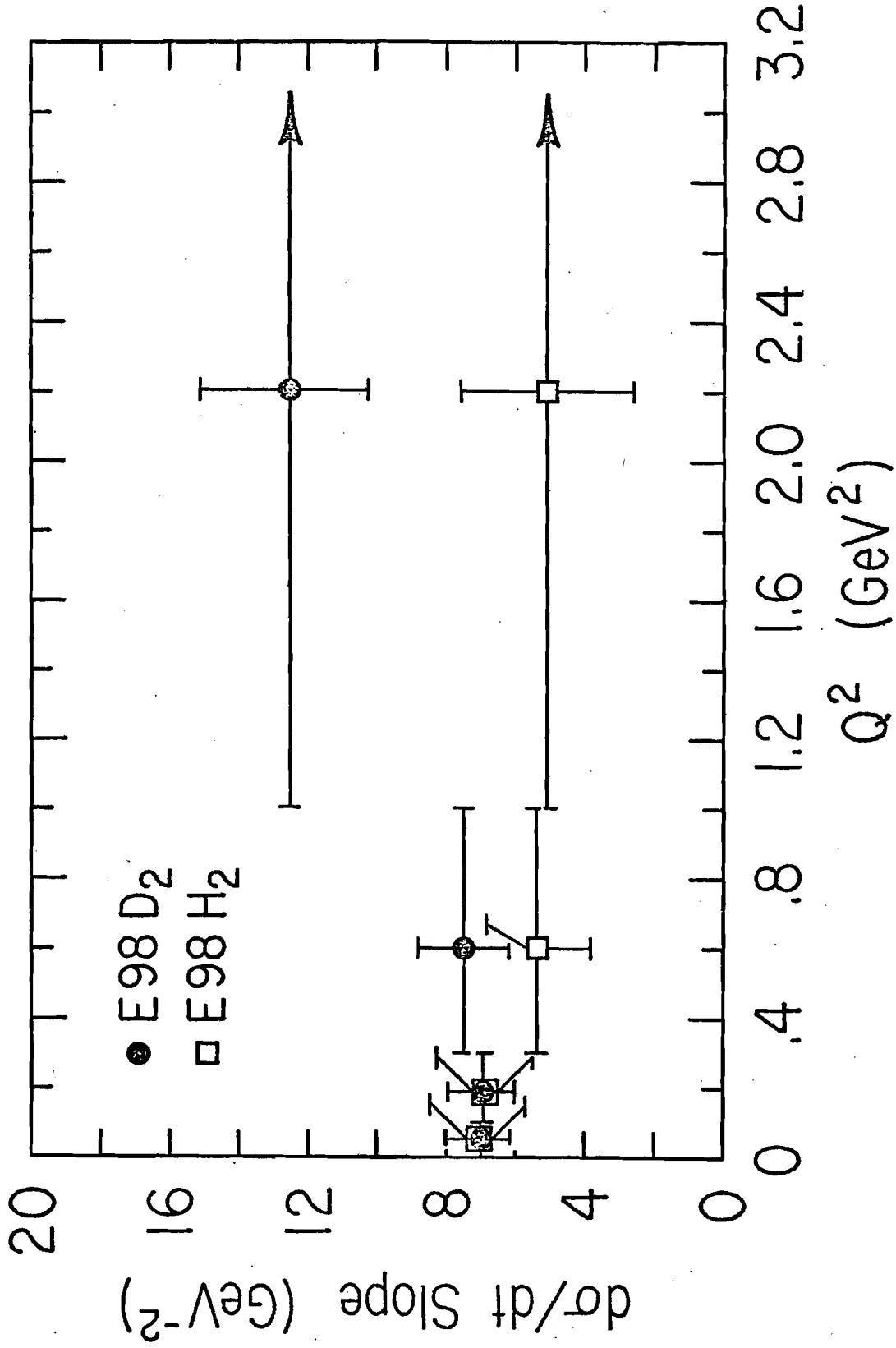
E98 D2
E98 H2
dσ/dt Slope (GeV-2)
Q2 (GeV2)
0
4
8
12
16
20
.4
.8
1.2
1.6
2.0
2.4
2.8
3.2